Anisotropic Mechanical Behaviour
of a Zr-Sn-Nb-Mo Alloy

by

Armando Salinas Rodríguez

A thesis submitted to the Faculty of Graduate Studies
and Research in partial fulfilment of the
requirements for the Degree of Master of Engineering.

Department of Mining and Metallurgical Engineering
McGill University
Montreal, Canada

To Lilia, Celia and Rodolfo

ABSTRACT

The anisotropy of the plastic deformation of EXCEL alloy (Zr-3.8 wt% Sn - 0.8 wt% Mo - 0.8 wt% Nb) was investigated by means of constant true strain rate compression tests. Specimens were machined from a cold drawn and annealed CANDU pressure tube which had a strong (0002) crystallographic texture in the radial-tangential plane. The specimens were oriented along the three principal directions of anisotropy of the tube, namely, axial, tangential and radial, and the flow stress was determined as a function of specimen orientation, true strain and strain rate over the temperature range 295-1200 K.

The flow behaviour of the specimens with axes parallel to the radial and tangential directions was found to be similar. The work hardening rate was highest in the tangential specimens and decreased with strain until fracture occurred by localized shear at temperatures below 900 K or until flow softening took place at the higher temperatures. The axial specimens displayed a completely different behaviour. After an initially decreasing work hardening rate, a regime of low work hardening rate was observed up to strains of about 0.08. After that, the work hardening

rate increased to values similar to those of the tangential specimens and remained constant until fracture occurred. A strong strength differential effect was found in the axial specimens tested in tension and compression at 298 K and $10^{-4}s^{-1}$.

As the temperature was increased above 1000 K, the anisotropic mechanical behaviour of the material decreased considerably and at 1200 K, the flow curves exhibited sharp yield drops and optical microscopy showed the presence of precipitates. The general trend observed was for the flow stress to increase with an increase in the fraction of basal poles parallel to the stress axis and with an increase in strain rate. The effect of temperature was represented in the form of $\sigma(T)$ curves as a function of specimen orientation, true strain rate and true strain. The behaviour for any particular set of conditions tested consisted of an initially slow decrease of the flow stress with increase in temperature ($T \leq 700$ K) and then, for higher temperatures, the flow stress decreased rapidly with increase in temperature.

The general deformation behaviour of the alloy is discussed in terms of the possible deformation mechanisms operating under the various experimental conditions and also with respect to the evolution of the texture caused by the operation of deformation modes such as twinning.

RESUME

L'anisotropie de la déformation plastique de l'alliage EXCEL (Zr-3.8% Sn - 0.8% Mo - 0.8% Nb en poids) a été étudiée au moyen de tests de compression à vitesse de déformation vraie constante. Les échantillons ont été préparés à partir d'un tube de force CANDU étiré à froid et recuit, qui présentait une texture cristallographique (0002) très forte dans le plan radial-tangentiel. Les échantillons étaient orientés suivant les trois directions principales d'anisotropie du tube, c'est-à-dire les directions axiale, tangentielle et radiale et la contrainte d'écoulement a été déterminée en fonction de l'orientation de l'échantillon, de la déformation vraie et de la vitesse de déformation pour des températures variant entre 295 et 1200 K.

L'évolution de la déformation plastique des échantillons d'axes parallèles aux directions radiale et tangentielle s'est avérée être similaire. Le taux d'écrouissage est le plus élevé pour les éprouvettes tangentielles et décroît avec la déformation jusqu'à rupture par cisaillement localisé aux températures inférieures à 900 K ou apparition d'un adoucissement aux températures plus élevées. Les éprouvettes axiales ont un comportement

totalement différent. Il y'a d'abord diminution du taux d'écrouissage, puis l'on observe un régime de faible taux d'écrouissage jusqu'à une déformation d'environ 0.08. Ensuite le taux d'écrouissage augmente jusqu'à des valeurs comparables à celles des échantillons tangentiels et reste constant jusqu'à la rupture. Une différence très importante de contrainte d'écoulement a été observée pour les échantillons axiaux sollicités en traction et compression à 295 K et $10^{-4}s^{-1}$.

Lorsque la température augmente au desous de 1000 K, le comportement mécanique du matériau devient de moins en moins anisotrope; à 1200 K, les courbes d'écoulement présentent un crochet de traction très aigu et des observations au microscope optique révèlent l'apparition de précipités.

La tendance généralement observée est donc la suivante: la contrainte d'écoulement augmente avec la fraction de pôles (0002) parallèles à l'axe de contrainte et avec la vitesse de déformation. L'influence de la température a été représentée par des courbes σ(T) en fonction de l'orientation de l'échantillon, de la déformation vraie et de la vitesse de déformation. Dans tous les cas, le comportement observé lorsque la température augmente consiste en une diminution lente de la contrainte d'écoulement

(pour T ≤ 700 K) suivie d'une décroissance très rapide aux températures plus élevées.

Le comportement de l'alliage est discuté de façon générale à partir des mécanismes de déformation intervenant dans différentes conditions expérimentales et ainsi qu'en fonction de l'évolution de la texture provoquée par les différents modes de déformation tels que le maclage.

RESUMEN

Este trabajo fué enfocado al estudio de la anisotropia de las propiedades mécanicas de la aleación EXCEL (Zr-3.8% Sn-0.8% Mo-0.8% Nb). La investigación fué realizada par medio de pruebas de compresión a velocidad de deformación verdadera constante. Los especímenes de prueba fueron maquinados a partir de un tubo de presión CANDU, el cual habia sido estirado en frio y recocido a 1013 K. La textura cristalográfica del tubo consistió basicamente de polos (0002) orientados en el plano radial-tangencial, exhibiendo un máximo en la dirección paralela a la dirección tangencial. Los especímenes fueron orientados en el tubo de tal forma de que sus ejes fueran paralelos a las tres direcciones principales de anisotropia, esto es, las direcciones tangencial, radial y axial; de esta forma, el esfuerzo de fluencia fué determinado en función de la orientación de los specímenes, la deformación logarítmica y la velocidad de deformación en el rango de temperaturas 295-1200 K.

El comportamiento bajo deformación de los especímenes con ejes paralelos a las direcciones radial y tangencial fué semejante. Los especímenes tangenciales exhibieron la mayor velocidad de endurecimiento por deformación al

inicio de los experimentos. Esta velocidad disminuyó con aumento en la deformación hasta que inestabilidad debido a la formación y ablandamiento de bandas de corte localizado produjo la fractura de los especímenes ensayados a temperaturas menores de 900 K; a tempuraturas más altas la occurrencia de procesos de recuperación dinámica y/o procesos debidos a la evolución de la textura produjo ablandamiento del material a medida que la deformación plástica era aumentada. Los especímenes axiales se comportaron de manera diferente. Al inicio de la deformación la velocidad de endurecimiento disminuyó a medida que la deformación era aumentada hasta que aproximadamente al 2% de deformacion se establecio un régimen de flujo a una velocidad de endurecimiento mínima y aproximadamente constante que se extendió hasta deformaciones verdaderas del orden de 8-10%. Despues de esto, la velocidad de endurecimiento aumentó á valores similares a los observados en especímenes tangenciales para después mantenerse constante hasta que los especímenes fallaban en la misma forma que los tangenciales. Otro fenómeno interesante encontrado en la deformación de muestras axiales fue el hecho que mostraron diferente comportamiento, similar a los especímenes tangenciales, cuando fueron ensayadas en tensión a 298 K y $\dot{\varepsilon} = 10^{-4} s^{-1}$, dando lugar a un fenómeno denominado Diferencial de Resistencia.

A medida que la temperatura era aumentada por arriba de 1000 K, el comportamiento anisotropico del material disminuyó considerablemente y a 1200 K las curvas de deformación exhibieron picos de esfuerzo de flujo y microscopía óptica mostró la presencia de precipitados.

La tendencia general observada fué que el esfuerzo de flujo disminuia con el aumento en la fracción de polos de planos basales orientados paralelos al eje de la deformación y con el aumento en la velocidad de deformación. El effecto de la temperatura fue representado en la forma de curvas $\sigma(T)$ como una función de la orientación de los especímenes, la velocidad de deformación y la deformación plástica verdadera. El comportamiento para un conjunto dado de condiciones experimentales consistió inicialmente, $T \leq 700$ K, de una disminución lenta del esfuerzo de flujo con el aumento en temperatura, mientras que a temperaturas mas altas el esfuerzo requerido para causar deformación plástica en el material disminuyó rápidamente.

El comportamiento mecánico de la aleación fué interpretado y discutido en función de los mecanismos de deformacion que pueden operar bajo las diferentes condiciones experimentales estudiadas asi como con respecto a la posible evolución de la textura debida a la operación de modos de deformación tales como maclado.

ACKNOWLEDGEMENTS

I wish to express my thanks and recognition to Professors John J. Jonas and Melek G. Akben for their guidance, constant encouragement and understanding during the course of this research. With their great deal of knowledge and patience, they always put me on the right track when everything seemed endless and obscure. Professor Akben bore the brunt of my frustration during the initial stages of my research and for that I owe her more than gratitude. I am also indebted to Drs. Carlos Tomé (Universidad Nacional de Rosario, Argentina), Nicholas Christodoulou and Edward F. Ibrahim (Atomic Energy of Canada, Ltd.) for their useful comments, help and interest.

The patience, help and understanding of my fellow graduate students along with helpful comments and suggestions are duly appreciated. I also wish to express my thanks to Ms. Alison Burch for the typing of the manuscript of this work.

Special thanks are due to Atomic Energy of Canada Ltd. for providing the experimental materials and for financial support during the realization of this work.

And finally, I wish to express my gratitude to my wife Lilia for her unlimited moral support, without which this project would not have been realized.

TABLE OF CONTENTS

CHAPTER 5

CHAPTER 6

LIST OF FIGURES

LIST OF TABLES

LIST OF APPENDICES

CHAPTER 1

INTRODUCTION

The CANada Deuterium Uranium Pressurized Heavy Water (CANDU-PHW) reactors use natural uranium as fuel and heavy water as both coolant and moderator. The pressure vessels for the heavy water coolant are pressure tubes fabricated from zirconium alloys. At the present time, the standard pressure tube alloys are Zircaloy-2 and Zr-2.5 wt% Nb. These two alloys have performed very satisfactorily during operation and the limiting factors in their service lives are predicted to be axial elongation, diametral expansion, and sag due to irradiation-enhanced creep and irradiation-induced growth.

The present study deals with the anisotropy of mechanical properties of a new zirconium alloy for pressure tubes developed at the Chalk River Nuclear Laboratories (CRNL) of Atomic Energy of Canada Ltd. This alloy, named EXCEL and containing nominally 3.5 wt% Sn, 0.8 wt% Mo, and 0.8 wt% Nb, was the result of an extensive research program aimed at developing zirconium alloys with at least the same strength and neutron economy as Zr-Nb alloys but having better in-reactor dimensional stability.

The anisotropy of mechanical properties of zirconium and its alloys has been studied extensively during the past 20 years and has been explained in terms of the different deformation mechanisms which operate depending on the stress state, strain rate, and temperature of deformation. It is also now well recognized that this anisotropy is the result of the strong crystallographic textures developed in the finished products as a result of the fabrication process. One of the main concerns related to the deformation behaviour of zirconium alloys is the relationship between the crystallographic texture and the resulting anisotropy of mechanical properties. For example, it is well known that the burst strength (biaxial loading) of Zircaloy fuel cladding is always larger than the tensile strength (uniaxial loading). Thus adequate control of the texture, e.g. with the c poles oriented in the radial-tangential plane, will enhance the strengthening effect of biaxial loading and can therefore allow the use of thinner wall thicknesses and hence the achievement of better neutron economy. Another important example is the incorporation of the so-called Strength Differential effect in the analysis of the fuel clad behaviour. It has been shown that the incorporation of this parameter increases considerably the collapse times calculated on the basis of isotropic behaviour. Up to the present, the most complete investigation regarding the effects of texture on the mechanical behaviour of zirconium alloys at room temperature as well as at Light Water Reactor operating temperatures (573-673 K) has been carried out by Ballinger.* He found that the mechanical behaviour of Zircaloy-2 is a strong function of stress state, temperature, and the basal pole distribution with respect to the stress axis.

The aim of the present work was to produce quantitative information related to the anisotropic behaviour of Excel alloy pressure tube specimens. These were prepared with axes along three different orientations in the tube, namely the axial, tangential, and radial directions; the samples were deformed by means of constant true strain rate compression testing. The test program involved the evaluation of flow data in the temperature range 295-1200 K at 10^{-4} and $10^{-1}s^{-1}$; and for the special case of axial specimens the effect of the stress state (tension vs. compression) on the deformation behaviour was also investigated at room temperature. This test program was also designed to provide data for assessing the probable deformation of Excel pressure tubes over the temperature range for Loss of Coolant Accident (LOCA) simulations in CANDU-PHW reactors.

---

* The complete reference is given in the literature review.

The final objectives of the present work were (i) to provide an up-to-date literature review of the deformation mechanisms that operate during the straining of zirconium and its alloys, and (ii) to consider some of the metallurgical factors involved in the fabrication and design of pressure tubes, particularly those associated with the development potential of zirconium alloys.

CHAPTER 2

DEFORMATION MECHANISMS IN Zr AND Zr-ALLOYS

Zirconium is a metal which crystallizes in the hexagonal close packed (HCP) structure at temperatures below 1138 K with a c/a ratio of 1.593.(1) Although at temperatures above 1138 K zirconium suffers an allotropic transformation from the HCP structure to a body centred cubic (BCC) structure, the deformation characteristics reviewed in this chapter correspond to those of HCP zirconium as this structure has greater technological relevance. Some of the physical properties of zirconium can be seen in perspective if the metal is considered within the context of the eighteen elemental HCP metals (see Table I(1)). The theoretical strength of a solid is directly proportional to its cohesive energy, ΔH_o^o . From Table I, it can be seen that the transition metals (Ti, Co, Zr, Tc, Ru, Hf, Re, and Os) have cohesive energies greater than 418 KJ/g-at. and consequently all of them have high melting points and are strong metals. On the other hand, it should be noted that as the number of d electrons increases in the transition metal series, the lattice parameter, a, decreases, and the density, ρ, cohesive energy and elastic bulk modulus all increase. Thus, it is apparent that zirconium with the smallest number of d

Table I. Physical properties of hcp metals (Ref. 1)

c/a = axial ratio, a = lattice parameter, ρ = density, T_m = melting temperature, T_t = transformation temperature, ΔH°_o = Cohesive Energy, γ = Surface Energy.

Metal*	c/a	a, nm	ρ, g/cc	$T_m(T_t)$,°C	ΔH°_o, kJ/g-at.	$\gamma(T_m)$,J/m^2
Be(4)	1.568	0.229	1.85	1290(1250)	322	1.30
Mg(12)	1.624	0.321	1.74	651	148	0.69
Zn(30)	1.856	0.266	7.13	420	130	0.90
Cd(48)	1.886	0.298	8.65	321	112	0.70
Sc(21)	1.592	0.331	2.99	1539	332	> 1.50
Ti(22)	1.588	0.295	4.54	1668(882)	465	1.75
Co(27)	1.623	0.251	8.90	1493(388)	422	2.22
Y(39)	1.572	0.365	4.47	1509(1487)	404	> 0.80
Zr(40)	1.593	0.323	6.45	1852(865)	604	1.69
Tc(43)	1.605	0.274	11.49	2140	631	2.15

...cont'd

Table I -- cont'd

Metal	c/a	a, nm	ρ, g/cc	$T_m(T_t)$, °C	ΔH°_o, kJ/g-at.	$\gamma(T_m)$, J/m^2
Ru(44)	1.583	0.271	12.40	2250	639	2.66
La(57)	1.615	0.376	6.17	920(864)	423	> 0.75
Hf(72)	1.581	0.319	13.29	2230(1995)	604	1.92
Re(75)	1.615	0.276	21.02	3180	772	3.13
Os(76)	1.579	0.273	22.50	3000	777	2.95
Gd(64)	1.591	0.363	7.90	1312	373	
Dy(66)	1.574	0.359	8.54	1407	278	
Er(68)	1.570	0.356	9.05	1497	393	

* The number in parentheses is the atomic number of each element.

electrons (2) is both inherently strong and relatively light.

A problem which arises as a result of the high strength is the lack of sufficient ductility, which is of importance if the metal is going to be formed. The problem of the ductile vs. brittle response of crystals requires knowledge of their workability in addition to their fracture strength. Pugh(2) introduced the quotient of elastic bulk modulus to shear modulus, K/G, as an indication of the extent of plasticity inherent in a pure metal (see Table II).(1) According to this view, a high value of K/G is associated with ductility and a low value with brittleness. Although the ductility is also affected by the grain size, temperature, and strain rate, as well as by the presence of inclusions and second phases, it is evident from Table II(1) that "low" values of K/G are associated with poor and fair ductilities (15% elongation or less) and "high" values with good ductilities (40% elongation or more).

Another correlation regarding the ductility was carried out by Rice and Thomson(3) who concluded that crystals whose dislocations have wide cores (i.e. relatively high values of Poisson's ratio, ν) and small values of the parameter Gb/γ ($Gb/\gamma \leq 7.5$ to 10) are ductile while crystals with narrow cored dislocations (i.e. low values of ν) and large values of Gb/γ are brittle. Here G is the shear modulus of the crystal, b is the Burgers vector of the disloca-

Table II. Elastic properties and ductility of hcp metals (Ref. 1). K = elastic modulus, G = shear modulus, b = Burgers vector, γ = Surface Energy. See text for the definition of the parameter Gb/γ.

Metal	c/a	K/G	Ductility	Gb/γ
Cd	1.886	2.21	Fair	10.24
Zn	1.856	1.73	Poor	11.73
Mg	1.624	2.03	Fair	8.10
Co	1.623	2.31	Fair	9.27
Re	1.615	2.05	Fair	15.73
Tl	1.599	6.52	Good	
Zr	1.593	2.65	Good	6.90
Sc	1.592	1.94		9.27
Ti	1.588	2.47	Good	7.31
Ru	1.583	1.63	Poor	19.45
Hf	1.581	1.95	Good	9.16
Os	1.579		Poor	
Y	1.572	1.63	Fair	11.59
Be	1.568	0.74	Poor	26.12

tions and γ is the true surface energy of the crack plane determined as the energy necessary to break the bonds at the crack tip. Dislocations with large core widths are considered to be more mobile, giving rise to easy plastic flow. As can be seen from Table II, the correlation between low values of Gb/γ and good ductility is not as good as in the case of the parameter K/G, although both correlations show that Zr is one of the more ductile of the HCP metals.

The question of the ductility has to be analysed very carefully since, for a polycrystalline metal to undergo a general homogeneous deformation without cracking, five independent slip systems are necessary.(4-8) Unfortunately, as a result of the nature of the HCP structure, the number of independent slip systems in a metal such as Zr is limited. The two most likely Burgers vectors in the HCP crystal structure are $\langle\vec{a}\rangle$ and $\langle\vec{c} + \vec{a}\rangle$ and the possible slip systems are shown in Fig. 1. The independent modes of slip in HCP crystals were analysed by Grooves and Kelly(7) and are listed in Table III. The two most common types of slip system, basal and prismatic, offer only a total of four independent modes between them. Furthermore, the independent modes contributed by the pyramidal slip system with $\langle\vec{a}\rangle$ Burgers vectors are crystallographically equivalent to the combination of four independent modes contributed by cross-slip between the basal and prismatic slip

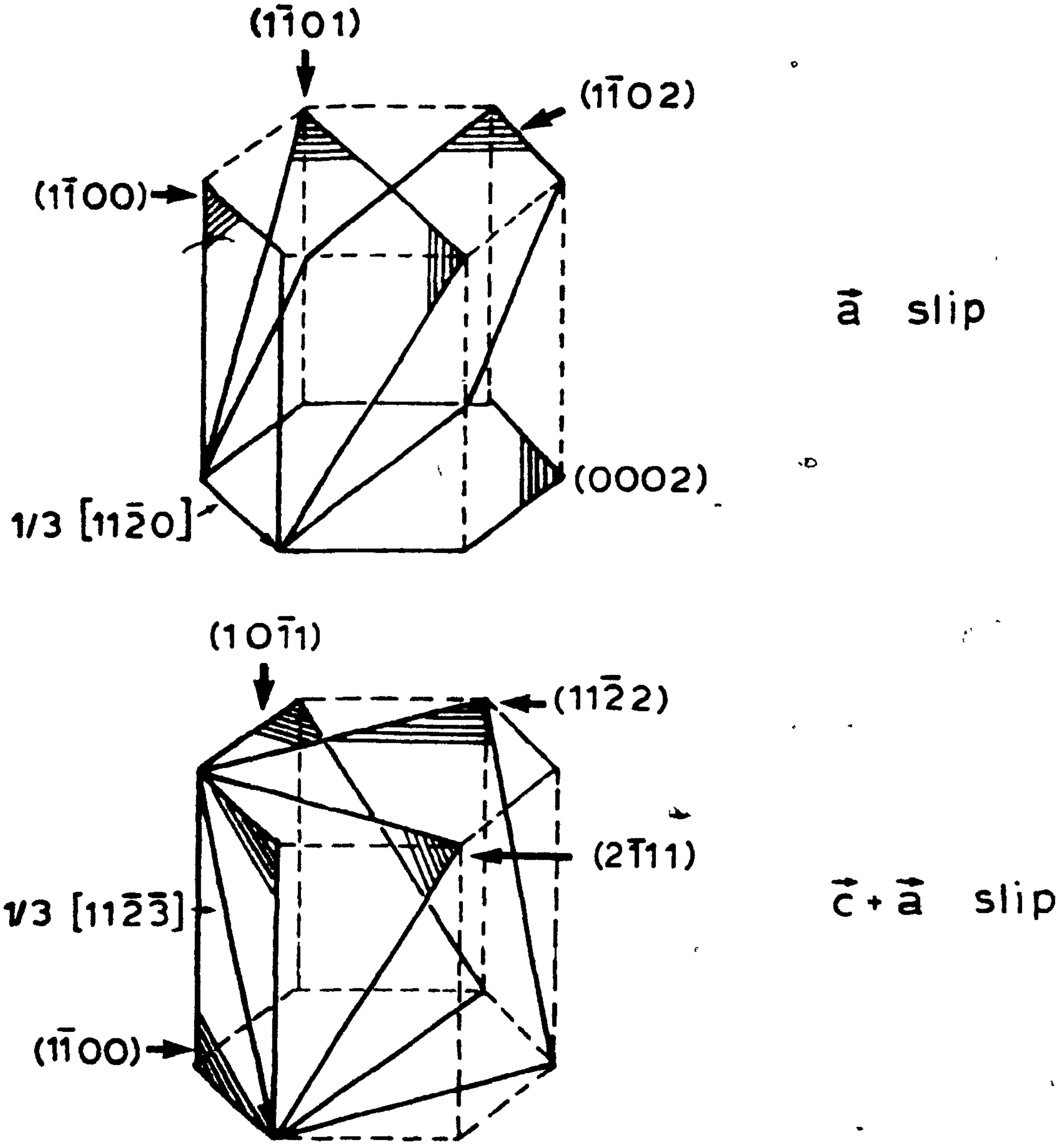

Figure 1. Basal, prismatic and pyramidal slip systems with <$\vec{a}$> Burgers vectors and four possible pyramidal slip planes with <$\vec{c}+\vec{a}$> Burgers vectors.

Table III. Independent modes of deformation in hcp crystals

Direction	Mode	Crystallographic Elements	Number of Independent Modes
a	Basal Slip	$(0002)\langle 11\bar{2}0\rangle$	2
	Prismatic Slip	$\{1\bar{1}00\}\langle 11\bar{2}0\rangle$	2
	Pyramidal Slip	$\{1\bar{1}0\ell\}\langle 11\bar{2}0\rangle$	4
c + a	Pyramidal Slip	$\{hki\ell\}^{*}\langle 11\overline{23}\rangle$	5
	Twinning	$\{K_1\}\langle \bar{\eta}_1\rangle^{\dagger}$	0-5

*See Fig. 1

†See Table IV

systems. Thus, when cross-slip is taking place between basal, prismatic and pyramidal planes and only <$\vec{a}$> Burgers vectors are involved, there are still only four independent modes of deformation . By contrast, when a slip system with a <$\vec{c}$ + $\vec{a}$> Burgers vector is operative, it provides five independent modes, which alone are sufficient to fulfill the von Mises criterion.(4,6)

Kocks and Westlake(9) have shown that ductility in polycrystalline hexagonal materials may not in fact require five independent slip systems, because the internal stresses set up at grain boundaries when the inelastic strains are not compatible can be relieved by localized deformation by twinning. By considering grain interactions without requiring the strain rate to be the same in each grain, Hutchinson(10,11) concluded that the overall inelastic deformation of a polycrystal is possible with only four linearly independent slip systems, i.e. without the necessity of <$\vec{c}$ + $\vec{a}$> pyramidal slip.

As will be discussed later, the <$\vec{c}$ + $\vec{a}$> slip system has not been observed experimentally in pure zirconium deformed at temperatures below 573 K, so that the good ductility of Zr at room temperature cannot be explained in terms of the relative ease of this type of glide. Instead, other deformation mechanisms, such as twinning and kinking, must operate during the plastic straining of Zr in order to permit fracture free deformation. Table IV lists the twins observed

Table IV. Twinning elements in zirconium and zirconium alloys. See Fig. 2 for the definitions of the twinning elements k_1, η_1, k_2, η_2. t_s is given by $t_s = 2 \cot \theta$.

K_1	η_1	K_2	η_2	Experimentally Determined Twinning Shear t_s	Stress State Normal to {0002}	Theoretical Twinning Shear g
$\{10\bar{1}2\}$	$\langle 10\bar{1}\bar{1} \rangle$	$\{10\bar{1}2\}$	$\langle 10\bar{1}1 \rangle$	0.167	TENSILE	$(\gamma^2-3)/\gamma\sqrt{3}$
$\{11\bar{2}1\}$	$\langle 11\bar{2}6 \rangle$	$\{0002\}$	$\langle 11\bar{2}0 \rangle$	0.630	TENSILE	$1/\gamma$
$\{11\bar{2}2\}$	$\langle 11\bar{2}\bar{3} \rangle$	$\{11\bar{2}\bar{4}\}$	$\langle 22\bar{4}3 \rangle$	0.225	COMPRESSIVE	$2(\gamma^2-2)3\gamma$
$\{10\bar{1}1\}$	$\langle \bar{1}012 \rangle$	$\{\bar{1}013\}$	$\langle 30\bar{3}2 \rangle$	0.104	COMPRESSIVE	$(4\gamma^2-9)/4\gamma\sqrt{3}$

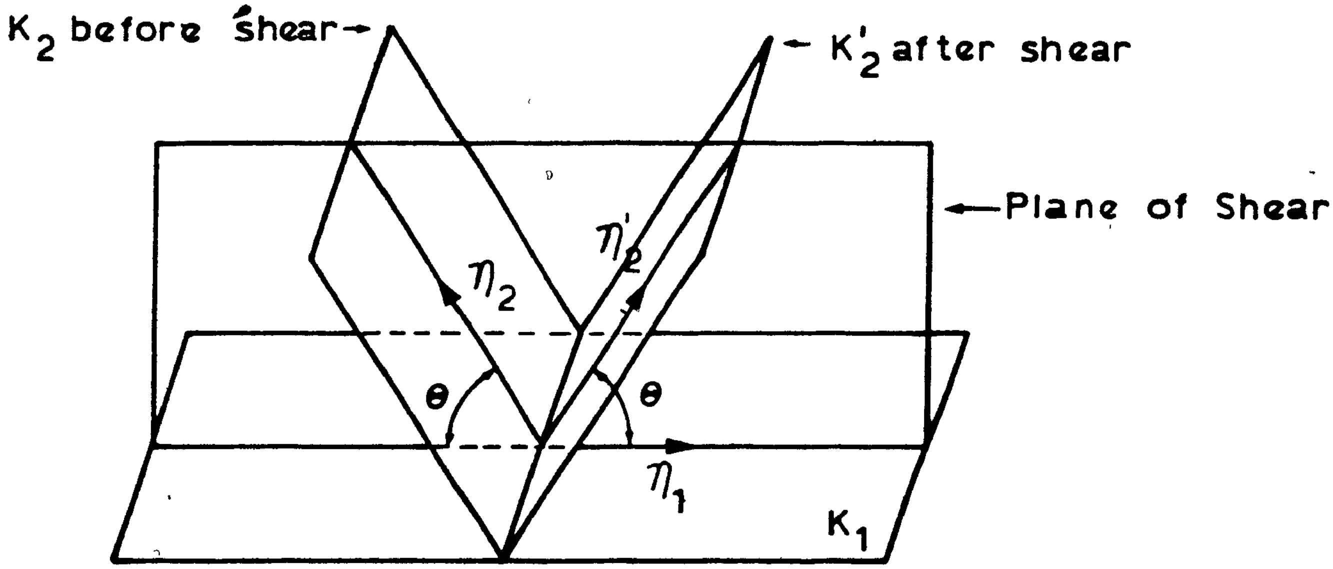

Figure 2. Crystallographic elements of twinning. The unit cell is defined by η_1, the shear direction; η_2, the direction of intersection of the plane of shear (defined by the twinning plane, K_1, and the shear direction) with the second undistorted plane K_2; and the plane of shear, S. It is homogeneously sheared into the unit cell in the twin defined by η_1, η'_2 and S. K'_2 and η'_2 are the second undistorted plane and the direction of intersection of the plane of shear with K_2 after the twinning operation has occurred.

in zirconium and zirconium alloys while Fig. 2 shows the pertinent elements in the twinning operation.

In the sections that follow, the available evidence about the deformation mechanisms operating in Zr and its alloys is reviewed with the objective of providing some understanding of the mechanical behaviour of this important material.

2.1 Single Crystal Deformation

The first detailed determination of the deformation mechanisms operating in Zr was carried out by Rapperport.(12,13) In his study zirconium crystals and large grained samples with a wide distribution of crystal orientations were tested in tension and compression at room temperature. The only slip system observed was the $\{10\bar{1}0\}$ $\langle 11\bar{2}0\rangle$, with an average critical resolved shear stress (CRSS) in compression of 6.37 MPa. No basal slip was observed in any of the crystals tested, even for crystals in which the resolved shear stress on the (0002) basal plane, in a $\langle 11\bar{2}0\rangle$ direction, was up to nine times greater than the resolved shear stress on the prism slip systems.

Twinning was found to occur on four different planes, $\{10\bar{1}2\}$, $\{11\bar{2}1\}$, $\{11\bar{2}2\}$, and $\{11\bar{2}3\}$. The most frequently observed twinning plane was the $\{11\bar{2}1\}$ and then the $\{10\bar{1}2\}$; the $\{11\bar{2}2\}$ and $\{11\bar{2}3\}$ were the least frequent. The theoretical twinning shear g (see Table IV), due to the most commonly observed twin system in a given HCP metal, is plotted as a function of the axial ratio $\gamma = c/a$ in Fig. 3. In this figure a twin mode showing a positive slope causes <u>contraction</u> along the c axis, and one showing a negative slope causes <u>extension</u>; thus, for the case of zirconium, the $\{10\bar{1}2\}$ and $\{11\bar{2}1\}$ twins are "tensile" twins, whereas the $\{11\bar{2}2\}$ twin is a "compression" twin. If Rapperport's data are analysed on this basis, it can be seen that, for crystals whose stress axis is within 50-80 degrees of the basal pole, a considerable amount of $\{10\bar{1}2\}$ twins are observed if the specimen is deformed in tension or $\{11\bar{2}2\}$ twinning if the specimen is loaded in compression. $\{11\bar{2}3\}$ twins were only observed in samples which had been deformed more than 10%.

The effect of temperature on the deformation mechanisms of zirconium was determined by Rapperport and Hartley.(14) Once again, the only slip system determined to operate within the temperature range 77 - 1075 K was of the $\{10\bar{1}0\}\langle 11\bar{2}0\rangle$ type with a CRSS in tension ranging from 9.8 MPa at 77 K to 0.196 MPa at 1075 K. As in the previous work, no basal slip could be detected even for crystals oriented in such a way that the ratio of the maximum shear stress on the basal plane with respect to that on the prism plane was as high as 25. In this work, the stress axis was generally oriented at an angle of from 50 to 80 degrees from

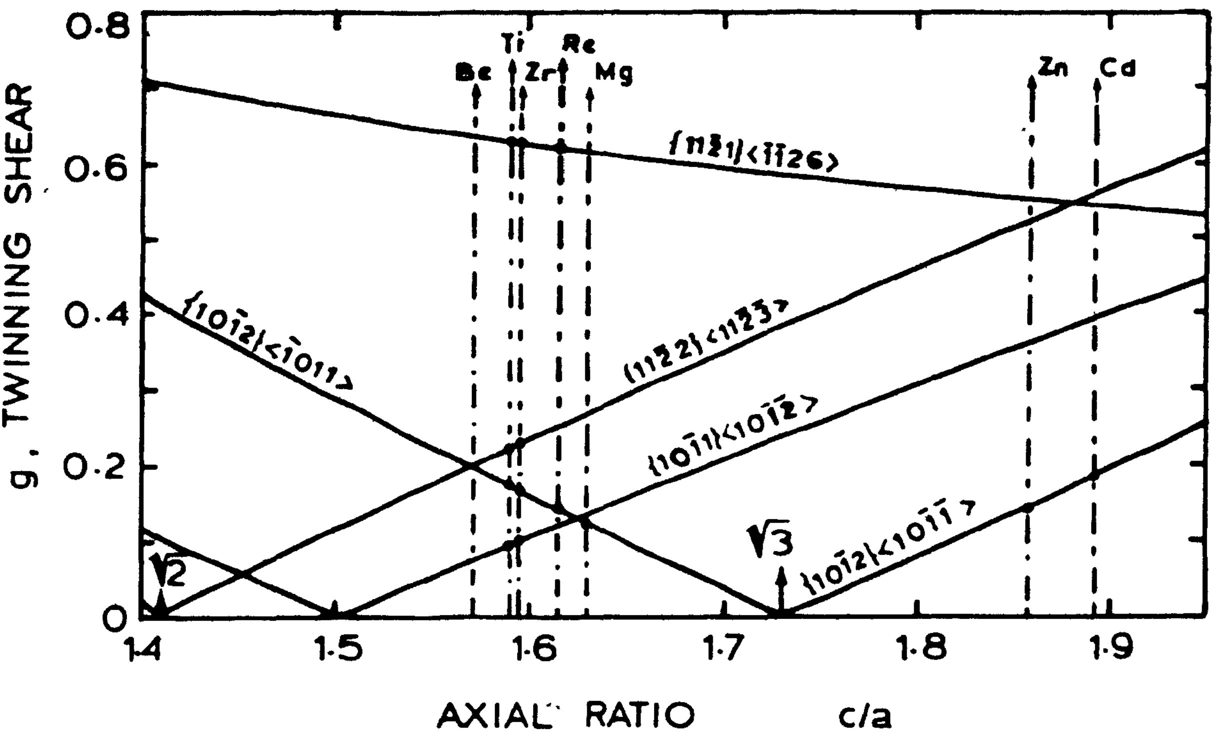

Figure 3. Variation of the twinning shear g with the axial ratio (c/a). A dot indicates that the twin mode is in an active mode for the metal.

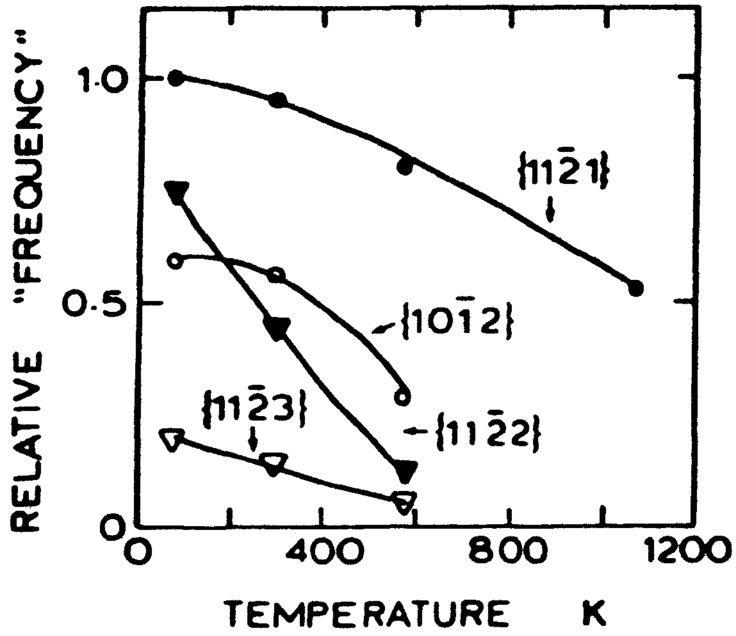

Figure 4. Schematic plot of relative "frequency" or "activity" of twin families vs. deformation temperature for zirconium.

the basal pole and, as can be seen in Fig. 4,(14) the most frequently found twin at all temperatures was of the $\{11\bar{2}1\}$ type with $\{10\bar{1}2\}$, $\{11\bar{2}2\}$, and $\{11\bar{2}3\}$ appearing in decreasing order of importance. $\{11\bar{2}3\}$ twins were seldom found at all temperatures and when found, they were localized at positions where the stress state was complex, i.e. near grain boundaries. $\{10\bar{1}2\}$ and $\{11\bar{2}2\}$ twins were present up to temperatures below 600 K and the relative frequency of occurrence decreased with temperature until, at 1075 K, the only twinning mode was $\{11\bar{2}1\}$.

Westlake(15) has used the dislocation theory of twinning(16,17) in order to propose a mechanism for the twinning process in zirconium. These models suggest that a twinning dislocation could be produced by the interaction of minor dislocations in the case of $\{10\bar{1}2\}$ twinning, or by the interaction of a minor and a major dislocation in the case of $\{11\bar{2}2\}$ twinning. These interactions might occur at dislocation pile-ups formed as a result of prior slip. Rapperport and Hartley(14) found that $\{10\bar{1}2\}$ and $\{11\bar{2}0\}$ twins were only formed after severe deformation by slip had occurred. In the case of $\{11\bar{2}1\}$ twinning, the model becomes quite complicated and it remains uncertain whether a dislocation mechanism can be feasible for this particular twinning mode. Perhaps one of the most important outcomes of the model is that the microscopic applied stress cannot be a measure of the nucleation stress and therefore it

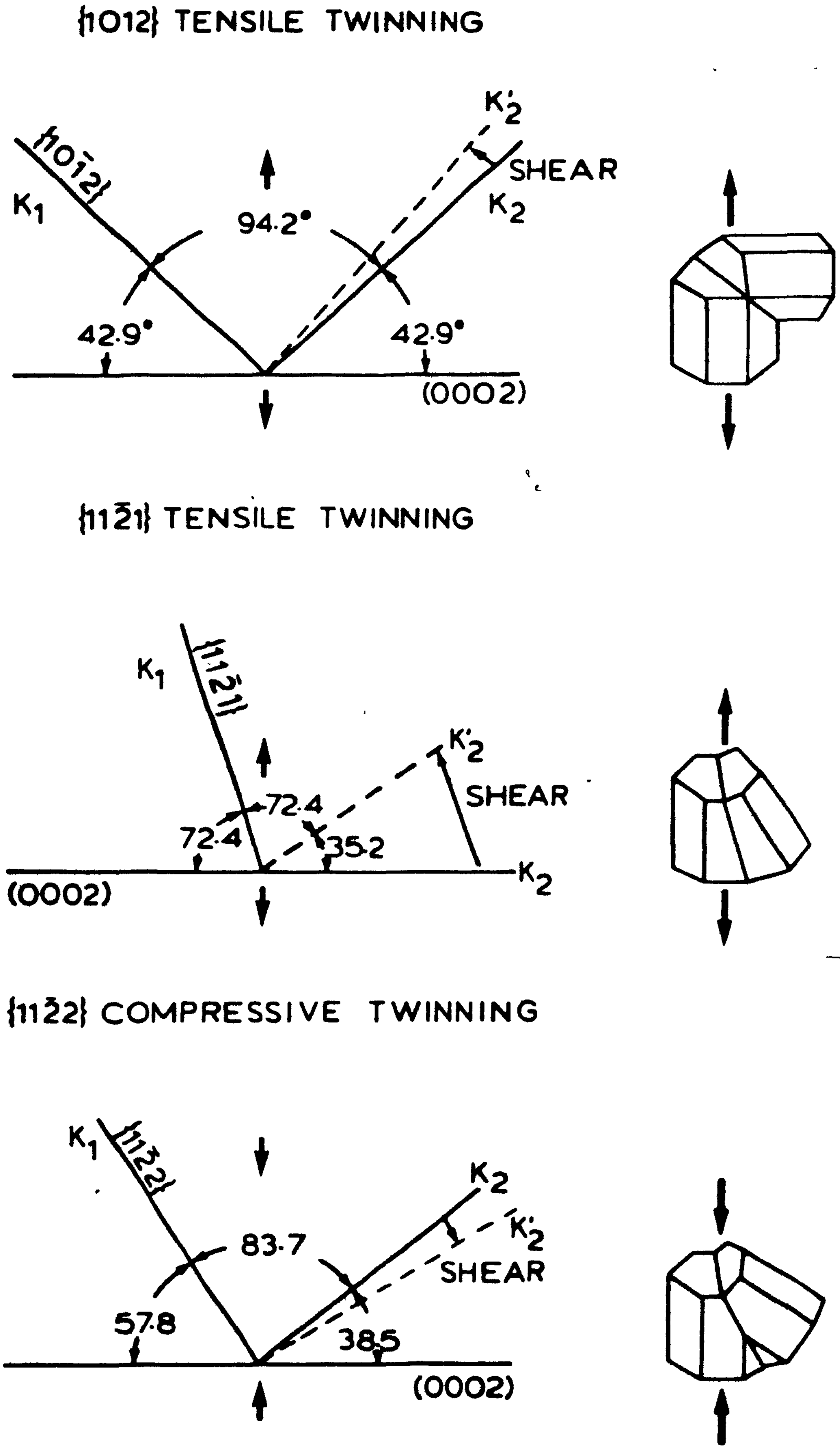
{1012} TENSILE TWINNING

{11$\bar{2}$1} TENSILE TWINNING

{11$\bar{2}$2} COMPRESSIVE TWINNING

Figure 5. Commonly observed twinning systems in zirconium.

does not appear as though there is a critical resolved shear stress for twinning.

Akhtar and Teghtsoonian(18) studied the effect of crystal orientation, temperature and strain rate on the work hardening parameters of Zr single crystals. They found that, at 78 K, when the angle χ_B between the basal plane and the stress axis was less than 35 degrees, the onset of plastic flow occurred by prismatic slip and the CRSS was independent of initial orientation. However, at χ_B greater than 35 degrees, plastic flow first occurred by twinning and load drops were observed. Also, with increasing χ_B (>35 degrees), twinning occurred at smaller fractions of the CRSS for prismatic slip. An interesting result was that for orientations favourable for slip, the stress-strain curve showed three stages of work hardening similar to those found in face centred cubic (FCC) single crystals. These stages were associated with primary prismatic slip and conjugate slip for stages I and II respectively, while dynamic recovery in stage III was suggested to be due to cross-slip from the prism to the basal plane. The presence of wavy slip lines associated with cross-slip from the prism to the basal plane has also been observed by Martin and Reed-Hill(19) and by Westlake.(20) At 295 K, similar orientation effects were observed, and although no explanation was provided for the transition from twinning to slip, it was observed again with a transition angle of 45 degrees.

In this study, although a wide range of orientations was tested, no basal slip could be detected.

Akhtar(21) carried out tensile tests on zirconium single crystals with unfavourable orientations for prismatic slip over the temperature range 295-1113 K. He found that basal slip did occur in crystals with appropriate orientations at temperatures higher than 850 K; at lower temperatures, plastic deformation occurred by prismatic slip and twinning. The CRSS for prismatic and basal slip is given in Fig. 6 as a function of temperature. This figure clearly shows that the CRSS for basal slip decreases continuously from about 5 at 850 K to 1.12 MPa at 1100 K. What these results indicate is that, even though a small amount of basal slip can occur at temperatures above 850 K, prismatic slip continues to be the slip mode operative at the lowest stress level. Akhtar suggests that basal slip occurs by a mechanism in which cross-slip is preceded by the recombination of partial dislocations on prism planes.

So far, no deformation mechanism except for $\{11\bar{2}2\}$ twinning can allow for the application of a negative strain along the c-axis. However, another mechanism that could accomplish this would be pyramidal slip with a $<\vec{c} + \vec{a}>$ type of Burgers vector. As will be discussed later, the textures developed and their stability in rolled zirconium cannot be explained in terms of prismatic slip alone, but rather by a sequence of several complicated twinning opera-

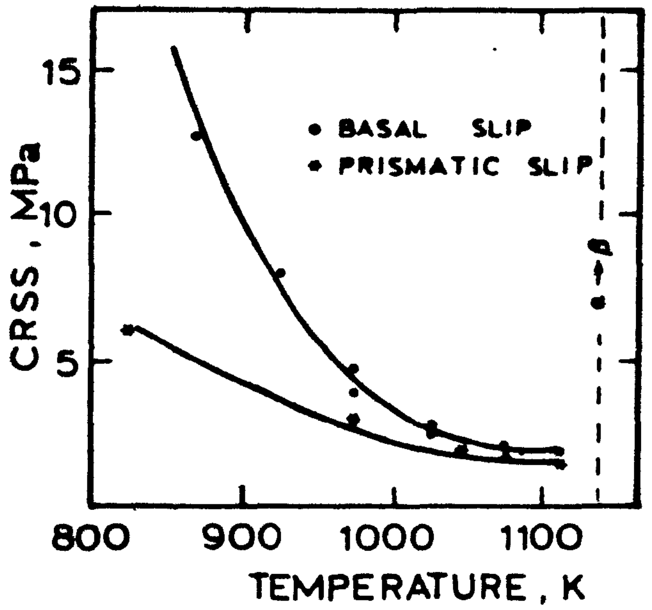

Figure 6. Critical Resolved Shear Stress (CRSS) as a function of temperature for basal and prismatic slip.

tions,(22) or, alternatively, by the activation of a slip system which can allow strain components perpendicular to the basal plane,(23) i.e. $\langle \vec{c} + \vec{a} \rangle$ slip. The operation of $\langle \vec{c} + \vec{a} \rangle$ slip in zirconium single crystals has only been observed under severely constrained deformation conditions or at high temperatures. Tenckhoff(24) deformed Zr crystals at different temperatures under conditions which concentrated shear deformation along $\langle 11\bar{2}3 \rangle$ directions and he found dislocations with 1/3 $\langle 11\bar{2}3 \rangle$ Burgers vectors, the frequency of which increased as the temperature increased. The slip planes for these $\langle \vec{c} + \vec{a} \rangle$ dislocations were suggested to be of the $\{11\bar{2}1\}$ and $\{10\bar{1}1\}$ type, although no conclusive evidence was obtained.

Akhtar(25) deformed single crystals in compression along the c-axis between 78 and 1100 K. He found that plastic deformation occurred by $\{11\bar{2}2\}$ twinning up to a temperature of 800 K, whereas twins of the $\{10\bar{1}1\}$ type, in conjunction with $\langle \vec{c} + \vec{a} \rangle$ slip on $\{10\bar{1}1\}$ planes, were observed to initiate plastic flow at temperatures above 800 K. The CRSS for $\langle \vec{c} + \vec{a} \rangle$ slip was determined to be approximately 10-20 times that required for prismatic slip.

2.2 Deformation of Polycrystalline Zirconium

The stress state required to activate the necessary deformation systems to cause an arbitrary strain in polycrystals varies from grain to grain because of differences in their crystallographic orientations. As a result of this, residual stresses(26) are produced whose wavelengths are of the order of the grain size. The presence of grain boundaries thus imposes constraints which have significant effects on the operative deformation mechanisms. Because of the internal stresses, the local stresses in certain regions of the polycrystal may be several times higher than the applied stress. All this, together with the compatibility principle mentioned earlier, can cause certain slip and twinning systems, which would not normally operate in a single crystal, to operate under a particular set of polycrystalline conditions. Of particular importance are the effects of temperature and strain rate on stress relaxation, which can have a strong effect on the regimes over which the twinning modes operate.(27) In addition, alloying elements may also have a strong effect on the deformation mechanisms.

One of the most extensive investigations dealing with the deformation of zirconium polycrystals was conducted by Reed-Hill;(28) he suggested that the excellent plasticity of polycrystalline zirconium is closely related to the ease of mechanical twinning. He carried out tensile tests on specimens machined from rolled zirconium plate with a deformation texture consisting of basal planes parallel to the rolling direction with a $[10\bar{1}0]$ direction in the rolling direction. The basal plane poles were concentrated in a narrow band centred about the normal direction of the plate with a peak at about 30-40 degrees from this direction. This texture allowed Reed-Hill to select a wide range of basal orientations with respect to the tensile axis. The twinning mechanisms observed to operate in polycrystalline zirconium were essentially those observed in single crystal deformation (Fig. 5). At room temperature and slow strain rates, the $\{10\bar{1}2\}$ twinning mode predominated in polycrystalline specimens so that deformation occurred by $\{10\bar{1}2\}$ twinning and $\{10\bar{1}0\}$ prismatic slip.

The orientation factor, i.e. the ratio of the shear stress, S_s , resolved on the slip plane to the applied normal stress, S_n , is defined as:

$$\text{Orientation Factor} = S_s/S_n = \cos\phi \cos\lambda \qquad (2.1)$$

where ϕ and λ are the angles bewteen the stress axis and the slip plane normal, and stress axis and slip direction respectively (see Fig. 9). Figure 7 (28) gives the orientation factors for prism slip and $\{10\bar{1}2\}$ twinning as a function of the angle between the stress axis and the basal plane pole; as can be seen, when the stress axis approaches the basal pole, the resolved shear stress on the prism slip planes is low, and consequently the corresponding stresses on the six $\{10\bar{1}2\}$ twinning planes become large. As a result, $\{10\bar{1}2\}$ twinning and $\{10\bar{1}0\}$ slip may be regarded

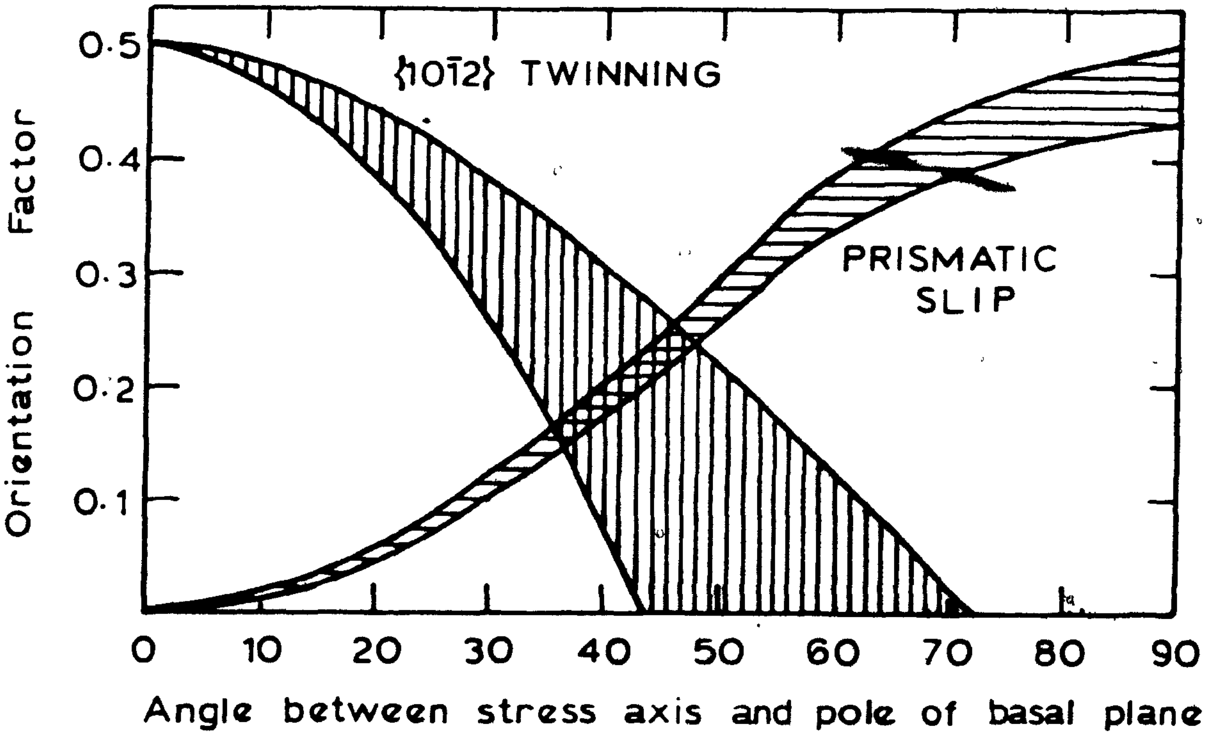

Figure 7. The orientation factors $S_s/S_n = \cos\phi \cos\lambda$ for prismatic slip and {10$\bar{1}$2} twinning as a function of the angle between the basal plane normal and the stress axis.

as complementary deformation mechanisms with the number of twinned and untwinned grains being approximately equal. Figure 8 shows that grains unfavourably oriented for prism slip are likely to support $\{10\bar{1}2\}$ or $\{11\bar{2}1\}$ twinning. $\{11\bar{2}1\}$ twinning should be favoured in an intermediate orientation range where orientation factors for both prism slip and $\{10\bar{1}2\}$ twinning are low. It also seems clear that $\{11\bar{2}2\}$ twinning is competitive with prism slip. An analysis of the various orientation factors as a function of stress axis position in the sterographic triangle shows that $\{11\bar{2}1\}$ twinning is favoured in the orientation range where the stress axis makes an angle between 20 to 60 degrees with the basal pole. At larger angles, the orientation factors for prism slip and $\{11\bar{2}2\}$ twinning alternate in relative importance as one moves across the stereographic triangle in a direction which makes a constant angle with the basal plane pole (such as along the small circle abc in Fig. 9).

Reed-Hill also found that a direct relationship between volume fraction twinned and total strain can be established regardless of the orientation of the specimens (see Fig. 10). This led him to conclude that twinning constitutes an integral part of the deformation of an aggregate of Zr grains of varying orientation and that the flow stress may be controlled by the ability of the metal to twin. At lower temperatures and faster strain rates, more twinning modes become active and the incidence of

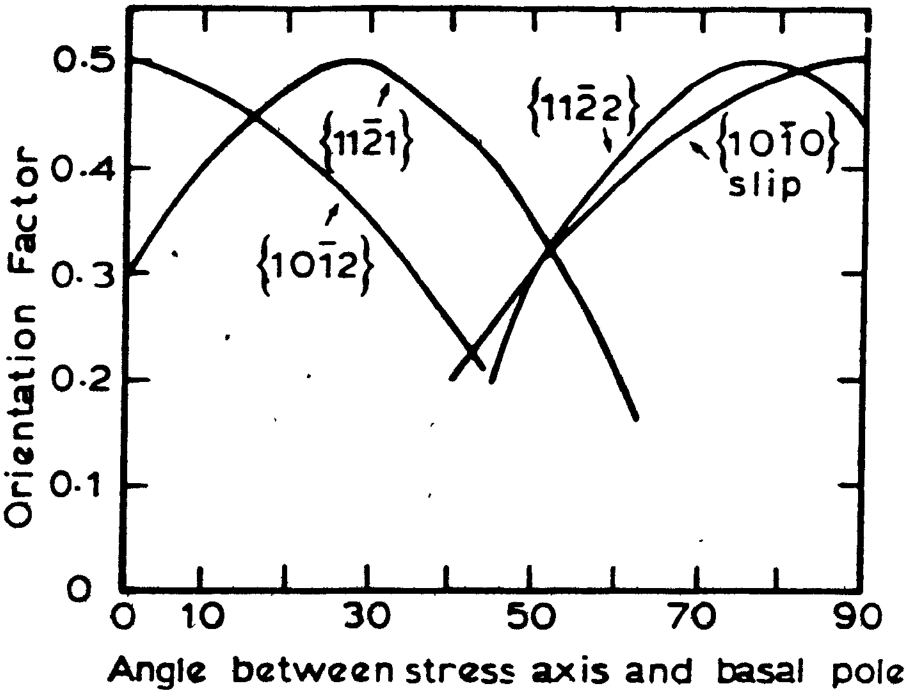

Figure 8. Orientation factors as a function of the angle between the stress axis and the basal plane pole for four modes of deformation.

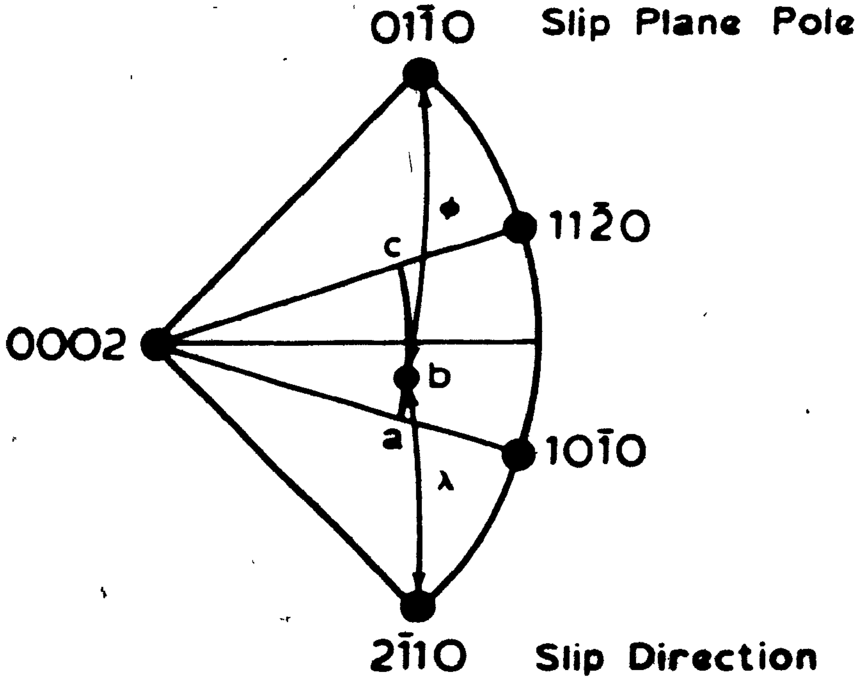

Figure 9. Schematic representation of the stress axis orientation , b, which favours prismatic slip on the (0110) [2110] slip system.

twinning increases, especially that of $\{11\bar{2}1\}$ twinning (see Fig. 4). On the other hand, it was found that during rapid straining at 77 K, all twinning mechanisms appeared to obey a resolved shear stress law and, at the same time, the resolved shear stresses for all four mechanisms apparently approached the same value. This indicates that twin nucleation is a strongly stress dependent process. It was also shown that a small pre-strain at 77 K to nucleate $\{11\bar{2}1\}$ twins followed by testing at room temperature increased the ductility of the material over a specimen deformed entirely at room temperature. This effect was attributed to the relative ease of growth of twins that were nucleated previously under conditions where high stresses had to be imposed to cause plastic flow to occur. This also emphasized the importance of introducing other modes of deformation in order to ensure plasticity.

It should be mentioned that although the $\{10\bar{1}2\}$ and $\{11\bar{2}1\}$ (tensile) twinning modes were the most frequently found, $\{11\bar{2}2\}$ (compressive) twins were also observed. The latter retwinned extensively by both $\{10\bar{1}2\}$ and $\{11\bar{2}1\}$ twinning. This behaviour was explained in terms of texture rotations brought about by the $\{11\bar{2}2\}$ twinning mode in which the material rotates into a favourable orientation for tensile twinning, whereas the rotations brought about by the two tensile twins reorient material to favour prism slip (see Fig. 5). Although no explanation for the presence of the $\{11\bar{2}2\}$ compression twins in the tensile test was put forward, their occurrence can be explained in terms of the necessity of accommodating compressive strain in directions perpendicular to the stress axis during a tensile test; thus, if some crystals are oriented with their c-axes within 60 to 90 degrees of the stress axis, there exists the possibility for $\{11\bar{2}2\}$ twinning to occur.

As the temperature was raised, an increased incidence of kinking was reported, with well defined kink bands being observed at 540 K. The nature of the lattice rotations at kink band boundaries was explained in terms of dislocations lying on the basal plane and having Burgers vectors parallel to a $\langle 11\bar{2}0\rangle$ close-packed direction. This was later confirmed by Martin and Reed-Hill,(19) who also suggested that this process was further evidence for the occurrence of basal slip as a secondary slip system in polycrystalline zirconium deformed at high temperatures. The fact that twinning was less and less frequent at higher temperatures was consistent with the view that the frequency of twin nucleation was strongly stress dependent. An important observation regarding kinking was that it occurred in compression specimens in grains where the stress axis was aligned close to the basal pole. Kinking is therefore another deformation mechanism which can lead to height reduction along the c-axis.

2.3 Deformation of Zirconium Alloys

Most of the research concerning deformation mechanisms in zirconium alloys has been directed at identification of the systems operating in an effort to explain the observed fabrication textures as well as their formation and stability. Early work carried out by Reed-Hill showed that the same mechanisms operated in Zircaloy-2 as in zirconium at room temperature. Concurrently, Picklesimer(30) described the highly anisotropic yielding behaviour of textured Zircaloy and was the first to explain this in terms of the relevant deformation mechanisms. He found that the yield strength in compression for directions which required reduction parallel to the c-axis was considerably higher (in some cases by a factor of two) than that for tension along the c-axis. He suggested that this was an indication that the stress level for $\{11\bar{2}2\}$ twinning was considerably higher than that for $\{10\bar{1}2\}$ twinning. As mentioned in the last section, $\{11\bar{2}2\}$ twinning is the predominant method for height reduction along the c-axis in unalloyed zirconium, although in zirconium alloys, this is not the only possibility.

For example, Jensen and Backofen(31) investigated the deformation and fracture behaviour of Zircaloy-4 and zirconium sheets with strong (0002) textures. They employed plane strain compression at temperatures from 298 K to 1000 K. They found that, below

600 K, Zircaloy-4 accommodated compression along [0001] by $\langle\vec{c} + \vec{a}\rangle$ slip, with dislocations mainly confined to thin bands oriented close to $\{11\bar{2}4\}$; whereas pure zirconium deformed by $\{11\bar{2}2\}$ twinning followed by second and third-order retwinning. Above 600 K, there was no essential difference in the deformation behaviour of zirconium and Zircaloy-4, both deforming by a combination of $\{10\bar{1}1\}$ twinning and $\langle\vec{c} + \vec{a}\rangle$ slip. This kind of deformation behaviour, i.e. $\{10\bar{1}1\}$ twinning and $\langle\vec{c} + \vec{a}\rangle$ slip, was also observed in specimens deformed in uniaxial compression, which eliminated the constraint inherent in the plane strain compression tests. It should be recalled that $\langle\vec{c} + \vec{a}\rangle$ slip on a system of the form $\{11\bar{2}1\}\langle 11\bar{2}3\rangle$ or $\{10\bar{1}1\}\langle 11\bar{2}3\rangle$ was induced by Tenckhoff(24) using highly constrained deformation in single crystals of zirconium. Jensen and Backofen also observed that the flow stresses in compression were considerably higher than in tension.

Lucas and Bement(32) carried out a study of the strength differential effect in the Zircaloy cladding of LWR* fuels. They suggested that the strength differential arises from the higher stress levels required for the activation of compressive deformation modes than for that of tensile modes. The strength differential is thus affected by the processing route of polycrystalline Zircaloy inasmuch

---

*Light Water Reactors

as the lattice rotations associated with cold work fabrication processes align the {0002} poles along the symmetry directions of product forms. They reported that these strength differentials were of significant magnitude even at temperatures exceeding 700 K.

Thus it seems that deformation along the c-axis can be readily accomplished in zirconium alloy by $<\vec{c} + \vec{a}>$ slip, specifically on $\{10\bar{1}1\}<11\bar{2}3>$ slip systems, rather than by twinning, and this conclusion is supported by the recent results of MacEwen et al(33) concerning the Bauschinger effect in Zircaloy-2.

From the preceding discussion it seems clear that the deformation mechanisms in zirconium and zirconium alloys depend in a complex way on the stress state, texture, composition, temperature and strain rate. These factors, taken together, make the mechanical behaviour of zirconium and its alloys a highly anisotropic one. Despite these complexities, these alloys are of great utility as engineering materials, especially in the nuclear industry. Some of the application aspects of these materials are dealt with in the following chapter.

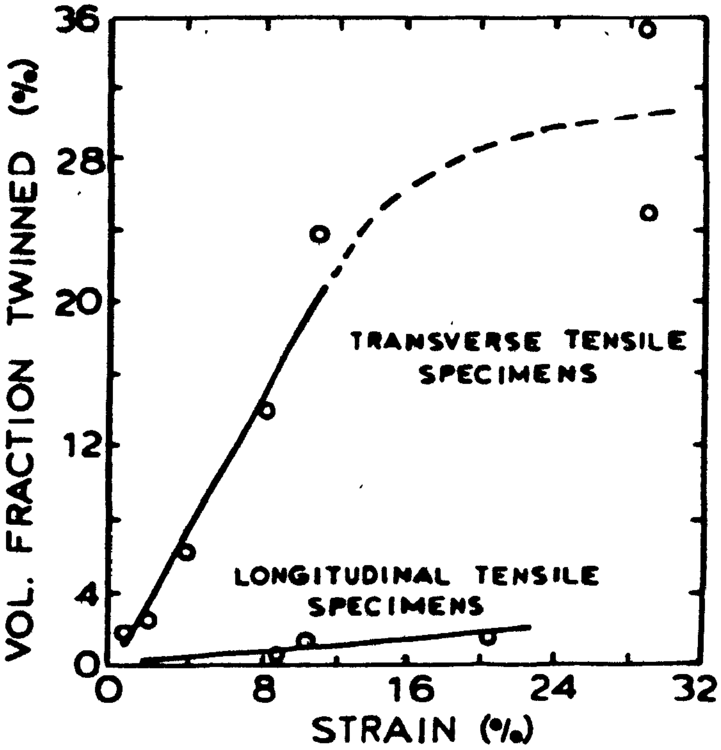

Figure 10. Volume fraction of twins as a function of strain in pure zirconium tensile specimens deformed at room temperature.

CHAPTER 3

ZIRCONIUM ALLOYS FOR PRESSURE TUBES

3.1 Environment of Operation and Design

The most valuable nuclear property of zirconium which leads to its use in nuclear reactors is its low thermal neutron absorption cross-section. This, together with its adequate corrosion resistance and strength, make zirconium a unique material for nuclear applications. The physical properties of zirconium are given in Table V. In the Canadian design of nuclear ractor (CANDU*), which is based on the use of natural uranium, the reactor core contains a complex lattice of zirconium alloy fuel channels. Uranium oxide (UO_2) is used as the fuel; it is clad in zirconium alloy tubes, and heavy water (D_2O) is employed as both moderator and coolant. The pressure tubes in the reactor core are horizontally oriented to facilitate on-power refuelling and are subjected to operation at temperatures in the range 523 to 585 K with a coolant pressure of 11.1 MPa and at a fast neutron flux of approximately $3 \times 10^{17}\ n \cdot m^{-2} \cdot s^{-1}$. In addition, the pressure tubes are subjected to a biaxial stress state produced

---

*Canada Deuterium Uranium

Table V. Typical physical properties of zirconium

Atomic number	40
Atomic weight	91.2
Density at 300 K	6.5 mg/m^3
Melting temperature	2125 K (1850°C)
Transition temperature $\alpha \rightarrow \beta$	1135 K (862°C)
Coefficient of thermal expansion at 570 K	[11$\bar{2}$0] direction 6.3 x 10^{-6}/K [0001] direction 10.4 x 10^{-6}/K
Specific heat at 300 K	276 J/Kg.K
Thermal conductivity at 300 K	20 W/m.K
Thermal neutron capture cross-section	microscopic 0.18 barn macroscopic 0.008 cm^2/cm^3
Electric resistivity	0.44 $\mu\Omega$m
Young's modulus at 300 K	[11$\bar{2}$0] direction 99GPa [0001] direction 125 GPa
Poisson's ratio at 300K	0.35
Lattice parameters at 300 K	
hexagonal α	a_o = 0.323 nm c_o = 0.515 nm
body centered cubic β	a_o = 0.359 nm

by the pressure of the coolant and the weight of the fuel bundles. The ratio of circumferential stress to axial stress is about 2.

The design criteria for pressure tubes are based on Section III of the ASME Pressure Vessel Code, although the code does not deal with zirconium alloys. The restrictions on the maximum design stress are as follows:

(1) σ < 1/3 of UTS (ultimate tensile stress)

(2) σ < 2/3 of YS (0.2% yield stress)

(3) σ < 60% of the stress estimated to give a rupture life of 100,000 hours

(4) σ < stress to give a creep rate of 10^{-7} h^{-1}

The important factor of neutron economy in the reactor core provides a considerable incentive not to reduce the stress in the tube by increasing the wall thickness. Figure 11 shows the design curves for cold worked Zircaloy-2, one of the zirconium alloys used as a pressure tube alloy, based on out-of-reactor tests. At reactor operating temperature (573 K), the lowest stress in the design curve is for 1/3 UTS which is therefore the limiting property for design. Design curves for Zr -2.5 wt% Nb alloys, another alloy used as pressure tube material, are similar but, as will be discussed later, the values for 1/3 UTS are higher.

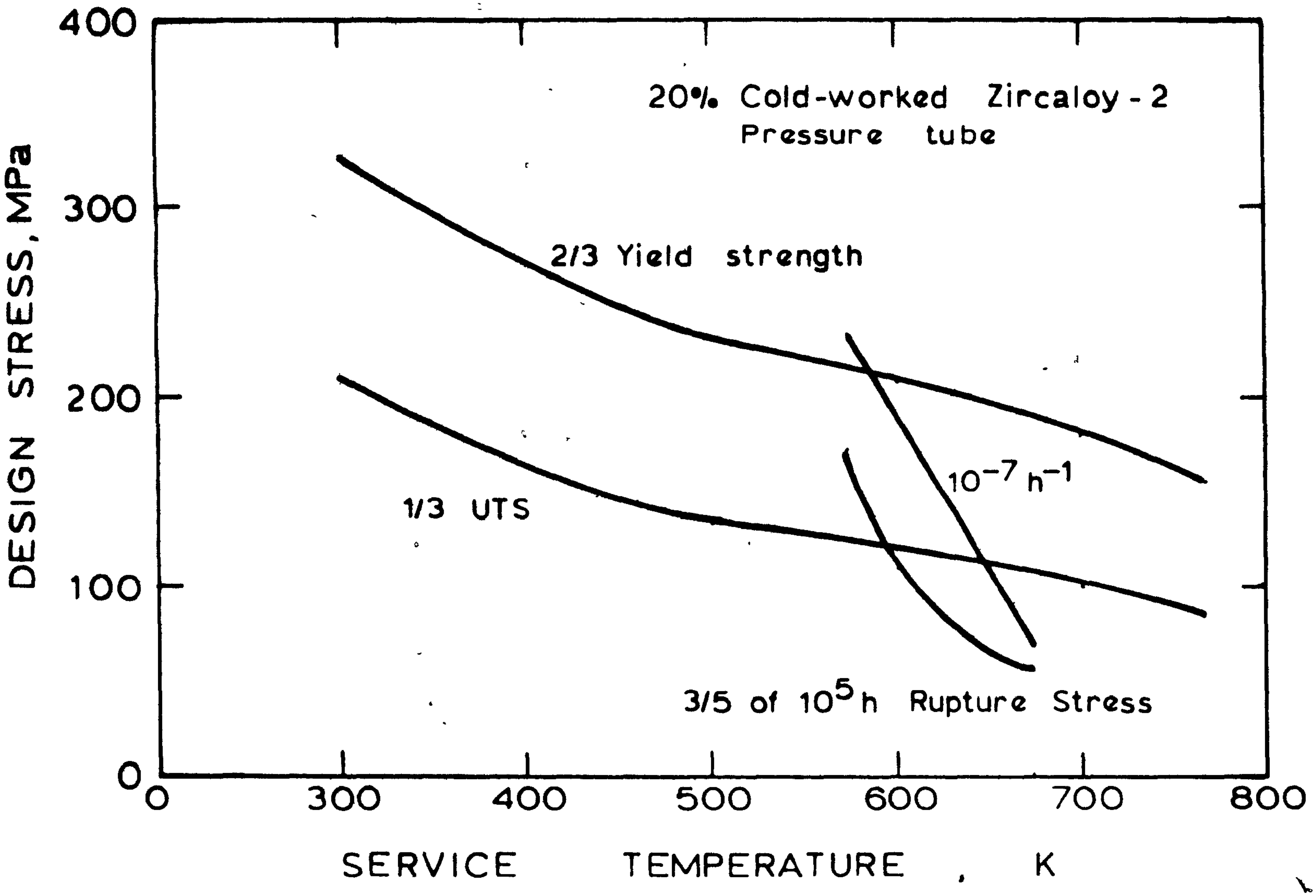

Figure 11. Design curves for 20% cold worked Zircaloy-2 pressure tube.

3.2 Fabrication

Any alloy to be used as a pressure tube material must have adequate neutron economy, satisfactory creep strength and sufficient ductility under in-reactor conditions; it must also resist corrosion by the reactor coolant. At present, pressure tubes in the following alloys and metallurgical conditions are being utilized in modern CANDU power reactors:

Alloy	Metallurgical Condition
Zircaloy-2 (Ref. 44)	Cold worked
Zr -2.5 wt% Nb (Ref. 45)	Quenched and aged
Zr -2.5 wt% Nb (Ref. 36)	Cold worked

The mechanical properties of these alloys are given in Table VI at 575 K, which is the general reference temperature for properties. The modern method of producing base zirconium of appropriate quality for nuclear applications leads to material which is almost free of inclusions, with a maximum impurity content of 3400 ppm, ~1 at.%.(34) The chemical composition specifications for Zr -2.5 wt% Nb made from such ingots are given in Table VII.

The alloy ingots are subsequently preheated to 1250 K and forged into round bars using flat and rotary forges. The bars are then machined into hollow billets suitable for extrusion. To produce a more uniform microstructure

Table VI. Pressure tube tensile properties at 565 K

Material	Test[a]	0.2% Yield Strength		Ultimate Tensile Strength		Elongation (%)	Reduction in area (%)
		MPa	kpsi	MPa	kpsi		
Cold-worked Zircaloy-2	LT	320	45	380	54	26	55
	TT	350	50	370	52	23	54
Cold-worked Zr-2.5 wt% Nb	LT	370	53	530	76	15	50
	TT	540	77	570	81	23	54
Heat-treated Zr-2.5 wt% Nb	LT	480	69	600	86	19	61
	TT	670	95	690	98	12	50

[a] Abbreviations--LT, longitudinal tensile; TT, transverse tensile.

Table VII. Chemical composition specifications for Zr-2.5 wt% Nb ingots

Alloying Elements	
Niobium	2.40 to 2.80 wt%
Oxygen	900 to 1300 ppm 5.2 to 7.4 x 10^{-1} at.%
Impurity Elements	ppm maximum (at.%)
Aluminum	75 (2.5 x 10^{-2})
Boron	0.5wt% (4.2 x 10^{-4})
Cadmium	0.5wt% (2.1 x 10^{-5})
Carbon	270 (2.1 x 10^{-1})
Chromium	200 (3.5 x 10^{-2})
Cobalt	20 (3.1 x 10^{-3})
Copper	50 (7.2 x 10^{-3})
Hafnium	50 (2.5 x 10^{-3})
Hydrogen	~~20~~ (1.8 x 10^{-1})
Iron	1500 (1.1 x 10^{-1})
Lead	130 (5.7 x 10^{-3})
Magnesium	20 (7.5 x 10^{-3})
Manganese	50 (8.3 x 10^{-3})
Molybdenum	50 (4.8 x 10^{-3})
Nickel	70 (1.1 x 10^{-2})
Nitrogen	65 (4.2 x 10^{-2})
Silicon	120 (3.9 x 10^{-2})
Tantalum	200 (1 x 10^{-2})
Tin	100 (7.7 x 10^{-3})
Titanium	50 (9.5 x 10^{-3})
Tungsten	100 (4.9 x 10^{-3})
Uranium	3.5 (1.3 x 10^{-4})
Vanadium	50 (9 x 10^{-3})

and to refine the grain size, either the forged bars or the machined billets are beta quenched from 1290 K. The billets are Cu clad to prevent excessive oxidation.(35) At 1200 K, the preheating temperature for extrusion, Cu and Zr form a low-melting point eutectic and thin sheet steel is used as a diffusion barrier between the zirconium alloy and the copper. Another advantage of Cu cladding is that it provides a surface that is receptive to lubricants; this is important because zirconium alloys are prone to galling.

In the case of cold worked Zircaloy-2 and Zr -2.5 wt% Nb, the extruded tubes are cold drawn in two passes, each of approximately 12 to 15% reduction in area, at drawing speeds of less than 25 $mm\cdot s^{-1}$. After this, the pressure tubes are stress relieved in an autoclave for 24 hours at 675 K. This process also produces a hard adherent oxide layer on the tubes. On the other hand, heat treated Zr -2.5 wt% Nb extrusions(36) are water quenched from 1150 K, cold drawn in one step of approximately 12% reduction in area, and aged at 775 K for 24 hours.

3.3 Mechanical Properties

3.3.1 Effect of heat treatment

Typical mechanical properties of Zircaloy-2 and Zr -2.5 wt% Nb alloy in various heat treated conditions are given in Table VIII. As can be seen, heat treatment of Zircaloy-2 does not improve the strength of the alloy. The higher strength of quenched Zircaloy-2 as compared to the slow cooled material is partially due to the finer effective grain size of the Widmanstätten structure produced. By contrast, Zr - 2.5 wt% Nb in the β- or (α + β)-quenched condition is much stronger than in any other condition because of the presence of the martensitic α'-phase. Aging this structure at 775 K has only a minor effect on the strength of the alloy (see Fig. 12). This is because:

(i) β-Nb precipitates, leading to an increase in strength;

(ii) there is concurrent recovery of α', resulting in a decrease in strength, and in a small effect on the mechanical properties.

The effect of time at high temperatures is also shown in Fig. 12. Here it can be seen that when the α' phase is heated into the (α + β)-phase region (870-1170 K), it rapidly transforms to α (with little Nb in solid solution) and β (enriched with Nb). This results in a considerable decrease in hardness and strength.

Table VIII. Typical room temperature tensile properties of Zircaloy-2 and Zr-2.5 Wt% Nb

Alloy	Material Condition	0.2% Y.S kpsi	0.2% Y.S MPa	UTS kpsi	UTS MPa	%El	%RA
Zircaloy-2	slow-cooled from 1025K (750 C)	48	330	72	500	22	40
	slow cooled from 1275K (1000 C)	48	330	63	470	22	35
	water quenched from 1275K (1000 C)	68	470	84	580	16	50
	20% cold worked	80	550	85	590	30	45
	40% cold worked	85	590	90	620	10	35
Zr-2.5 wt% Nb	slow cooled from 1125K (850 C)	50	350	74	510	28	48
	slow cooled from 1275K (1000 C)	76	520	89	610	13	46
	water quenched from 1275K (1000 C)	106	730	115	790	9	38
	water quenched from 1125K (850 C)	109	750	120	820	14	60
	20% cold worked	85	590	90	620	15	46
	40% cold worked	90	620	100	690	13	50

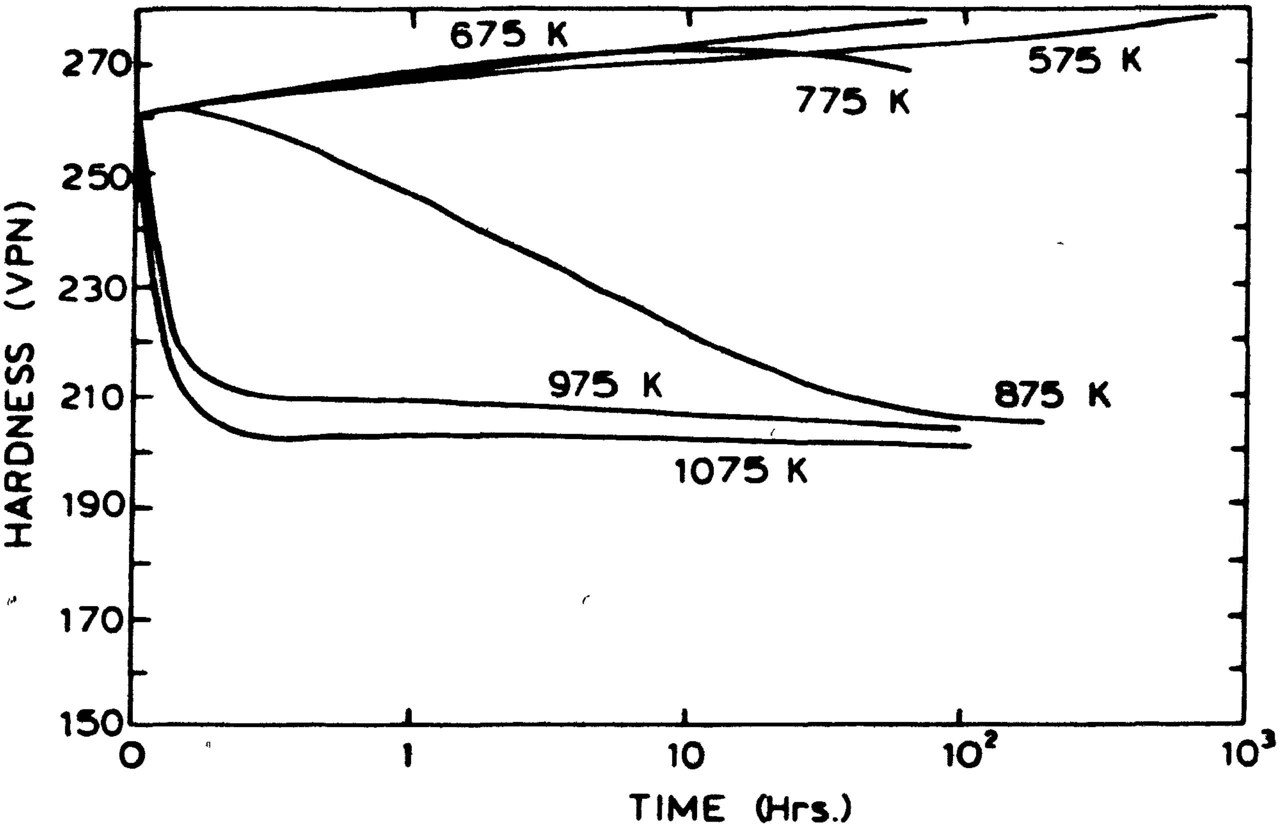

Figure 12. Effect of heating at different temperatures on the hardness of Zr-2.5 wt% Nb water-quenched from 1155 K.

3.3.2 Effect of cold work

Cold work increases the strength of Zircaloy-2 and Zr -2.5 wt% Nb due to the increase in dislocation density. Table VIII, as well as Figs. 13 and 14, show the effects of cold work on the mechanical properties of the two alloys.

3.3.3 Effect of grain size

Figure 15 shows the effect of grain size on the yield stress of hot worked Zr -2.5 wt% Nb.(43) As can be seen, the latter can be increased to 520 MPa by decreasing the grain size. The flow stress of zirconium alloys follows the Petch equation:

$$\sigma = \sigma_i + kd^{-1/2} \qquad (3.1)$$

where σ is the flow stress, σ_i is the flow stress of a single crystal, k is the grain boundary strengthening coefficient and d is the grain size.

3.3.4 Age hardening, recovery and recrystallization

Zirconium alloys used in the fabrication of pressure tubes are usually stress relieved at 675 K after cold drawing. At this temperature, any change in the strength of the pressure tube alloy is due to recovery. Recovery is a thermally activated process and is affected by the amount of prior deformation by cold work, the direction of the internal stresses and the crystallographic texture of the

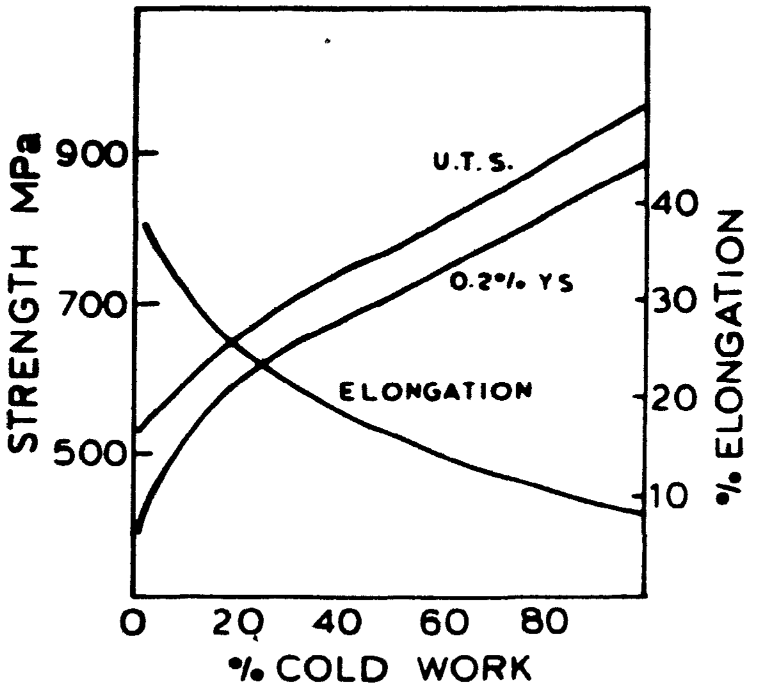

Figure 13. Effect of cold work on the tensile strength of Zr-2.5 wt% Nb alloy.

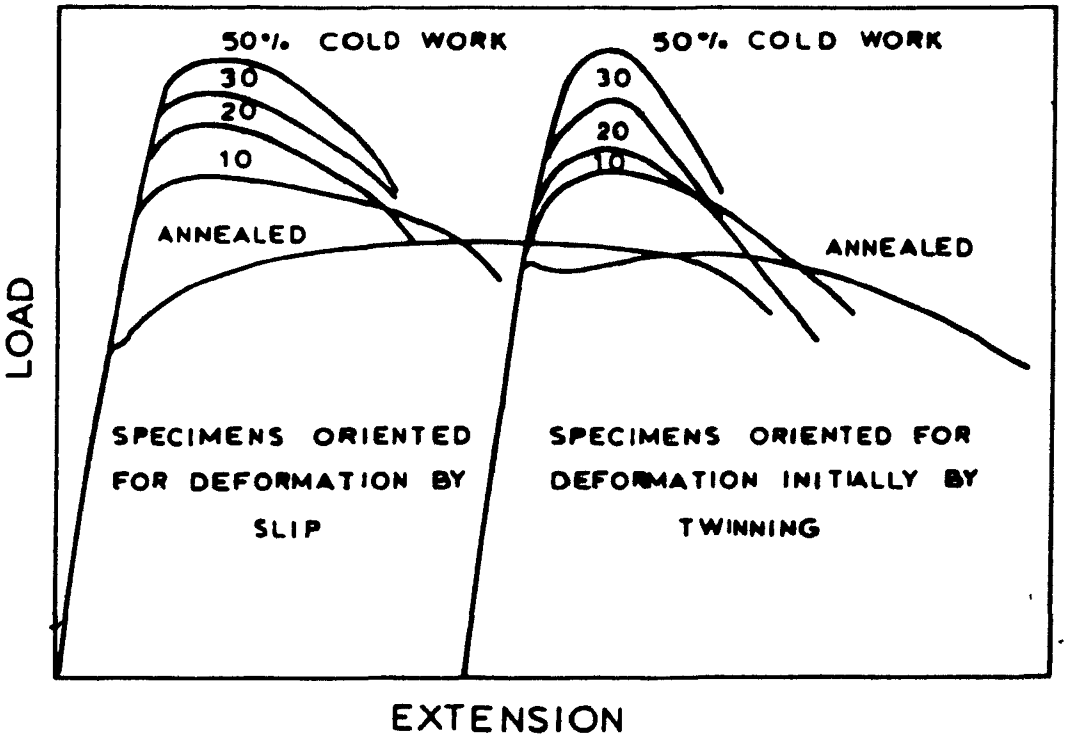

Figure 14. Effect of cold work on the tensile proportions of Zircaloy-2.

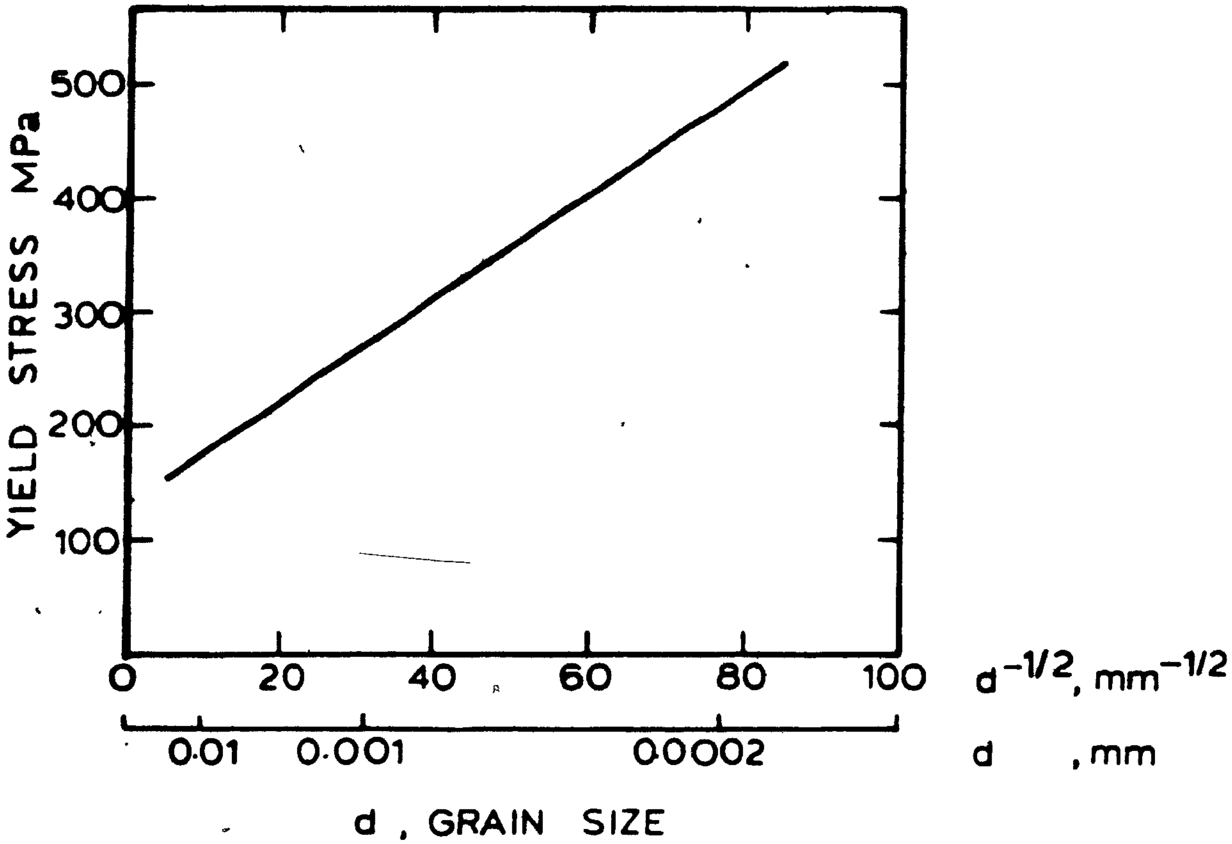

Figure 15. Effect of grain size on the 0.2% yield stress of hot worked Zr-2.5 wt% Nb alloy.

alloy. Figure 16 shows the width of the (0004) α-phase diffraction peaks of cold worked Zr -2.5 wt% Nb. It is readily seen that, at 575 K, recovery is very slow, while at 775 and 875 K, there is rapid partial recovery followed by changes at a much smaller rate. It is evident that the higher the temperature, the greater the initial recovery. In order to obtain full recovery in times less than thousands of hours, it is required to heat the material to temperatures above 875 K.

The rate of recovery is also increased by increasing the amount of cold work (Fig. 17). Ells and Cheadle(42) have shown that textures also affect recovery. Figure 18 shows the mechanical properties of 40% cold worked Zircaloy-2 as a function of temperature and of the orientation of samples made from rolled sheet with a pronounced initial texture. As can be seen, short transverse specimens hardened after heating in the range 575-775 K. This increase in strength was partially attributed to a Bauschinger effect which arises from the reversal of the stress state in a tensile test on samples taken from the short transverse direction of the rolled sheet. In addition, this effect was also attributed to a small amount of age hardening which had a greater effect when deformation was initially by twinning rather than by slip. The results for 40% cold rolled Zr -2.5 wt% Nb were similar but more pronounced (Fig. 19). The yield stress of the short transverse specimens was decreased below that of the longitudinal and transverse specimens due to the Bauschinger effect. However, after work hardening, the UTS's were in the order expected from the texture of the specimens, with the short transverse the strongest and the longitudinal the weakest. All the specimens age hardened in the temperature range 575-775 K and again the effect was larger in specimens that initially deformed by twinning.

Such age hardening in Zr -2.5 wt% Nb alloy has been attributed(43) to the increase in strength of the Nb-rich cubic β-phase when ω plates form within it. The ω then behaves as a fibre strengthening phase.

The isochronal recovery and age hardening of a 20% cold worked tube is shown in Fig. 20. At 575 and 675 K, the increase in the hardness of the grain boundary β-phase is greater than the recovery of the α-phase and there is a small overall increase in hardness. Above 875 K, the recovery of the α-phase is the dominant factor and there is an overall softening. Recrystallization usually only starts when recovery is almost complete; i.e. after many hours at 875 K or after a few minutes at 1075 K.

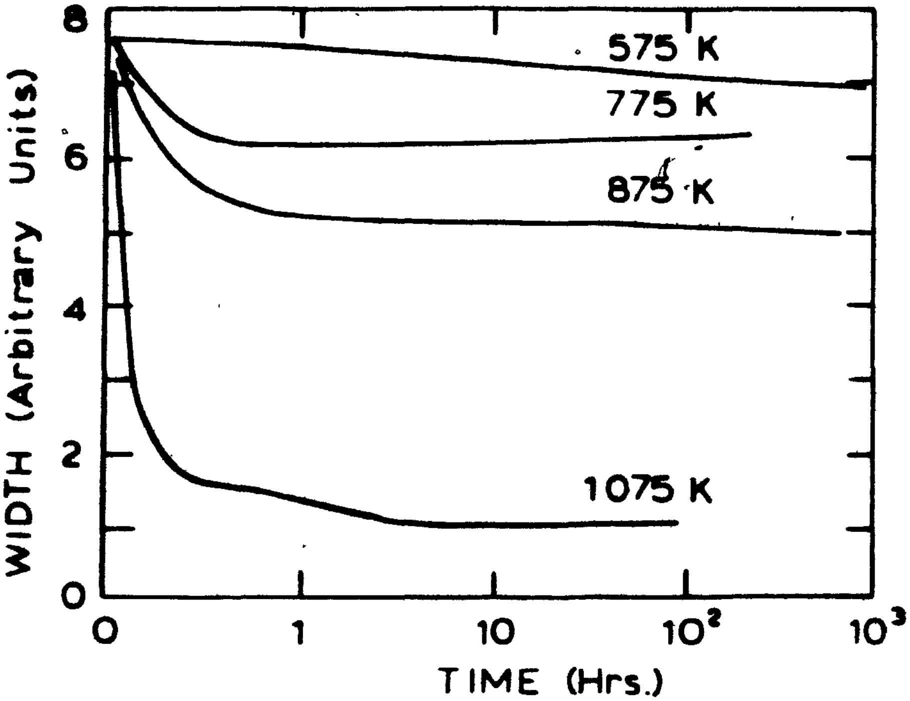

Figure 16. Width of the (0004) X-ray diffraction peak of 20% cold worked Zr-2.5 wt% Nb alloy after heating at different temperatures.

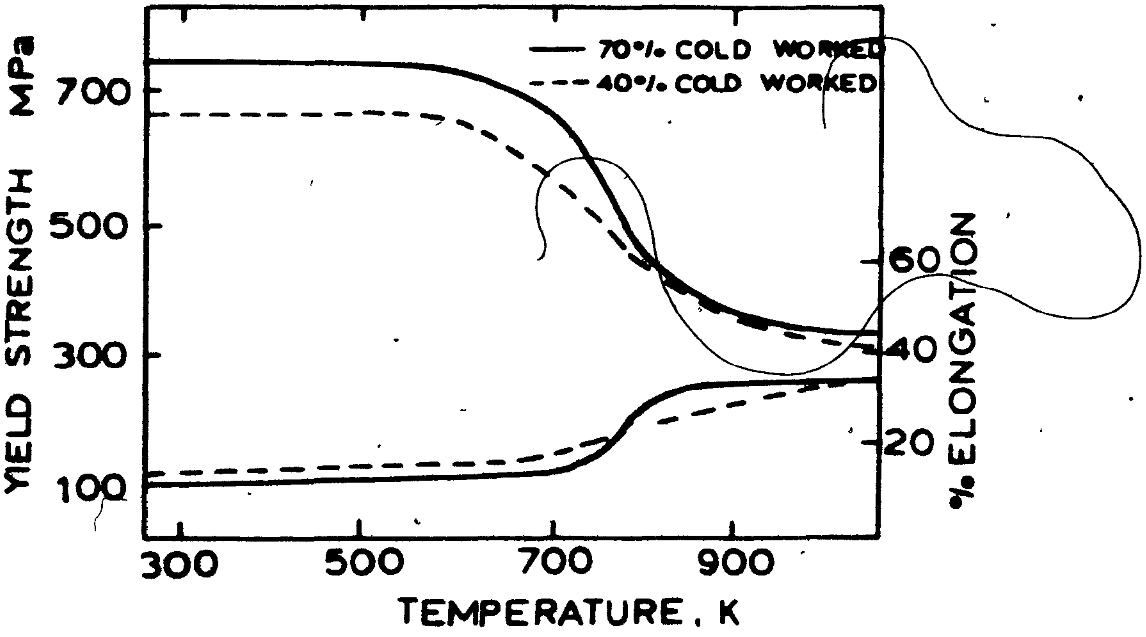

Figure 17. **Effect of heating for 1 hour on the tensile properties of 70% and 40% cold worked Zircaloy-2.**

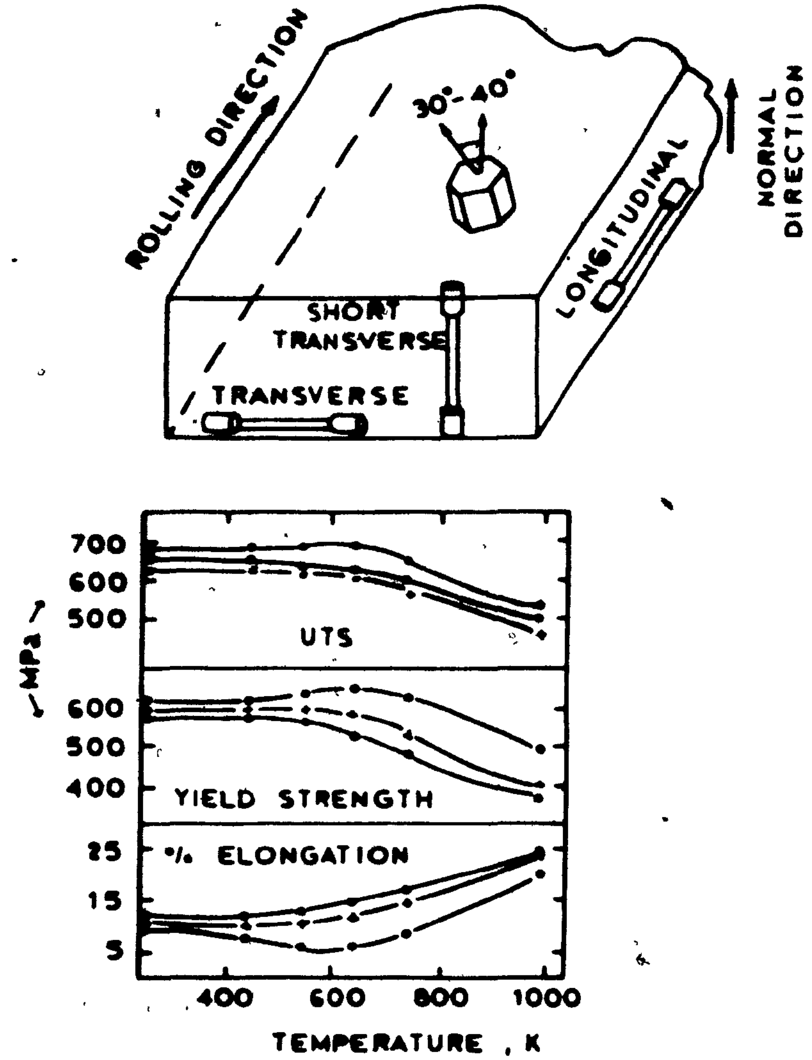

○ Short Transverse specimens, deformation initially by twinning.

+ Transverse specimens, deformation by twinning and slip.

● Longitudinal specimens, deformation by slip.

Figure 18. Effect of heating for 1 hour on the tensile properties of 40% cold worked Zircaloy-2 sheet.

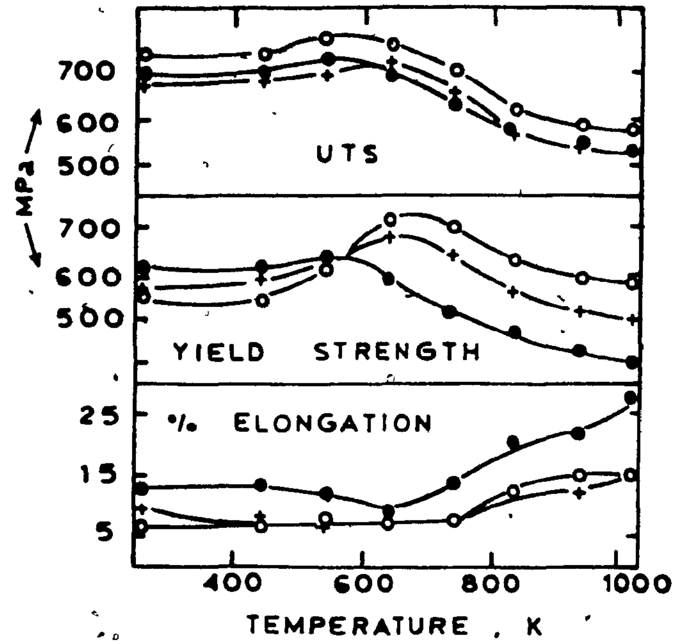

Figure 19. Effect of heating for 1 hour on the tensile properties of 40% cold worked Zr-2.5% Nb alloy.

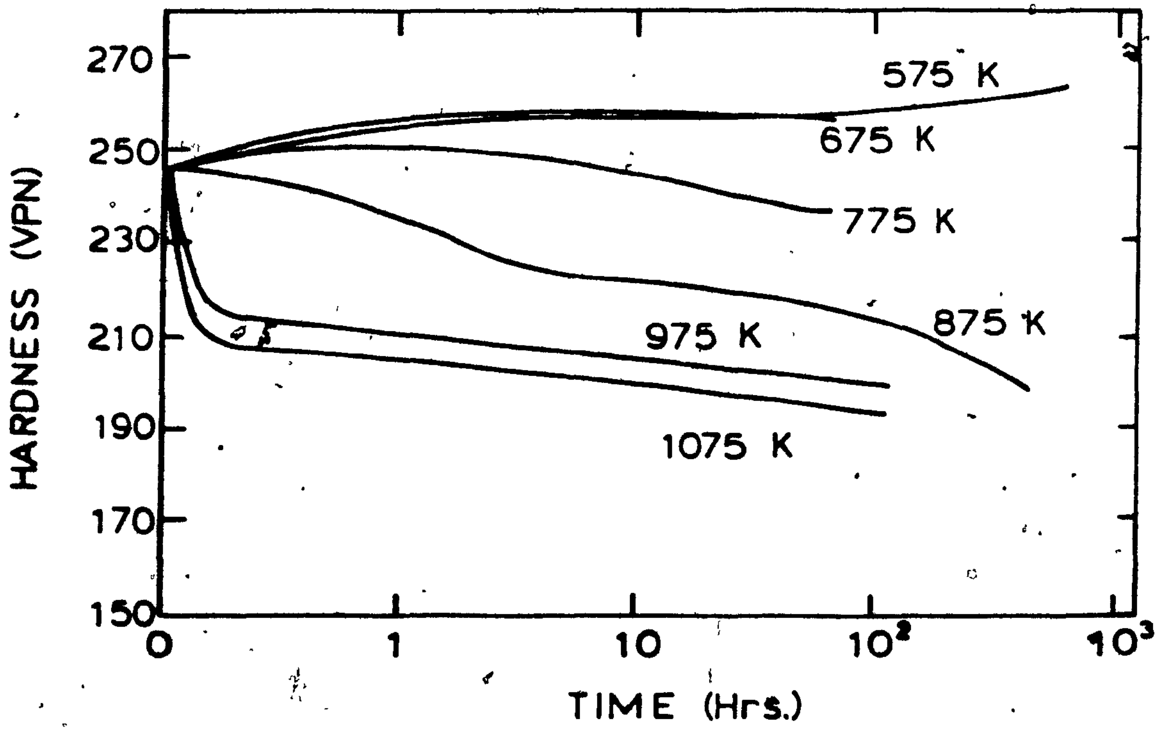

Figure 20. Effect of heating at different temperatures on the hardness of a 20% cold worked Zr-2.5 wt% Nb pressure tube.

3.4 Metallurgical Properties of Zirconium Alloy Pressure Tubes

In this section, the metallurgical properties of zirconium alloy pressure tubes will be discussed in terms of the effects that operating conditions, such as neutron irradiation, impose on the performance and service life of the pressure tubes.

3.4.1 Creep and growth

Irradiation creep arises from the application of an external non-hydrostatic stress during irradiation. This applied stress causes the evolving microstructure to interact with the irradiation produced point defects in an anisotropic way. Irradiation growth, on the other hand, only occurs in crystallographically anisotropic materials and requires the response of the evolving microstructure to be naturally anisotropic in the absence of applied stress.

The mechanisms by which irradiation creep occur have been extensively discussed by Bullough and Wood.(46) They conjectured four fundamental mechanisms:

a) Stress induced preferred absorption (SIPA) of the point defects on dislocations;

b) Stress induced preferred nucleation (SIPN) of point defects in planar aggregates (edge dislocation loops);

c) Stress induced climb and glide (SICG) of the dislocation network;

d) Stress induced gas driven interstitial deposition (SIGD).

The phenomenon of neutron enhanced creep is the life-limiting criterion for zirconium alloy pressure tubes. Figure 11 shows the design stress data for cold-worked Zircaloy-2. As can be seen, for temperatures above 620 K, creep strength becomes the limiting factor in the design stress of the tubes.

The secondary creep rate of pressure tubes operating over a range of conditions in CANDU-PHW and -BLW reactors has been correlated$^{(47,48)}$ with neutron flux, temperature and stress as follows:

$$\dot{\varepsilon}_t = K \cdot 10^{-25} \cdot \sigma_t \cdot \phi \cdot (T - 160°C) \qquad (3.2)$$

where $\dot{\varepsilon}_t$ = diametral creep rate, h^{-1}

σ_t = diametral stress (60 - 200 MPa)

ϕ = fast-neutron flux (from 10^{13} to 3.5×10^{13} $n \cdot cm^{-2} s^{-1}$ < 1 MeV)

K = constant = 5.8 cold worked Zircaloy-2

2.1 cold worked Zr -2.5 wt% Nb

3.2 heat treated Zr -2.5 wt% Nb

In the conventional expression for creep at a given temperature,

$$\dot{\varepsilon} = c \cdot \sigma^{n} \cdot t^{m-1} \qquad (3.3)$$

under in-reactor conditions, at low stress, n is close to 1 for all the three materials. Hence such creep deformation is described as 'superplastic.'(48,49) The tendency to necking and flow localization is reduced and high ductility is obtained. Also, the secondary creep rate as described by Eq. (3.2) is independent of time, i.e. m (Eq. 3.3) is 1. Considering that the equation only applies for high neutron fluxes, then as the flux approaches zero, the creep rate and the time exponent "m" must approach the values for out-of-pile tests, which is about 0.3 for the latter.(50)

As will be discussed later, zirconium alloys develop very strong crystallographic textures, which in the case of extruded and drawn pressure tubes consist of grains with basal poles in the circumferential and radial directions. Results from biaxially stressed tubes have been correlated with uniaxially stressed specimens(52) with a stress adjustment factor based on preferred slip on the prism planes. A continuum mechanics approach was also used(53) to derive anisotropy constants for uniaxial and biaxial loading.(47,54) To satisfy boundary conditions, the uniaxial transverse creep rate must be lower than the longitudinal creep rate.

From the above analysis it may be concluded that cold worked Zr -2.5 wt% Nb has the best creep characteristics and results show that the diametral strain of a pressure tube fabricated from this alloy is likely to be less than 3% after 40 years of service.

3.4.2 Mechanical strength and ductility

The effect of neutron irradiation on the yield strength and tensile strength of cold worked Zircaloy-2 and Zr -2.5 wt% Nb was extensively studied by Langford(57) and Ells and Fidleris.(54) Table IX shows typical values for uniaxial and biaxial strength for unirradiated and irradiated zirconium alloys. It is apparent that irradiation increases both the uniaxial strength, either yield or tensile, and the biaxial burst strength. Note that, typically, the biaxial strength is up to 15% higher than the uniaxial tensile strength in isotropic materials because plastic deformation is inhibited by the superimposed longitudinal stress (= 0.5 hoop stress); however, in zirconium alloys, the biaxial strength may be increased by up to 20% above the uniaxial strength because of the additional influence of anisotropic deformation modes.

The reduction in ductility due to irradiation is also shown in Table IX. The different behaviour of Zircaloy-2 compared with Zr -2.5 wt% Nb is also evident. Zircaloy-2 bulges considerably during the 575 K burst test, producing high diametrical elongations, which are reduced after irra-

Table IX. Burst test properties of zirconium alloy pressure tubes at 565 K

Material	*	0.2% Yield Strength MPa	kpsi	Burst Strength MPa	kpsi	Elongation %	Reduction in area %
cold-worked	U	420	60.0	450	63.0	28	35
Zircaloy-2	I	550	78.0	550	78.5	7.5	12-17
cold-worked	U	530	75.0	600	85.0	3-7	30
Zr-2.5 wt% Nb	I	770	110.0	780	111.0	1	15-17
heat treated	U	650	92.0	770	109.0	2-5	20
Zr-2.5 wt% Nb	I	101.2	114.0	1100	157.0	1	14

* U is unirradiated - I is irradiated

diation. Bement[56] has explained this behaviour as follows. Irradiated cold worked Zircaloy-2, with a texture oriented for $(10\bar{1}2)$ twinning in tension, i.e. the circumferential direction in the tube, generally shows an abrupt yield point in uniaxial tension tests at 575 K. This is attributed to mobile dislocations sweeping channels free of defects; i.e., the moving dislocations absorb defects and thus reduce the stress required to move the dislocations that follow. The situation after yielding is therefore unstable, since the stress to initiate plastic flow exceeds the stress necessary to maintain the flow. In the irradiated pressure tube under biaxial stress, plastic flow can commence if a local stress concentration (usually at the thinnest wall section) reaches the yield stress, after which flow can continue unstably until the local stress is relieved. Failure will occur at this point while the remainder of the tube has barely yielded, as shown by the reduction in transverse elongation during burst tests of irradiated tubes. Under operating conditions, the stress in the tube is only one third of the unirradiated longitudinal tensile strength, and plastic instability does not represent a problem.

In the case of Zr -2.5 wt% Nb pressure tubes, bulging does not occur during the burst test, the circumferential elongation is relatively low and irradiation reduces it slightly. This behaviour has been attributed[56] to the greater restraints on deformation imposed by the higher strength of this alloy.

The reduction in area at fracture in all the three alloys (Table IX) remains relatively large after irradiation. This is in part responsible for the very good flaw tolerance of pressure tubes.

3.5 Fabrication Textures and their Influence on the Mechanical Properties

To take full advantage of the anistropy of mechanical properties exhibited by zirconium alloys one has to be able to understand its origin and in this way to control it. The only way to understand the anisotropic mechanical properties is in terms of the crystallographic texture of the material. In this way, correlations between anisotropy and fabrication practice, stress-strain behaviour, etc. are possible.

The first observations concerning preferred orientation in zirconium were made by McGeary and Lustman.(56) They determined the texture of thin zirconium sheet as a function of fabrication history. Their results showed that cold rolling produces a texture consisting of basal planes parallel to the rolling direction with basal poles oriented at ±30 degrees from the transverse direction and no basal plane poles parallel to the rolling direction.

Hot rolling below the recrystallization temperature did not alter the final texture.

The texture formed by cross-rolling consisted of basal planes in the rolling plane with $\langle 10\bar{1}0\rangle$ directions located in one direction in the sheet (rolling or transverse) and the $\langle 11\bar{2}0\rangle$ directions located in the other.

Recrystallization of the cold rolled texture resulted in a 30 degree rotation about the c-axis placing the $\langle 11\bar{2}0\rangle$ directions in the rolling direction. Recrystallization of the cross rolled texture resulted in a switching of the $\langle 10\bar{1}0\rangle$ and $\langle 11\bar{2}0\rangle$ directions in the sheet.

An important result brought about by the crystallographically reversible nature of the α-β phase transformation, which has an orientation relationship(57) $(0001)_{\alpha} \| (110)_{\beta}$, $(11\bar{2}0)_{\alpha} \| (111)_{\beta}$, is that, although α-recrystallization annealing rotates the texture in the basal plane, the basal texture is not altered unless the material is cycled through the α-β transformation.

Textures in zirconium alloy tubes have been extensively investigated.(23,22,57,58) Most of this research has shown that the textures produced in the fabrication of tubing are dependent on the details of the fabrication procedures used, including types of equipment, extrusion ratios, die angles, mandrel dimensions and angles, reduction per pass, number of passes between anneals, changes in wall thickness vs. circumferential reduction in each operation, etc.

Picklesimer$^{(60)}$ carried out an extensive research program on the textures developed during tube forming operations. He pointed out the importance of prior processing on tube textures and performed an analysis of the deformation in various tube forming operations. Essentially, he concluded that the textures developed by fabrication methods other than rolling can be rationalized and estimated from a knowledge of the rolling textures if an approximate plane strain condition exists during fabrication and the plane of strain can be identified. Figure 21 shows the strain states and orientations of unit lattice cells, both before and after deformation for rolling and several tube production processes.

The kind of analysis Picklesimer proposed can only be carried out in terms of ideal orientations and, since texture formation also depends on prior processing, the results are consequently only approximate. Nevertheless, this concept is particularly useful when the textures can be related to mechanical properties. This is done in terms of the basal plane normal, which is the hard direction in the HCP structure. Thus the textures of different tubes can be compared in terms of the basal plane orientations. Figure 22 shows several such ideal orientations and their representation in both direct and inverse pole figures.

These ideal orientations are the result of a simpli-

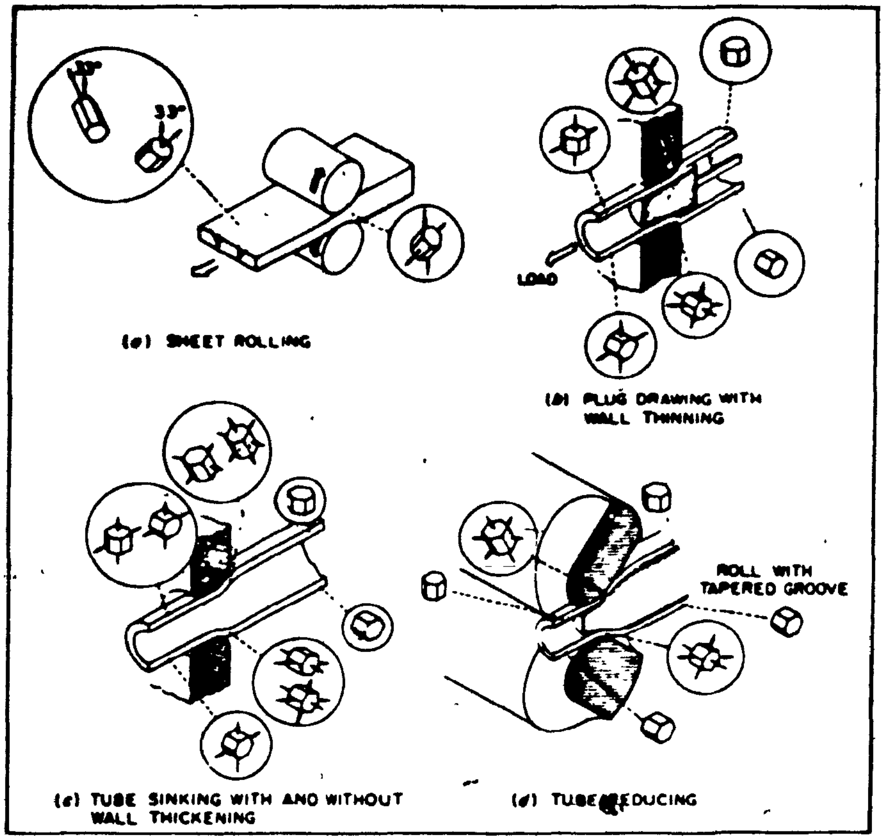

(a) SHEET ROLLING

(b) PLUG DRAWING WITH WALL THINNING

(c) TUBE SINKING WITH AND WITHOUT WALL THICKENING

(d) TUBE REDUCING

Figure 21. Strain states for various types of fabrication of zirconium alloy pressure tubes.

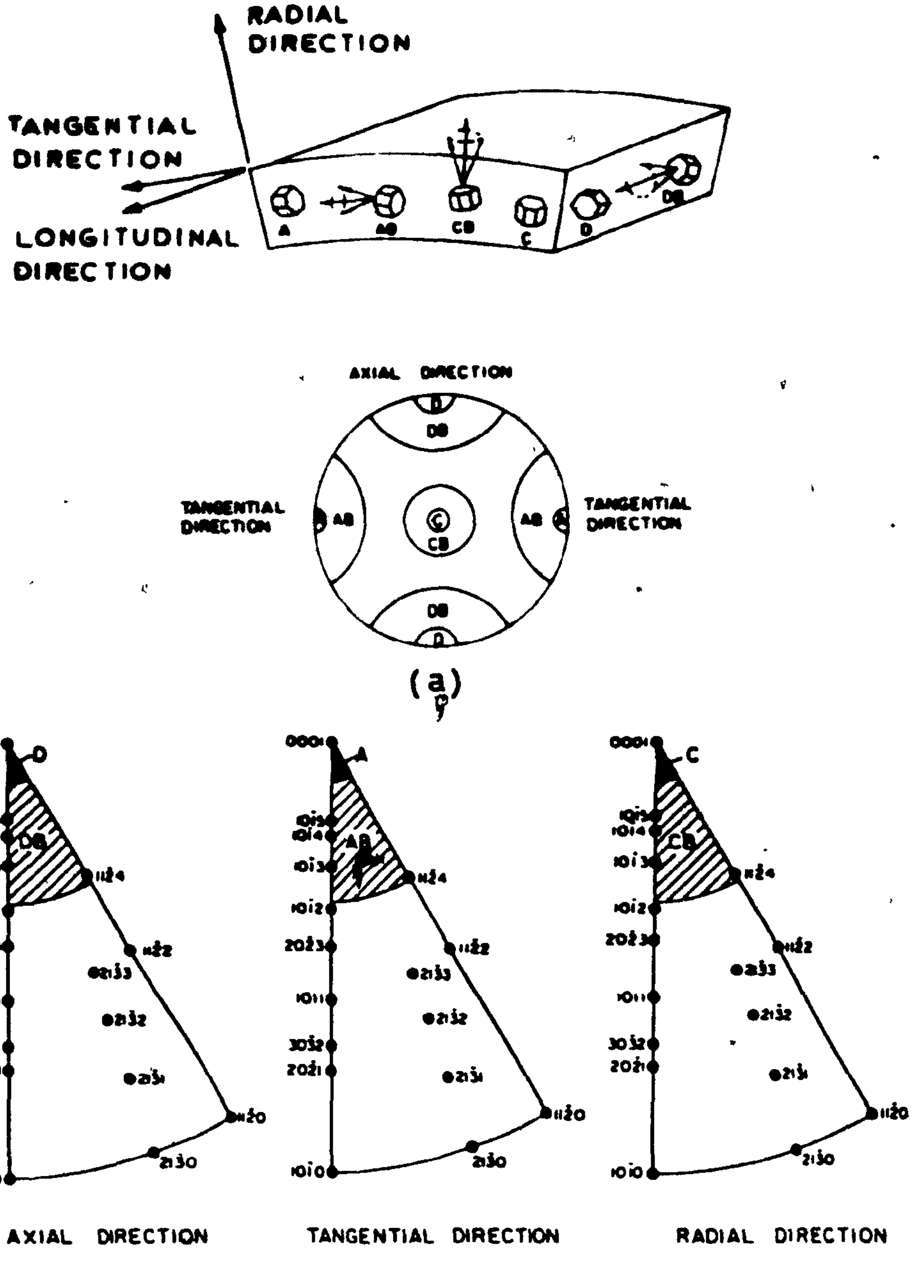

(a)

(b)

Figure 22. Ideal orientations in zirconium alloy tubes plotted on direct (a) and inverse (b) pole figures.

fication of the observed textures and in the case of zirconium alloy tubes the textures observed consist of basal poles concentrated in the radial direction (C, Fig. 22), in the tangential direction (A, Fig. 22), in both directions, or in orientations within 40 degrees from the radial or tangential directions (CB and AB respectively, Fig. 22). These are the commonly observed textures detected in cold worked pressure tubes. However, Cheadle and Ells(59) have shown that basal poles can also be found in the axial direction or within 40 degrees from it in heat treated Zr -2.5 wt% Nb, but not in Zircaloy-2 (D and DB, Fig. 22).

Texture coefficients can be given to the idealised orientations for the quantitative comparison of tubes. A texture coefficient is the relative number of crystallographic planes parallel to a given surface compared to the number in a random sample. The larger the value the more intense is the texture and a texture coefficient of one denotes random orientation. Table X gives a summary of reported textures in tubes of zirconium, Zircaloy-2 and Zr -2.5 wt% Nb in terms of ideal orientations and texture coefficients.

One of the important observations which led to the above rationalization of textures in zirconium alloys was that, in any case, the stable texture observed consisted of basal planes parallel to the direction of maximum tensile

Table X. A summary of reported textures of tubes of Zircaloy-2, Zr-2.5 wt% Nb and zirconium

Manufacturing method and material		Texture coefficients					
		A	AB	CB	C	DB	D
as extruded	Zircaloy-2	A/AB>C/CB					
as extruded, plug drawn		A/AB>C/CB					
as extruded, zirconium and Zircaloy-2		A/AB>C/CB					
as extruded, cold drawn (NPD production) Zircaloy-2		A/AB>C/CB					
as extruded, and cold drawn 56.8%	Zircaloy-2	4	3	3	2	-	-
as extruded, and cold swaged 74.7%		-	-	3	4	-	-
as extruded, and cold drawn (NPD production) Zircaloy-2		2.7	1.4	1.6	1.3	-	-
as extruded, Zr-2.5 wt% Nb		6.2	1.5	4.2	3.3	-	-
as extruded, Zr-2.5 wt% Nb plus water quenched from 880°C, aged 500°C		3.3	0.7	0.7	-	-	2.0

...cont'd

Table X--cont'd

Manufacturing method and material		A	AB	CB	C	DB	D
		Texture coefficients					
extruded and cold-drawn Zr-2.5 wt% Nb		1.3	1.5	3.7	2.1	-	-
extruded and cold-drawn	Zircaloy-2	A/AB<C/CB					
extruded and tube reduced		A/AB∼C/CB					
extruded and cold drawn Zircaloy-2		A/AB∼C/CB				-	-
extruded and cold drawn Zr-2.5 wt% Nb		A/AB>C/CB				-	-
extruded and cold drawn Zr 2.5 wt% Nb, plus water quenched 1000°C, aged 5 h at 500°C		A/AB>C/CB				D/DB > C/CB	
extruded	Zircaloy-2	8	-	2	-	-	-
extruded and tube reduced		3	2	-	2	-	-
extruded and tube reduced plus cold drawn		3	3	-	-	-	-
extruded and cold drawn	Zircaloy-2	2.4	2.7	1.9	3.3	-	-
extruded and tube reduced		1.1	1.0	3.7	5.0	-	-
extruded and tube reduced		8.1	2.4	1.3	2.3	-	-

strain and basal poles predominantly in the direction of maximum compressive strain; when a "plane strain" condition can be identified in a given process, this leads to possible textures which are analogous to those obtained in rolling.

Many attempts have been made to explain the stable texture in zirconium alloys by considering the available deformation mechanisms. As pointed out in Chapter 2, the formation and stability of the texture can be explained in terms of a sequence of twinning operations involving at least six different sets of twins.(22) A much simpler explanation was suggested by Picklesimer,(23) who assumed that slip in $\langle 11\bar{2}3\rangle$ directions could occur. This direction occurs on $\{10\bar{1}0\}$, $\{10\bar{1}1\}$, $\{11\bar{2}1\}$, and $\{11\bar{2}2\}$ planes (see Fig. 23) and cross slip should be possible between the slip systems. These slip systems would produce a strain component perpendicular to the basal plane. No large changes in basal pole orientations are required when these slip systems operate, and the developed texture should remain essentially the same on further rolling.

Ballinger(27) suggested that the incorporation of $\langle \vec{c} + \vec{a} \rangle$ slip into the deformation process would explain the observed texture and stability of rolled plate by using a single twinning operation, $\{10\bar{1}2\}$, and prismatic slip. Essentially, he proposed that for an initially random texture and for reduction by uniaxial compression, the

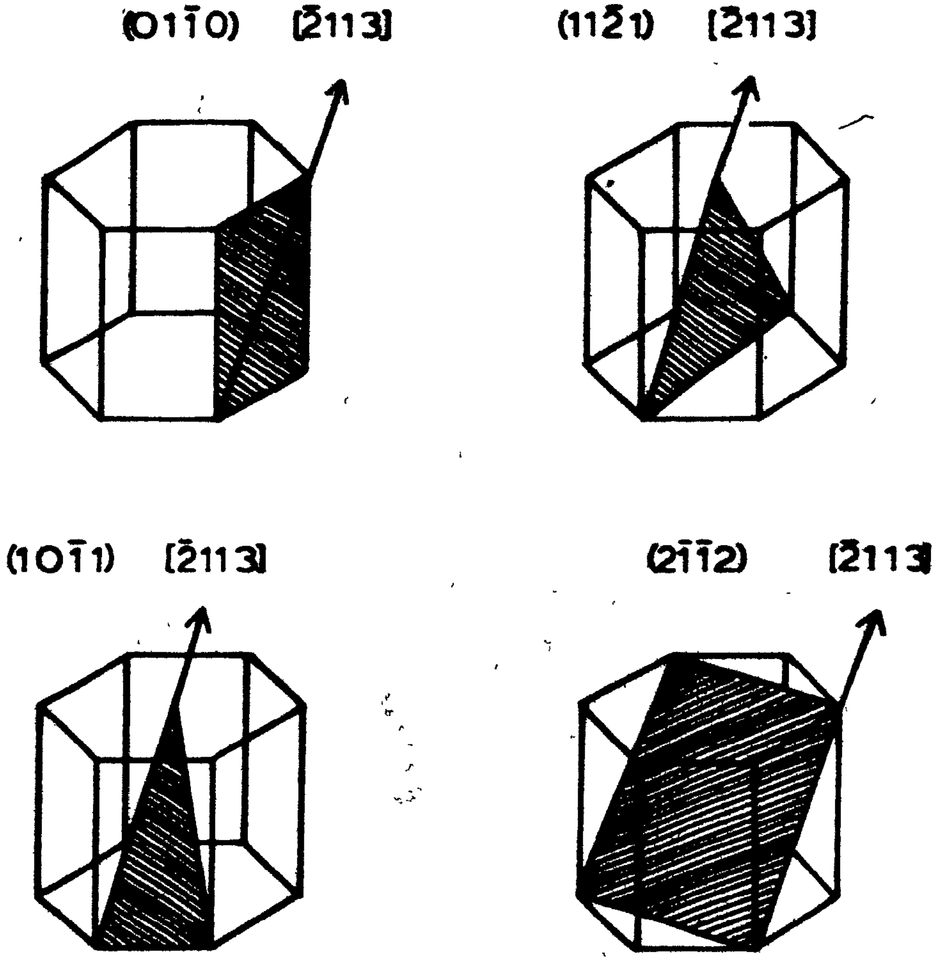

Figure 23. Possible slip planes for pyramidal slip with a $\langle \vec{c}+\vec{a} \rangle$ Burgers vector.

operation of $\{10\bar{1}2\}$ twinning, which would occur in grains with basal poles located within 45 degrees of the rolling or transverse directions, would rotate the basal poles by ~85 degrees, resulting in a pole distribution which is symmetrical about the plane normal and cut off at approximately 45 degrees to the rolling and transverse directions. After this initial deformation and the formation of the initial texture, the operation of slip in the two systems mentioned above acts to sharpen the texture. Prism slip accounts for most of the large axial extensions in the rolling direction and $\langle \vec{c} + \vec{a} \rangle$ slip would be responsible for the through thickness reduction. The action of the $\{10\bar{1}0\}\langle 11\bar{2}0\rangle$ systems is to reorient the basal plane into the rolling direction while rotating the $\langle 10\bar{1}0\rangle$ directions into the rolling direction as well. This rotation to $\langle 10\bar{1}0\rangle$ in the rolling direction is the result of conjugate slip on $\{10\bar{1}0\}\langle 11\bar{2}0\rangle$ systems (the $\langle 10\bar{1}0\rangle$ direction bisects the angle between $\langle 11\bar{2}0\rangle$ directions).

The angle between the $\{10\bar{1}1\}$ planes and $\{0002\}$ planes is ~60 degrees and compressive strains on $\{10\bar{1}1\}\langle 11\bar{2}3\rangle$ systems rotate the slip plane such that it will approach the normal to the compression axis. The two slip operations act to distort the initially symmetric texture to the observed final texture consisting of one with no basal poles in the rolling direction and a spread of poles peaked in the normal transverse plane at approximately 30-40 degrees to the transverse direction.

The basal planes will be parallel to the rolling plane with a $\langle 10\bar{1}0\rangle$ direction in the rolling direction. The large axial strains in the rolling direction tend to eliminate any rotation of basal poles into the rolling direction through the $\{10\bar{1}1\}\langle 11\bar{2}3\rangle$ slip operation.

The above model of texture formation and stability can be applied to tube forming operations if an appropriate "plane strain" condition can be identified in the fabrication process. In addition, an equivalence must be established between the radial, axial and circumferential directions in the tube and the normal, rolling and transverse directions in the plate respectively. However, tube fabrication processes are more complicated than rolling, with stress states which are much harder to define and with superimposed shears and redundant deformations.

3.6 Development of Zirconium Alloys

One way of markedly improving the thermal efficiency of water-based reactors is by raising the outlet coolant temperature from 575 K to 675-725 K. This would produce a higher efficiency of energy conversion in turbines fed with superheated steam. A second method involves the thermal neutron efficiency of the reactors, which can be improved by decreasing the wall thickness of the pressure tubes.

Hence there exists an incentive for the development of zirconium base alloys for use in heavy water reactors designed to operate at higher coolant pressures and temperatures. Such investigations fall under the theme of the development of high temperature creep resistant alloys, although the behaviour of reactor alloys is of course complicated by neutron flux effects.

Wilcox(61) has suggested an empirical relationship which could take into account the factors that control the tensile strength of refractory metal alloys at high temperatures:

$$\sigma = \sigma_o + f\left(\frac{Gb}{\lambda}\right) + f\left(\left|\frac{1}{a}\,\frac{\delta a}{\delta c}\right|\right) + f\left(\left|\frac{1}{G}\,\frac{\delta G}{\delta c}\right|\right) + \sigma_{SRO}$$

$$+ f(Gb\rho^{1/2}) + f(d^{-1/2}) + f(\sigma_f V_f) \qquad (3.4)$$

where G is the shear modulus and b is the Burgers vector for mobile dislocations, and the other symbols are defined below. By analyzing this equation, it is possible to see that the high temperature (creep) strength, σ, developed in a matrix of base strength σ_o is promoted by:

(1) Small precipitate spacing, λ;

(2) High solution hardening due to the atomic misfit parameter $\left|\frac{1}{a}\,\frac{\delta a}{\delta c}\right|$;

(3) An increase in shear modulus by alloying. (Douglas(62) determined that Nb additions tend to

reduce both the elastic and shear moduli at room temperature);

(4) An increase in short range order in the alloy, and therefore in σ_{SRO} ;

(5) An increase in the stable dislocation density, ρ;

(6) A small mean grain diameter, d (this effect depends not only on d but also on the effective grain boundary immobilization);

(7) Introduction of a significant volume, V_f, of fiber reinforcement; σ_f.

Williams(64) carried out a very complete review of the factors mentioned above and the extent to which different alloy elements can contribute to σ in equation (3.4). Table XI lists the characteristics of several alloying elements which are attractive in terms of strengthening potential and neutron absorption. These alloying elements contribute to the last five terms of Eq. (3.4); furthermore, alloys containing these elements can be strengthened by thermal and mechanical processing techniques. Alloys containing β-stabilizing elements can be quenched from the β-phase or high in the $(\alpha + \beta)$-phase field to produce a fine twinned martensite structure which is supersaturated in β-stabilizing elements and has a very fine effective grain size. This structure can be further hardened by aging to precipitate the β-stabilizing elements.

Table XI. Possible alloying additions for α-zirconium based alloys for nuclear applications

Element	Effect of 1 At% Addition on Cross Section	Effect of Addition on Phase Stability	Strengthening Mechanism
Tin	1.7%		
Aluminum	1.8%	Stabilize HCP α-Phase	Solution Strengthen α-Phase
Lead	-0.4%		
Molybdenum	13%	Stabilize BCC β-Phase	Solution Strengthen β-Phase. Precipitation Strengthen α-Phase
Niobium	6.6%		
Silicon	-0.1%	Very low Solubility	Solution Strengthening

The effects of combinations of these alloying elements have been studied by Williams et al (65) and Ibrahim et al. (66) Aluminium and lead, although effective α-solution strengtheners, are very detrimental to the corrosion resistance of α-Zr in water. Silicon has very little effect on the properties unless its concentration in the alloy is large. It was found that Nb, Mo and Sn were the most promising alloying additions.

The present work deals with the anisotropic mechanical behaviour of one of these alloys which was the result of an intense research program undertaken at Chalk River Nuclear Laboratories, AECL, in 1969. This alloy was designated to replace the Zircaloy-2 and Zr -2.5 wt% Nb alloys in current use as pressure tube materials in future power nuclear reactors and has been named "Excel". The composition of this alloy was specified as:

Element	wt% Element
Sn	3.5
Mo	0.8
Nb	0.8
O	1100 ppm
H	20 ppm
Zr + impurities	Balance

Tin is an alpha stabilizer and is particularly attractive as an alloying addition because:

(1) It has a low neutron capture cross section;

(2) Zr_4Sn precipitates should be stable for dispersion hardening;

(3) It reduces stacking fault energy, which makes cross slip more difficult and increases the strength;

(4) It reduces the grain boundary migration rate, which should increase creep resistance at high temperatures.

A great deal of information about the short term (strength, microstructure, texture) and long term (corrosion, delayed hydrogen cracking, creep and growth) properties of Excel alloy has been obtained since the alloy was devised as a potential pressure tube material and the major outcomes of this research will now be discussed.

Cheadle et al(67) made a comparative study of Excel alloy in two different metallurgical conditions, namely 5% cold worked and annealed. Both materials were extruded at 13:1 into tubes and then cold drawn 5%. The cold worked material was stress relieved at 675 K for 24 h while the second material was annealed at 1023 K for 30 min and then stress relieved at 675 K for 24 h. Table XII gives the microstructural characteristics of the two materials together with some comparative information for Zr -2.5 wt% Nb.

The microstructure of the 5% cold worked tube consis-

Table XII. Effect of fabrication details on the grain thickness and dislocation density of Excel alloy pressure tubes

Tube Type	Tube No.	% Cold Drawn	Grain Thickness, mm x 10^{-3}	Dislocation Density, m^{-2}
Excel extrusion	248	0	...	3×10^{14}
	248	2.0	0.74	
	250	3.7	0.62	
5% cold worked Excel	252	3.2	0.64	3.4×10^{14}
	253	2.8	0.58	
	254	4.4	0.62	
	249	2.9	0.80	
Annealed Excel	251	2.9	0.74	1.4×10^{14}
30% cold-worked Zr-2.5 Nb	...	25 to 30	0.2 to 0.4	5 t0 9 $\times 10^{14}$
Extruded Zr-2.5 Nb	...	0	0.2 to 0.6	0.8 to 2 $\times 10^{14}$

ted of elongated α-grains, a thin boundary network of cubic β-phase, and a few localized areas of martensitic α'. The thickness of the alpha grains in the radial direction was determined to be 0.58 to 0.74 μm. The annealed microstructure, on the other hand, consisted of relatively equiaxed α-grains with the cubic beta phase concentrated at grain corners. As can be observed from Table XII, the dislocation density of both the extruded and cold worked tubes was higher than that of the extruded Zr -2.5 wt% Nb.

A low dislocation density and equiaxed grain structure are desirable for improving in-reactor creep and growth.(69) This condition was obtained in the annealed Excel pressure tube. As far as texture is concerned, it was found that the majority of the α-grains were oriented with their basal plane poles close to the tangential direction. The resolved fraction of alpha grains oriented in this direction was slightly higher than in cold-worked Zr -2.5 wt% Nb.

Table XIII gives a comparison of the average tensile properties of the Excel pressure tubes and typical tensile properties of 30% cold worked Zr -2.5 wt% Nb and CANDU-PHW minimum specifications. As can be seen, 5% cold worked Excel is very much stronger than 30% cold worked Zr -2.5 wt% Nb, while the annealed tubes are almost as strong as Zr -2.5 wt% Nb and still meet the tensile specifications for CANDU-PHW pressure tubes. It was also found that although the corrosion resistance of Excel tubes is about

Table XIII. Average tensile properties of Excel pressure tubes and typical tensile properties of 30% cold worked Zr-2.5 wt% Nb pressure tubes

Alloy	Tube Condition	Test Temperature K	Test Direction	0.2% Yield Stress, MPa	Ultimate Tensile Strength, MPa	% Elongation
Excel	extrusion	575	longitudinal	495	535	10
	5% cold-drawn	575	longitudinal	525	580	12
			transverse	620	645	13
		300	longitudinal	736	845	12
			transverse	930	965	9
	annealed	575	longitudinal	385	500	19
			transverse	490	550	13
		300	longitudinal	615	745	17
			transverse	815	840	17
Zr-2.5 Nb	30% cold-drawn (average tube)	575	longitudinal	380	520	15
			transverse	540	600	12
		300	longitudinal	640	790	13
			transverse	...	810	15
	CANDU-PHW minimum specifications	575	longitudinal	330	479	12

one half that of cold worked Zr -2.5 wt% Nb, their hydrogen absorption behaviour may be similar. As a result, an additional corrosion allowance on the inside of Excel pressure tubes of 0.2 mm was suggested, which was estimated to be consumed over the 30-year life of a reactor.

The most probable cause of a crack forming in a pressure tube is delayed hydrogen cracking. It has been suggested(70) that the stress to reorient hydrides in Excel is about three times higher than in Zr -2.5 wt% Nb, so that cracking should be much harder to initiate in Excel. However, when delayed hydrogen cracking does start, the cracks are likely to travel about ten times faster in Excel alloy than in Zr -2.5 wt% Nb. Critical crack length determinations for "leak without break" show Excel to be as safe as Zr -2.5 wt% Nb.

One of the most important findings about Excel alloy is its resistance to in-reactor creep and growth. It has been determined(69) that very elongated alpha grains and high dislocation densities, while making a large contribution to the tensile strength, are very deleterious to in-reactor creep and growth. Cheadle et al(67) found that annealed Excel with a more equiaxed grain structure and a lower dislocation density have creep rates which are less than a third that of Zr -2.5 wt% Nb and about 60% that of 5% cold worked Excel alloy.

Table XIV gives a comparison of the relative creep strengths of Excel and Zr -2.5% Nb tubes. As can be seen, the differences observed between the longitudinal and transverse deformation rates are similar for the two alloys, which indicates that the creep anisotropy of the Excel tubes should be similar to that derived for cold worked Zr -2.5 wt% Nb.

The last important characteristic of Excel is related to its thermal neutron capture cross section. It has been determined(71) that the capture cross section of Excel is initially higher than that of Zr -2.5 wt% Nb, but since the capture cross-sections of Sn and Mo decrease with irradiation due to transmutation, the average cross-section of Excel over 30 years is 13% less than that of Zr -2.5 wt% Nb. Table XV gives a comparison of the properties of annealed Excel and cold worked Zr -2.5 wt% Nb.

This analysis indicates that Excel is a superior alloy for pressure tubes. However, there is as yet no commitment to use these tubes in a power reactor, a development which is partially due to the relatively satisfactory performance of the Zr -2.5 wt% Nb alloy.

Table XIV. Relative creep strength of Excel and Zr-2.5 wt% Nb tubes after 2300 h at 573 K and 2.0×10^{17} n·m·$^{-2}$s^{-1} (E>1 MeV)

Material	Specimen Orientation	K Relaxation Rate Constant, h^{-1}	Creep Rate Relative to Cold-Worked Zr-2.5 Nb
Annealed Excel	longitudinal	0.63×10^{-4}	0.32
	transverse	0.40×10^{-4}	0.28
5% cold-worked Excel	longitudinal	1.01×10^{-4}	0.51
	transverse	0.70×10^{-4}	0.49
30% cold-worked Zr-2.5 Nb	longitudinal	$1.98 \pm 0.37 \times 10^{-4}$	1.0
	transverse	$1.44 \pm 0.10 \times 10^{-4}$	1.0

Table XV. Comparison of the properties of annealed Excel and cold worked Zr-2.5 wt% Nb

Property		c.w. Zr-2.5% Nb	Annealed Excel
Neutron capture cross section cm^2/cm^3 average over 30 years service		0.00916	0.00918
UTS at 575 K, MPa (longitudinal) front end (Specification for c.w. Zr-2.5 wt% Nb is 479 MPa, minimum)		517 ± 40^1	500^2
Corrosion allowance		0.10 mm	0.20 mm
Dimensional changes after 30 years in CANDU-PHW 600 MW	Diameter	3.9 %	1.1 %
	Length	2.5 %	0.8 %
Delayed Hydrogen Cracking			
K_{IH} (MPa $\sqrt{m}$ or $m^{-1/2}$)		~10	~10
Stress (MPa) to initiate a crack at a 0.1 mm notch at 525 K		250	500
Relative crack velocity		1	10
Stress to reorient hydride into radial/axial plane, MPa		255	690
Critical crack length at 295 K and 120 MPa hoop stress (100 ppm H)		45 mm	~50 mm

...cont'd

Table XV, cont'd

Property	c.w. Zr-2.5% Nb	Annealed Excel
Rolled joints	403 SS end fittings	standard 403 SS end fitting satisfactory

1. 95% limits for Pickering 3 and 4 tubes
2. Tubes 249 and 251

CHAPTER 4

DESCRIPTION OF MATERIALS AND EXPERIMENTAL EQUIPMENT AND TECHNIQUES

4.1 Experimental Material

The base material utilized in this study came from a batch of Excel pressure tubes fabricated at Chase Nuclear Ltd. These tubes form part of an extensive research and development program undertaken at the Chalk River Nuclear Laboratories of Atomic Energy of Canada Ltd. concerned with the development of higher strength pressure tube alloys for CANDU-BLW and -PHW reactors.* The fabrication route for the tubes is shown in Fig. 24 and the chemical analysis of both the ingot from which the tube was fabricated as well as the pressure tube itself are given in Tables XVI and XVII respectively. Although some segregation of the Sn to the bottom and top of the ingot occurred, the chemical composition of the ingot can be seen to be relatively homogeneous. Of greater importance is the observation that the impurity levels in the ingot are

---

*Canada Deuterium Uranium; Boiling Light Water; Pressurized Heavy Water.

EXTRUSION

extrusion ratio : 11:1
temperature : 1130 K

COLD DRAWING

reduction in cross-sectional area : 25%

ANNEALING

vacuum annealing
temperature : 1013 ± 15 K
time : 30 minutes
cooled in vacuum to less than : 323 K

STRESS RELIEF ANNEALING

temperature : 673 K
time : 24 hours

Figure 24. Fabrication route for the Excel alloy pressure tube utilized in this study.

Table XVI. Chemical composition of the ingot from which the pressure tube was fabricated

	Spec. %	Top %	Middle %	Bottom %	Average %
Sn	3.2-3.8	3.53	3.39	3.68	3.53
Mo	0.6-1.0	0.76	0.77	0.75	0.76
Nb	0.6-1.0	0.77	0.81	0.77	0.78
O	900-1600 ppm	1120	1090	1140	1117
H	20 ppm	5	5	5	5

Table XVII. Chemical analysis for the front and back ends of the pressure tubes

Sample No.	Oxygen ppm	Hydrogen ppm	Sn %	Mo %	Nb %
592 F	1120	14	3.70	0.80	0.71
592 B	1210	24	3.95	0.91	0.82

below the specified limits. By contrast, the gradient in chemical composition from the front to the back of the tube is greater and may be the result of the extrusion process.

The fabrication route was selected in order to improve the metallurgical characteristics of previously fabricated Excel pressure tubes,(67) particularly the crystallographic texture. The cold work and the annealing heat treatment were chosen to produce the smallest possible equiaxed alpha grains which, as discussed above, should lead to better in-reactor dimensional stability. The effect of cold work and annealing temperature on the thickness of alpha grains in Excel alloy(72) is shown in Table XVIII. As can be observed, the grain thickness decreases as the amount of cold work is increased up to 30% and as the annealing temperature is decreased. For these reasons the tube was annealed at 1013 K for 30 minutes and cold worked by 25%. Figure 25 shows an electron micrograph of the front end of the pressure tube utilized to carry out the present study. The dislocation density of the tube, although dependent on the position within the tube from which the sample was taken, was determined to be about 1.4 x 10^{14} cm^{-2}, which is much less than that of cold worked Excel and Zr -2.5 wt% Nb pressure tubes. This low dislocation density also improves the in-reactor dimensional stability of the tube.(69)

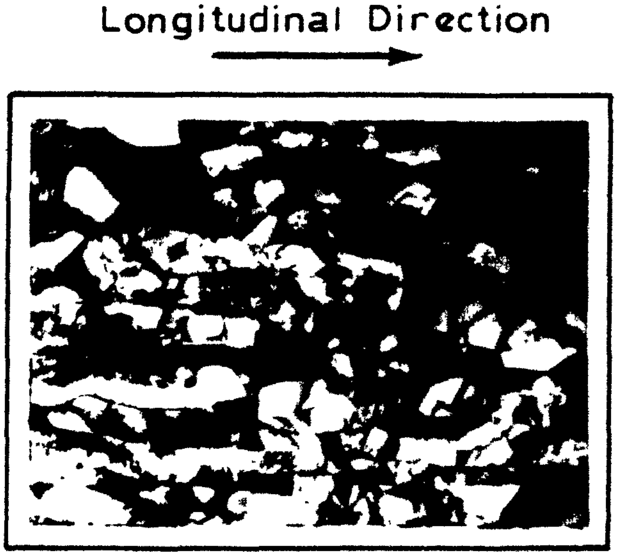

FIGURE 25 Electron micrograph of the Excel alloy pressure tube utilized in this study. 25% cold worked and annealed at 1013 K for 30 min. X 11450

Table XVIII. The effect of cold work and annealing temperature on the thickness of α grains in Excel pressure tubes

% Cold Work	Thickness of α Grains x 10^{-3} mm		
	30 minutes at 1025 K	30 minutes at 1050 K	30 minutes at 1075 K
5	0.79	0.87	1.08
10	0.72	0.85	-
20	0.59	0.74	0.98
30	0.53	1.07	1.05
40	1.11	1.05	1.72

4.2 Crystallographic Texture

The crystallographic texture of the tube utilized in this investigation was determined using the reflexion method developed by Schultz.(73) This involves examining three specimens representing the three directions of principal strain during fabrication; i.e., the axial, radial, and tangential directions in the present case. In what follows a brief description of the technique and the method of representation, direct pole figure, will be given.

4.2.1 Direct pole figure representation

As mentioned in Chapter 3, the crystallographic texture of a polycrystalline material can be expressed quantitatively by a texture coefficient (TC) which is defined as the number of reflecting crystallographic planes of a given type and orientation divided by the number of reflecting planes of that type and orientation in a textureless or "random" sample of the same material; i.e.

$$TC_{(hkl)} = \frac{N_{(hkl)}}{N_{R(hkl)}} \qquad (4.1)$$

where $TC_{(hkl)}$ = texture coefficient for crystallographic planes of a given type and orientation.

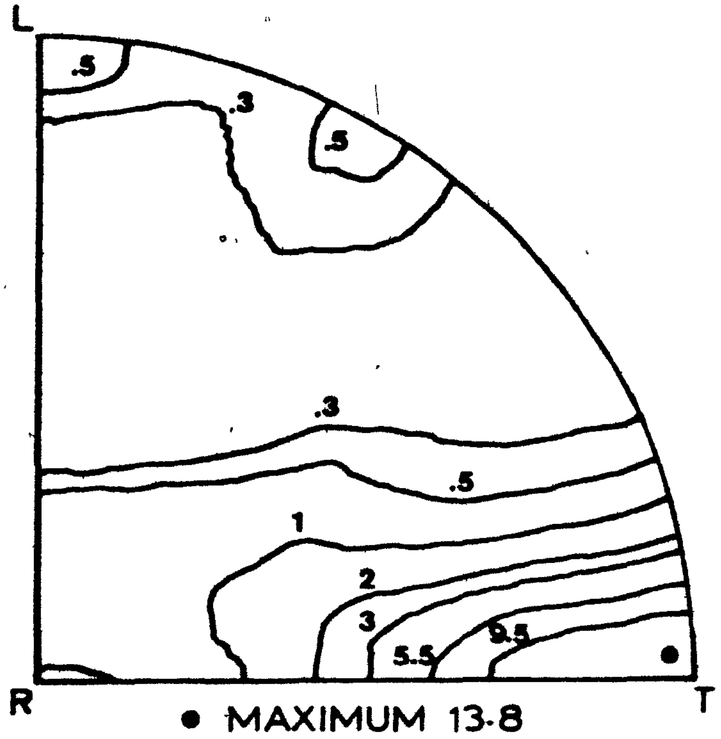

Figure 26. Average (0002) pole figure for seven Excel alloy pressure tubes (Ref. 67).

$N_{(hkl)}$ = number of crystallographic planes of type (hkl) in a given orientation in a textured material.

$N_{R(hkl)}$ = number of crystallographic planes of type (hkl) in a given orientation in a random sample of the same material.

The texture coefficients for the (0002) plane for seven Excel alloy pressure tubes determined by Cheadle et al$^{(67)}$ are illustrated in Fig. 26. It is evident that the basal plane texture coefficients are concentrated near the tangential or circumferential direction, which means that the majority of the alpha grains are oriented with their basal plane normals close to that direction.

4.3 Mechanical Testing

4.3.1 Experimental equipment

The compression testing system utilized in the present work consisted of a 100 KN MTS* close-loop electrohydraulic testing machine interfaced with a PDP 11/04 minicomputer. A CENTORR model M60 front loading furnace for high temperature operation in vacuum was used for the tests at high temperatures. Figure 27 shows an exterior view of the compression system while Fig. 28 gives an internal view of

---

*Material Testing Systems

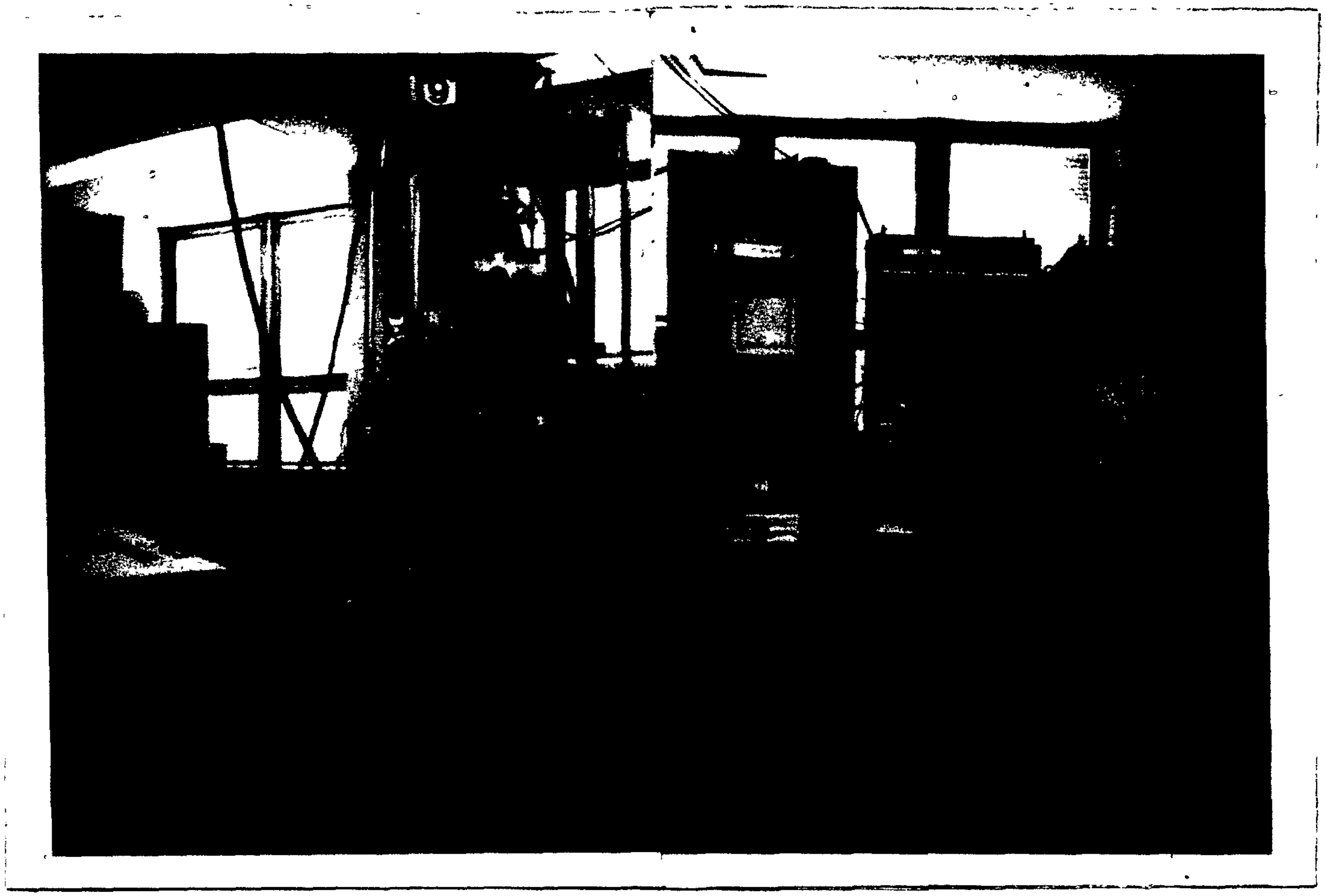

(1) MTS load frame, (2) Centorr furnace, (3) temperature and vacuum control console, (4) actuator, (5) PDP 11/04 computer, (6) Tektronix terminal, (7) hardcopy unit, (8) load cell, (9) LVDT

Figure 27 Exterior view of the automated, servohydraulic, high temperature, high vacuum testing system.

(1) thermocouples, (2) tungsten tooling, (3) tungsten mesh heating elements, (4) tungsten and molybdenum heat shields, (5) vacuum chamber, (6) hinged door

Figure 28 Interior view of the high temperature high vacuum testing chamber.

the testing chamber.

4.3.1.1 Closed-loop servohydraulic system

In this section, the basic operating principles of the testing system will be described, with special attention being given to the control unit. Three main units can be delineated in the system:

1) load unit
2) performance unit
3) control unit.

The load unit consists of a two column load frame rated at 100 KN under static loading. The crosshead, which is raised or lowered by means of hydraulic crosshead lifts, supports the hydraulic actuator which applies the loading force to the specimen. The actuator is provided with an 'open housing' LVDT (linear variable differential transformer) assembly to provide a stroke feedback signal for displacement control or displacement readout (see Fig. 29). The LVDT utilized with this equipment has four calibrated ranges of operation, namely 100, 50, 20 and 10 mm. For the present work, all tests were carried out using the 10 mm range. The forces applied to the specimens are measured by means of bridge resistance load cells placed on the load frame platen. Two load cells of different capacity were employed, a 100 KN load cell for tests at temperatures up to 900 K and a 5 KN load cell for higher temperature tests. Both load cells were calibrated to give output accuracies within 0.5% of range and the LVDT was calibrated to better than 1% of range.

The performance unit consists of a 38 liter per minute hydraulic power supply, a servovalve and a service manifold. The servovalve, which is the final control element in the servohydraulic testing system, reacts to an electrical input signal by porting hydraulic fluid in a direction and at a rate determined by the input signal's polarity and magnitude. The performance unit provides the system with the energy required for the test in the form of controlled, filtered hydraulic fluid under pressure at 21 MPa.

The control unit of the system consists basically of a set of plug-in printed circuit cards, each performing a particular function. A block diagram showing the main components of the control unit is given in Fig. 29, where the controlled variable is the output from the LVDT, i.e. the stroke signal. The transducers, load cells and LVDT's provide electrical output signals proportional to the quantities that they sense. These transducers receive either AC or DC excitation voltages from associated transducer conditioners, which also receive the outputs from the transducers and provide DC output voltages proportional to the mechanical inputs to the transducers. There are two types of transducer conditioners; (i) the AC type, which provides an amplitude regulated 10 KHz, 10 V peak-to-peak excitation voltage for reactive-type transducers (LVDT); and (ii) the DC type conditioners, which provide an excitation voltage and output amplification for resistive bridge transducers such as load cells and strain gauges. In this kind of conditioner, the transducer output is amplified with a gain of 500, 1000, 2500, and 5000, depending upon the range selected. With the AC conditioners, on the other hand, the operating range selector increases the gain of a DC amplifier, built into the conditioner itself, by multiples of 1, 2, 5 and 10. In both conditioners, however, the full scale output is always a ±10 V, in the form of a low impedance signal.

The signals from the transducer conditioners are fed to a "feedback selector" for selection of the output of a particular conditioner for use in controlling the hydraulic actuator. In the present case, the controlled variable was chosen to be the output from the AC conditioner which corresponds to the position of the face of the tungsten tool in contact with the specimen throughout the test. This feedback selector can be made to operate manually or automatically by setting a two-position knob. In the "local" position, feedback selection is carried out manually; while, if the "remote" position is chosen, feedback selection is accomplished by the Data/Control Processor, also shown in

Fig. 29. Another important function of the feedback selector is the optimization of the system speed of response. This optimization is accomplished by adjusting the controller gain.

The DC Error signal, which is the algebraic sum of the feedback signal and the control signal (or command), is the output signal of the servocontroller and it should be zero during static operation of the system; for example, just before the test is actually started, where the compression rod is not applying any load on the sample. At this point the output from the transducer conditioners corresponding to both the load cell and the LVDT should be zero. During dynamic operation, that is, while the test is going on, the difference between the feedback and command signals produces a DC Error which is scaled so that ±10 corresponds to 100% of the range in which the controlled variable is being operated. Thus, when the LVDT is set in the 10 mm range, 10 mm of actuator travel corresponds to −10 V (in the case of compression tests), so that the actuator's characteristic is 1.0 mm V^{-1}. The DC Error signal is the control signal which operates the servovalve on the hydraulic actuator; thus a 10 volt DC Error signal produces a full scale servovalve current and consequently a full servovalve opening allowing oil into the actuator which will drive it to 100% displacement.

The valve driver shown in Fig. 29 serves the function

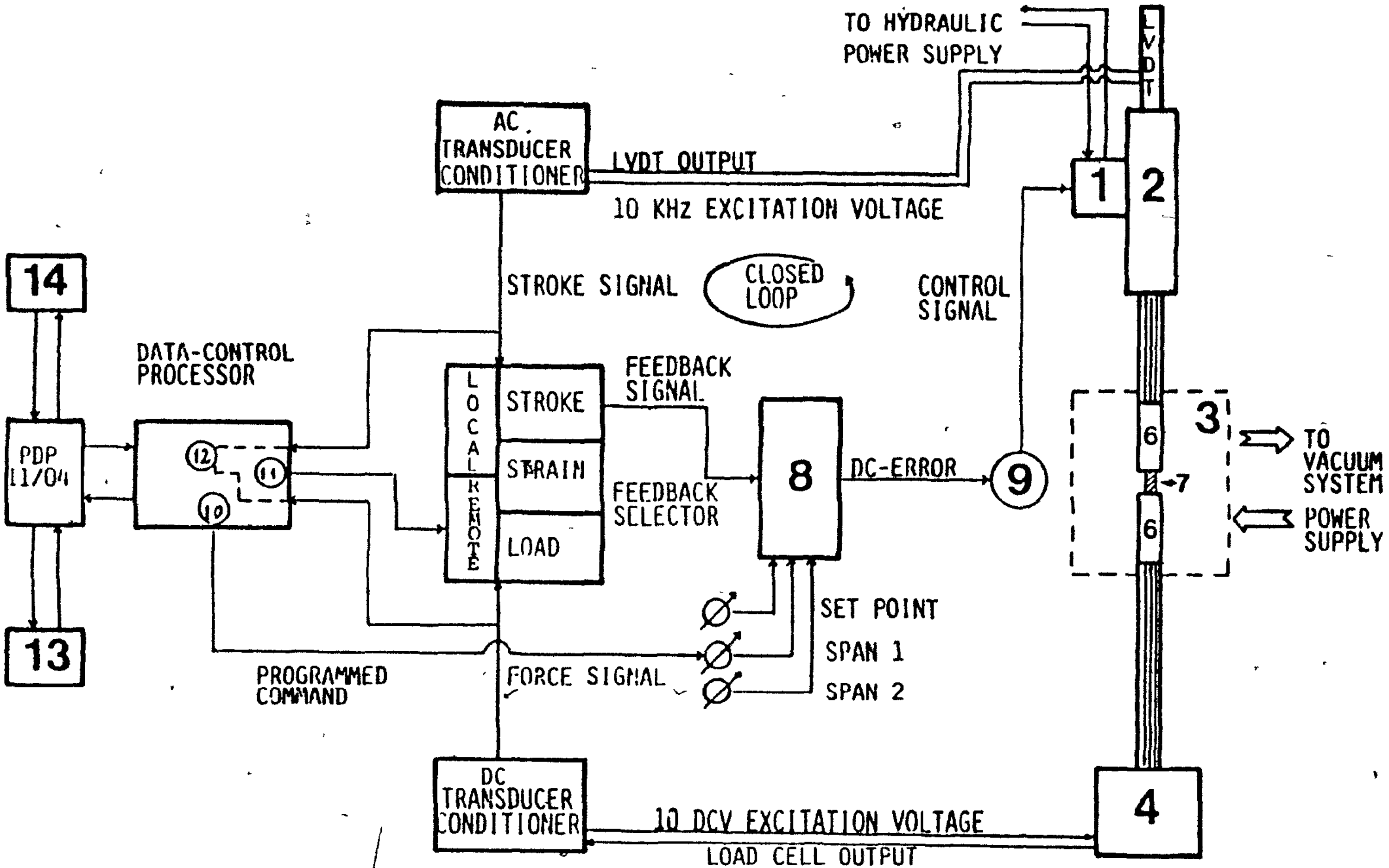

1. SERVOVALVE
2. HYDRAULIC ACTUATOR
3. TEST CHAMBER
4. LOAD CELL
5. STAINLESS STEEL EXTENSION RODS
6. THORIATED TUNGSTEN COMPRESSION RODS
7. SPECIMEN
8. SERVOCONTROLLER
9. VALVE DRIVER
10. HARDWARE SEGMENT GENERATOR
11. FEEDBACK SELECTOR REGISTER
12. ANALOG-DIGITAL CONVERTER
13. FLOPPY DISK DRIVE UNITS
14. TERMINAL

Figure 29. Automated closed-loop servohydraulic mechanical testing system equipped for high vacuum, high temperature compression tests.

of helping to maintain the system resolution by preventing silting of the servovalve due to the small impurity particles contained in the oil. This is achieved by applying a low amplified electrical signal to the coils of the servovalve which causes the spool of the valve to vibrate, avoiding the silting in this way and also eliminating static friction which could act so as to reduce the resolution of the system.

4.3.1.2 Control/data processor interface

The closed-loop servohydraulic testing system described in the previous section is "automated" by means of an MTS-433 Processor Interface which performs the functions of command generation, data acquisition and reduction, and real time decision making. The complete automatization of the system includes a Central Data Processor, a Communications Device, the Processor Interface, and the System Software. Table XIX lists the facilities available in the "Automated Closed-Loop Servohydraulic Testing System" and Fig. 29 shows its configuration schematically.

The Central Data Processor, a DEC-PDP-11/04 minicomputer, has a core memory capacity of 28 K in 16-bit words. Communication between the computer and the processor interface and all the peripheral devices, namely, the Tektronix graphics terminal, the Tektronix hardcopy unit, and the DEC-RX11 floppy disk system, is accomplished by an input/

output bus called PDP-11 Unibus. Figure 30 is a block diagram of the interface, which consists of a set of 5 basic printed circuit cards installed in what is known as the PDP-11 Computer Bus Converter. These five cards have the function of interfacing with the Unibus and of converting Unibus signals to signals usable in the Processor Interface. The specific function of each card is outside of the scope of this description and further information can be obtained from reference 63.

In order for the processor interface to achieve the automatization of the closed-loop servohydraulic testing system, a number of other printed circuit cards must be added to the basic cards. These cards perform the functions of command generation (HARDWARE SEGMENT GENERATOR, Figs. 29 and 30), data acquisition and reduction (ANALOG-TO-DIGITAL CONVERTER, Figs. 29 and 30), feedback selection and control mode switching (FEEDBACK SELECTOR REGISTER, Figs. 29 and 30), as well as real time decision making, which is very important for the type of experiments carried out in the present work.

The hardware segment generator is a computer controlled function generator which provides 1024-point analog haversine (180°) or ramp waveform segments for use as the main command waveform for the system servocontroller (see Fig. 29). Each haversine or ramp waveform segment is created after the computer provides end level and segment duration parameter data. This allows complex waveforms (consisting of any mixture of haversine and ramp segments from 0.0059 through 2048 s duration, 100 Hz maximum frequency, and -10 V through +10 V amplitude) to be generated by defining the control parameters, storing them in an array and starting the Hardware Segment Generator with the aid of BASIC-11 compatible assembly language routines. The Hardware Segment Generator is formed by a set of four cards (see Fig. 30); the Master Segment generator produces a haversine or ramp segment for each time parameter entered and each output segment starts at zero volts, ends at ten volts, and has 1000 steps. The Channel Segment Generator scales the analog segment from the Master Segment Generator according to the specified end-level parameters. The resulting analog output is connected to the Dump circuit which is used to ramp the command signal to zero in the event of an error condition; this causes a switch in control mode from any mode to load control. If no error condition exists, then the command signal passes through the Dump circuit unchanged. The master clock oscillator provides raw timing for the Master Segment Generator.

The Analog-to-Digital Converter can convert up to 4 channels of analog signals to equivalent 12-bit digital words for use by the computer. The inputs of this converter are the analog outputs of the transducer conditioners corresponding to the force and stroke signals (see Fig. 29).

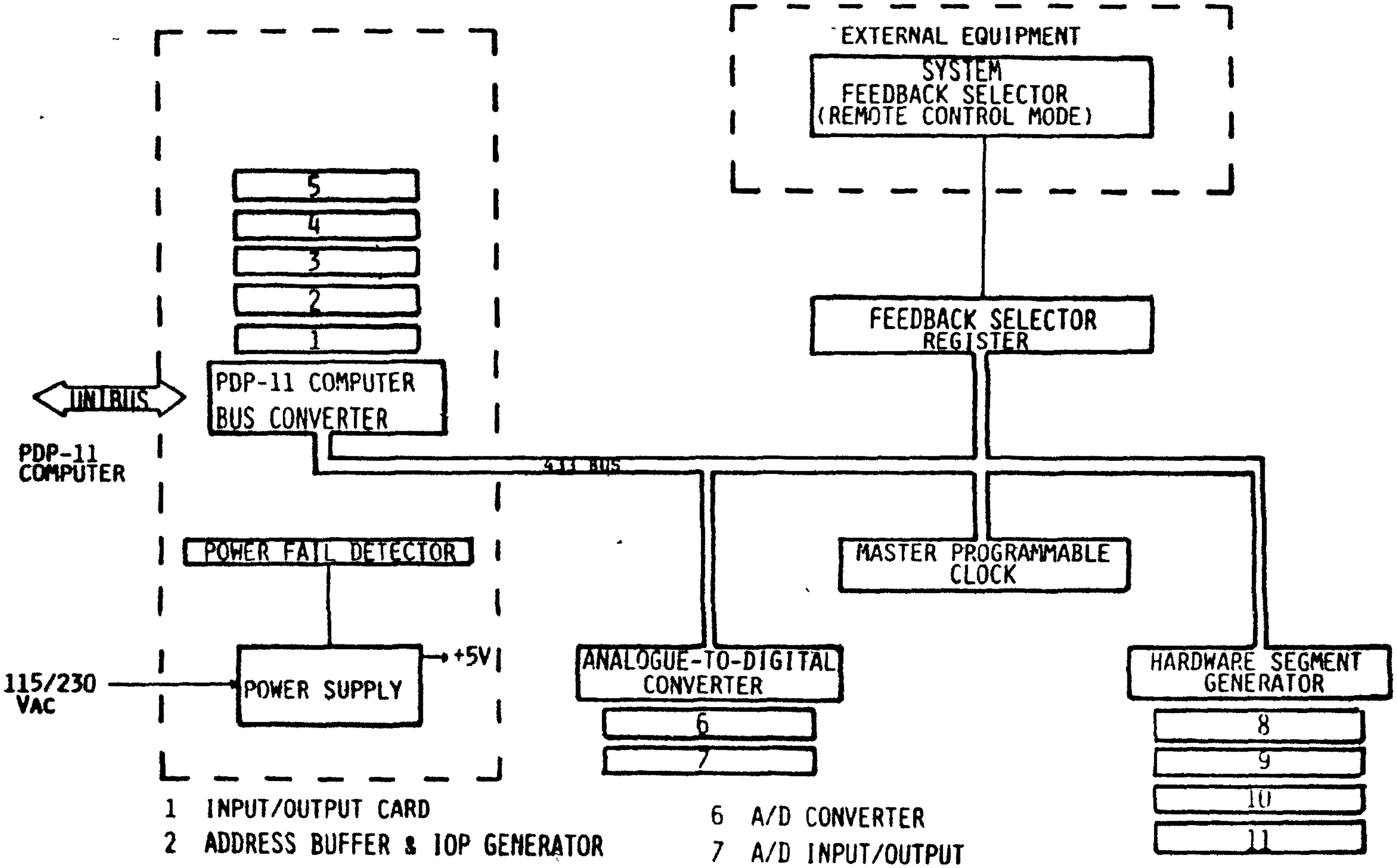

1 INPUT/OUTPUT CARD
2 ADDRESS BUFFER & IOP GENERATOR
3 DATA IN/OUT CARD
4 PRIORITY INTERRUPT REGISTER
5 UNIBUS TERMINATOR

6 A/D CONVERTER
7 A/D INPUT/OUTPUT
8 MASTER SEGMENT GENERATOR
9 CHANNEL SEGMENT GENERATOR
10 MASTER CLOCK OSCILLATOR
11 DUMP CIRCUIT

Figure 30. Processor Interface Block Diagram.

The Master Programmable Clock is programmed by the computer to generate an interrupt after a specified time interval. After this interval, the computer enters a service routine during which certain program steps such as incrementing the servocontroller command, reading the load or stroke signals, or any other function may be performed.

The Feedback Selector Register performs three main functions; the primary function is automatic selection of the transducer feedback signal for the servocontroller. Smooth transfer of control modes during operation is also accomplished using circuits in the system feedback selector (see Fig. 29) combined with appropriate software routines. The second function involves switching in the shunt calibration resistor on the DC transducer conditioners and the third function is to operate external devices such as counters, recorders, alarms, etc., by means of relay control.

4.3.1.3 High temperature, high vacuum testing chamber

In order to carry out high temperature experiments, the automated closed-loop servohydraulic system described above is provided with a high temperature, high vacuum testing chamber which consists of a 17 KVA CENTORR model M60 front loading furnace equipped with a 0.1 m high speed diffusion pump backed by an $8.5*10^{-3}m^3s^{-1}$ mechanical pump. This system provides a static vacuum of 1.3×10^{-3} Pa at 1200 K. While under dynamic conditions the vacuum is always better than 6×10^{-3} Pa. All high temperature tests were carried out when the vacuum was better than 10^{-4} Pa, which was achieved after a short period of holding at the test temperature. A view of the testing chamber is presented in Fig. 28. The hot zone of the chamber, approximately 76 mm in diameter and 200 mm high, is surrounded by concentric multi-layered tungsten and molybdenum radiation shields, with the top and bottom of the furnace chamber similarly shielded. The tungsten heating elements (see Fig. 28) are cylindrically shaped and are vertically placed in each of the four quadrants of the cylindrical hot zone. The heating elements and shields are split into two halves, one half of which is mounted on the hinged door; this arrangement enables direct and easy access to the hot zone for adjustments of the specimen, tooling and thermocouples. The entire furnace is enclosed in a double wall, water cooled stainless steel jacket which assures uniform cooling of the whole assembly. As mentioned before, the top and bottom anvils were machined from thoriated tungsten rods and are ~150 mm high and 32 mm in diameter. They are screwed to the water cooled stainless steel extension rods (see Fig. 29) by means of threaded joints lubricated with graphite to facilitate handling. The compression test specimen is placed coaxially on the lower anvil.

Temperature control in the testing chamber was achieved by means of a Leeds and Northrup (L & N) Current Adjusting Type (CAT) temperature controller working in conjunction with a L & N Speedomax H recorder. The CAT controller provides an output current which is proportional to the deviation in temperature below the set point. The current output of the controller is translated into a power unit appropriate to the furnace by means of an SRC (Silicon Controlled Rectifier) power package. To set a constant heating rate, the set point control is transferred to a Datatrak programmer; thus the set point is moved at a rate determined by an electric curve follower which moves along a line scribed on the Datatrak chart.

To control the temperature in the chamber a J-type Pt/Pt-10% Rh thermocouple was utilized as the sensing element for the temperature controller; for measuring the temperature of the test specimen two K-type Chromel-Alumel thermocouples were used. The position of the thermocouples in the test chamber is shown in Fig. 28. For temperatures below 1200 K, the two K-thermocouples were placed in such a way as to contact the specimen at two diametrically opposite points and the test was usually initiated only when the readings of the two thermocouples were identical, which indicated that no temperature gradients existed across the diameter of the sample. For long term tests, the temperature was kept constant within ±3 K throughout the test. At testing temperatures higher than 1200 K, the occurrence of a reaction between the thermocouple and the Zr specimen did not allow contact and so the thermocouples were placed as close to the specimen as possible to provide temperature control within ±5 K.

4.3.2 Testing technique and procedure

Constant true strain rate compression testing was chosen as the testing technique to carry out the present investigation. This is because it is a fairly simple test, especially as regards strain rate control. It also has the advantage that inhomogeneous flow due to necking does not take place, as it does in the case of tension, so that relatively large strains (of up to 1.0) can be applied. However, inhomogeneous flow can occur if friction between the mating surfaces of the test specimen and the compression tools is not reduced or avoided. The occurrence of friction results in "barrelling" of the specimens; at larger strains, a phenomenon called "fold-over" may also take place. These problems can be avoided by the use of suitable lubricants. For the present case, MoS_2 at room temperature and colloidal graphite at higher temperatures proved very effective in reducing friction during the compression of Excel up to strains of 0.8. In the case of the high temperature tests, graphite also helped to prevent sticking of the Excel specimens to the tungsten tooling.

4.3.2.1 Test specimens

In order to study the directionality of the mechanical properties of the pressure tube, cylindrical specimens were machined from a section of the tube located at 3.8 m from its front end.* As mentioned in Chapter 3, the crystallographic texture developed in the tube becomes stable after the first stages of the fabrication process, specifically during extrusion. Subsequent annealing below the $\alpha/\alpha+\beta$ transformation temperature does not appreciably affect the texture but does eliminate most of the internal stresses resulting from the different orientations of the grains within the material (see Section 3.5). Thus, any anisotropy of mechanical properties exhibited by the pressure tube is a direct result of the texture developed during the fabrication of the tube. This state of anisotropy can be assumed to have three mutually orthogonal planes of symmetry at every point in the tube; these planes intersect each other in three orthogonal directions which are called the principal axes of anisotropy. These are, in the present case, the circumferential, radial, and axial directions of the tube. This assumption becomes apparent when the distribution of (0002) basal planes poles in the tube is analyzed; this can be deduced from the symmetries present in the pole distribution in the tangential plane of the tube. It should be noted that the orientation of the anisotropy axes in a given element of material varies

---

* i.e. from the end of the tube which first comes out of the extrusion chamber.

relative to the element axes during continued deformation, therefore changing the state of anisotropy of the element.

Due to the small wall thickness, the types of specimen which can be machined from the tube are rather limited. The present cylindrical specimens were machined to have their axes parallel to each of the principal directions of anisotropy and they were named Tangential, Radial, and Axial specimens respectively. The specimen orientations in the pressure tube are illustrated in Fig. 31 together with the specimen dimensions. Two main problems were found as a result of the specimen size. One is related to the small size of the specimens, especially the radial specimens, which resulted in much scatter and poor accuracy in the measurement of the small loads (100 N at high temperatures) required to deform specimens with such small cross-sections. Another source of inaccuracy was the small height of the specimens, which required the experiments to be carried out in the lowest range of the LVDT.

As the output of the transducer conditioners is scaled to ±10 V whatever the transducer output, the scatter increases and the accuracy of the measurement decreases as the range of the transducer is decreased. This problem could not be avoided since no other LVDT was available; however, the scatter and inaccuracy of the load readings were improved by using a small load cell fitted with a

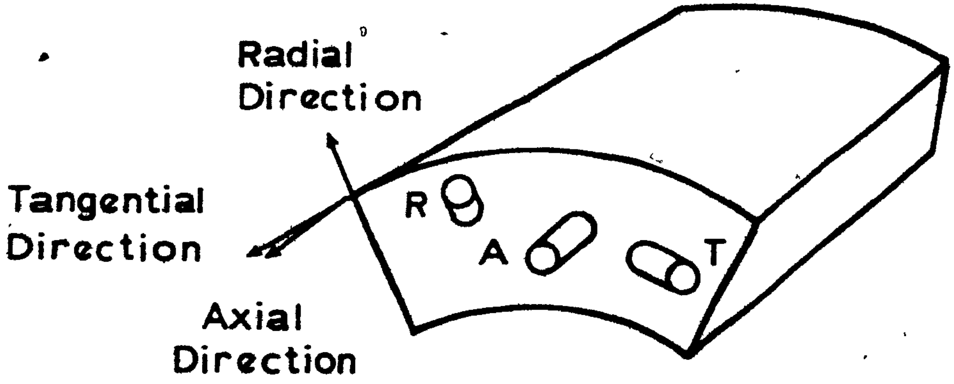

SPECIMEN	DIAMETER (mm)	HEIGHT (mm)
AXIAL	4	6
RADIAL	4	4
TANGENTIAL	4	6

Figure 31. Spatial orientation of the specimens in the Excel alloy pressure tube.

load cell protector and by decreasing the hydraulic pressure to the servovalve.

The anisotropy characteristics of the tube were then studied as a function of specimen orientation in the tube at 10^{-1} and $10^{-4}s^{-1}$ strain rate, over the temperature range 298-1400 K, by means of constant true strain rate compression tests. The complete schedule of experiments is given in Table XX.

4.3.2.2 True strain rate compression tests

In order to carry out constant true strain rate compression tests, the velocity of the upper compression rod must be carefully controlled; the method of doing this will now be described. The true strain on a specimen deformed from an initial height ℓ_o to an instantaneous height ℓ is given by:

$$\varepsilon = \ln(\ell/\ell_o) \qquad (4.1)$$

By differentiating with respect to the time t, the true strain rate is obtained

$$\dot{\varepsilon} = (1/\ell)\cdot(d\ell/dt) \qquad (4.2)$$

where $d\ell/dt$ is the rate of change of specimen height, which in the present case is determined by the position of the interface between the specimen and the compression rod, which is determined in turn by the LVDT connected to the actuator.* Thus, from Eq.(4.2), for a constant true strain rate $\dot{\varepsilon}_c$, the ram velocity must be reduced in proportion to the instantaneous height of the specimen; that is,

$$d\ell/dt = \dot{\varepsilon}_c \cdot \ell \qquad (4.3)$$

In order to produce a constant true strain rate, the movement of the actuator must be controlled so that its velocity remains proportional to the height of the specimen. Thus, the height of the specimen, i.e. the position of the compression rod/specimen interface, must be used as the feedback signal in the closed-loop of the testing system.

As mentioned in Section 4.3, in the system used in this study, MTS-BASIC was the programming language and the RT-11 monitor was used to provide access to system and application programs, as well as to perform input and output functions. This software package contains a number of real time routines written in assembly language which interface the software with the MTS Hardware Processor and the other special devices. These routines can be called from the application programs by means of single instructins, such as FG1 (command function generation), MSW1 (test

---

*We neglect here the elastic compliance of the testing system (see Appendix II) as this affects the strain rate much less than the strain.

mode selection), PLOT, AXES, SCALE, etc. (for plotting), DACQ (data acquisition), etc.

Thus, in order to provide the command signal to be compared with the feedback signal (stroke signal) in the servocontroller (see Fig. 29), a computer program was written so as to provide a DC Error signal that will drive the servovalve and hence the hydraulic actuator in the manner described by Eq.(4.3). This was carried out as follows.

The FG1 routine was used to create analog output via the Hardware Segment Generator described in Section 4.3.1.2. The format of this function in the application program is

FG1 (ARG1, ARG2, ARG3, ARG4)

where ARG1 is the name of an array which contains the command information, i.e. the end levels of the segments corresponding to the specific values of the voltages in the channel being controlled. ARG2 is the number of times that the command information will be used (for cyclic applications). ARG3 is employed to select the output mode for the array, which for the present case was chosen to be of the ramp type with unrepeated segments of constant duration. ARG4 selects the maximum frequency of the Hardware Segment Generator. This device is designed to operate in 8 frequency ranges, 0, 1, 2, 3, 4, 5, 6, 7, corresponding to 100, 50, 20, 10, 10, 5, 2 and 1 Hz respectively. Each frequency range corresponds in turn to 2047 machine units. Now, the total time of an experiment is given by the ratio of the total true strain and the true strain rate at which the specimen must be deformed, i.e.

$$t = \varepsilon/\dot{\varepsilon} \tag{4.4}$$

Thus, as the output of the HSG was chosen to consist of segments of constant duration, it is possible to divide the total time of the experiment into a number of segments, N, each of duration

$$\Delta t = \frac{t}{N} \quad \text{(sec/segment)} \tag{4.5}$$

and a frequency

$$f = \frac{N}{t} \quad \text{(Hz)} \tag{4.6}$$

If R is the frequency range in which the HSG is chosen to operate, then

$$f = \frac{2047}{R} \; \frac{N}{t} \quad \text{(machine units)} \tag{4.7}$$

and from Eq. (4.5)

$$\Delta t = \frac{R}{2047} \; \frac{t}{N} \quad \text{(machine units)} \tag{4.8}$$

which is the period of time, in machine units, that elapses between the end levels of each segment; it is constant throughout the experiment. Usually N and R are chosen to give a value for f near 2047, which corresponds to a frequency near the maximum in the frequency range chosen. The value of f is always contained in the first element of the array containing the command information.

The command information, i.e. the elements of the array X(I), must be calculated to produce a control signal capable of moving the actuator at a decreasing velocity which is proportional to the height of the specimen. The 10 volt analog signal corresponding to the maximum operating range of the LVDT corresponds to 2047 machine units (4.885 mV/machine unit); therefore, if the LVDT operating range is R1, then the calibration factor for this transducer is:

$$K = \frac{2047}{R1} \tag{4.9}$$

A similar expression can be obtained for the load transducer.

Assuming that the initial height of the specimen L0 corresponds to S1 machine units and that the instantaneous height L corresponds to X(I) machine units, then the instantaneous change in height due to the generation of a segment by the HSG will be

$$\Delta L = L - L0 = \frac{S1 - X(I)}{K} \tag{4.10}$$

Now, the incremental plastic strain $\Delta\varepsilon$, produced when the compression rod compresses the sample as a result of the response of the actuator to a command corresponding to X(I) volts, is related to the total plastic strain ε by the following expression:

$$\Delta\varepsilon = \varepsilon \cdot I/N \tag{4.11}$$

where I is the i'th segment generated and N is the total number of segments. Now, it must be recalled that the increment in true strain is related to the increment in engineering strain Δe by

$$\Delta\varepsilon = \ell n(1 + \Delta e) \tag{4.12}$$

where $\Delta e = \Delta L/L0$. Thus, rearranging Eq.(4.12),

$$\Delta L = L0\ \mathrm{EXP}(\Delta\varepsilon) - L0 \tag{4.13}$$

and equating (4.13) and (4.10),

$$\frac{S1 - X(I)}{K} = L0 * \mathrm{EXP}(\Delta\varepsilon) - L0 \tag{4.14}$$

Finally, substituting Eq.(4.11) into Eq.(4.14) and solving for X(I),

$$X(I) = S1 + K * L0[\mathrm{EXP}(-\varepsilon \cdot \frac{I}{N}) - 1] \tag{4.15}$$

where the minus sign has been introduced to take into account the compressive nature of the deformation.

Equation (4.15) gives the size of each segment generated by the HSG and, as can be seen, the step size decreases exponentially, thus producing the exponentially decreasing rate of displacement required to maintain the true strain rate constant throughout the experiment. The accuracy with which the strain rate was controlled is shown

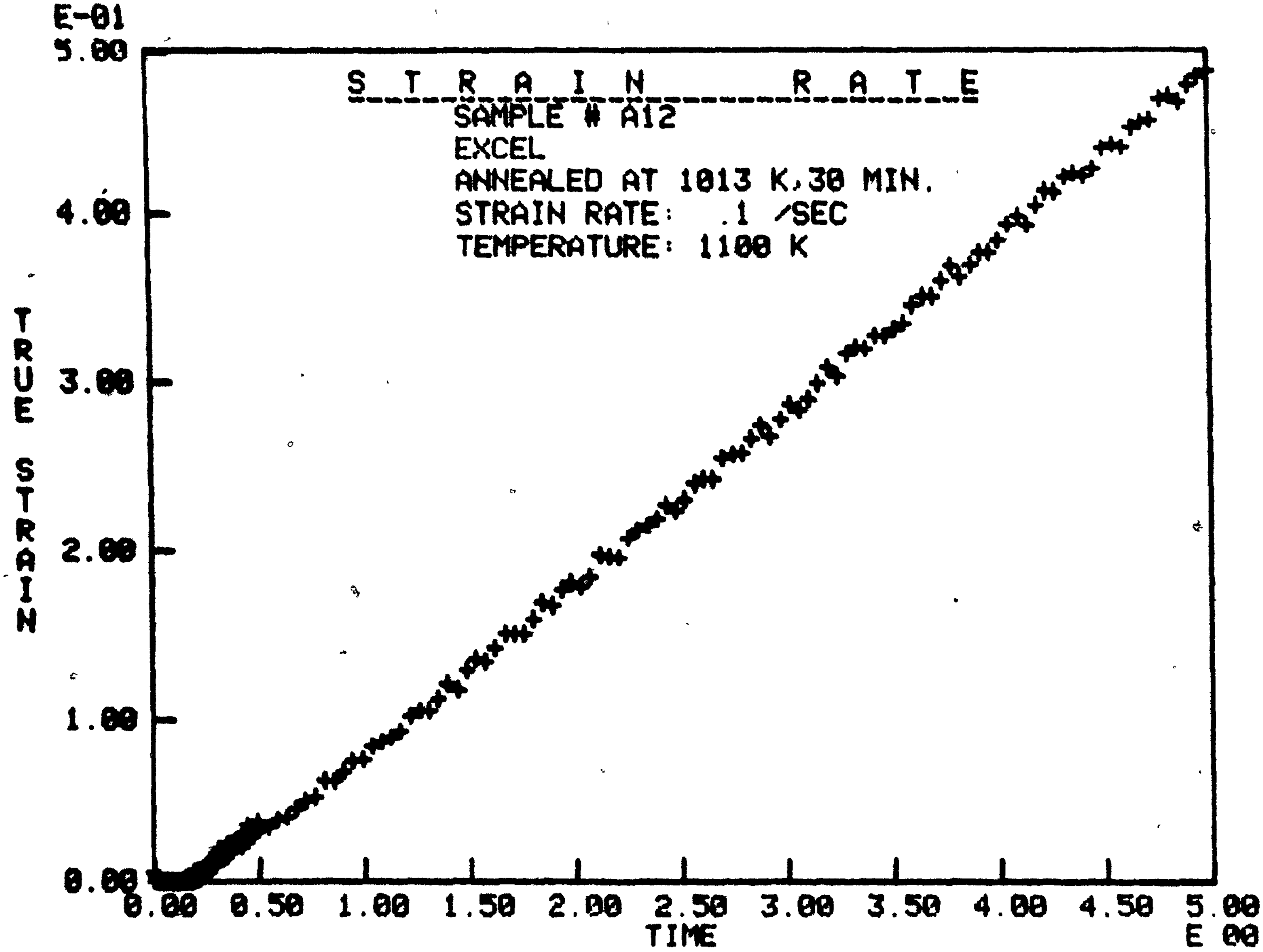

Figure 32. Computer plot of true strain vs. time showing the constancy of the true strain rate during an experiment.

in Fig. 32, where a computer plot of the true strain vs. time shows a constant slope of 0.1 for a specimen deformed to $\varepsilon = 0.5$ at $\dot{\varepsilon} = 0.1$. The total number of segments N and the frequency at which the HSG is operated (f) are chosen according to the strain rate, i.e. the time of duration of the test (see program listing in Appendix I). Data Acquisition was performed at two different rates: 100 points were taken during the initial 1/10th of the total strain; and a further 100 points were read during the balance of the straining. The data were saved in an MTS BASIC file on a floppy disk and were also displayed in graphical form on the Tektronix terminal, following which copies were made by means of the hardcopy unit. Appendix I gives the source listing of the program used to carry out the experiments involved in the study.

4.3.2.3 Test procedure

Both faces of the specimen were lubricated, either with MoS_2 for room temperature testing or with colloidal graphite for the high temperature experiments. A light layer of lubricant was also applied to each anvil and the specimen was placed at the centre of the bottom anvil. The thermocouples were positioned in place (see Fig. 28) and the upper anvil was then lowered to a position near the upper surface of the specimen; this helped to reduce the temperature differences between the ends of the sample during heating. The test chamber was then closed and evacuated (except in the case of room temperature testing). The test specimen was heated to the test temperature in about one hour and a soaking period of 15 min. was allowed to stabilize the temperature and to allow programming procedures to be carried out. The specimens were compressed to a total strain of 0.6 or to fracture and then the ram was retracted to its original position and the furnace power was shut off to permit the chamber to cool, an operation which usually took about 1.5 hours.

4.4 Metallography

Selected specimens were sectioned along their compression axes in a low speed Buehler/Isomet saw. The specimens were cold mounted using a polyester resin (Castolite) and left to cure overnight. Rough grinding of the specimens was done on 120 grit silicon carbide paper on a rotating wheel with the purpose of removing any resin from the surface of the specimens. Fine grinding was performed manually on silicon carbide papers in the order 240, 320, 400 and 600 grit size, using a small amount of water as lubricant.

Mechanical polishing was carried out on a silk cloth on a rotary polishing wheel run at low speed. The polishing medium was 6 μm diamond paste and kerosene. The final polishing stage was carried out using an attack-polishing technique(76) employing a 1/2% HF (48%) solution and Cr_2O_3 freshly prepared by igniting ammonium dichromate. This procedure produced a scratch-free surface which, when examined under the microscope, showed very little attack of the grain structure of the specimens. In this condition, the specimens were slightly etched in a solution of 40 ml lactic acid, 40 ml HNO_3 (50%) and 4 ml HF (48%); and subsequently anodized in a solution of 10 g oxalic acid in distilled water using a voltage of 80 Vdc. The specimens were examined using polarized light in a Neophot microscope.

Table XIX. Computer/Interface Subsystem

	HARDWARE
Central Data Processor	DEC-PDP-11/04 Computer
Communications Device	Tektronix Graphics Terminal
Storage and Output Devices	DEC-RX11 Floppy Disk System RX01 Floppy Disk Drive Tektronix Hardcopy Device
Interface	MTS-433 Processor Interface
SOFTWARE	MTS-BASIC/RT-11

Table XX. Experimental Schedule

Test temperature, K.	Strain Rate, s^{-1}.	
-	10^{-1}	10^{-4}
295	AT	ATR
600	-	AT
800	AT	AT
900	AT	AT
1000	ATR	ATR
1100	AT	
1200	AT	

A = Axial, T = Tangential, R = Radial

CHAPTER 5

EXPERIMENTAL RESULTS

5.1 Crystallographic Texture of the Excel Alloy Pressure Tube

Figures 33 and 34 show the pole figures for the front and back ends of the pressure tube utilized in this investigation. As can be seen, the tube showed a very strong texture, as indicated by the high texture coefficients, and consisting of basal plane poles oriented towards the circumferential direction of the tube. Additionally, the basal plane poles seem to be randomly oriented near the radial direction, whereas no basal poles are aligned along the axial direction of the tube. This texture is a direct result of the tube fabrication process, as mentioned in Sec. 4.3.2.1, and it is apparent that the state of anisotropy of the tube, which is a result of the texture, has three mutually perpendicular planes of symmetry which intersect along the three principal directions of the tube, i.e. the axial, radial and circumferential directions.

In terms of the ideal orientations introduced in Chapter 3 (see Fig. 22), this tube has a texture with most of the grains in A orientations (TC = 14) and some of the

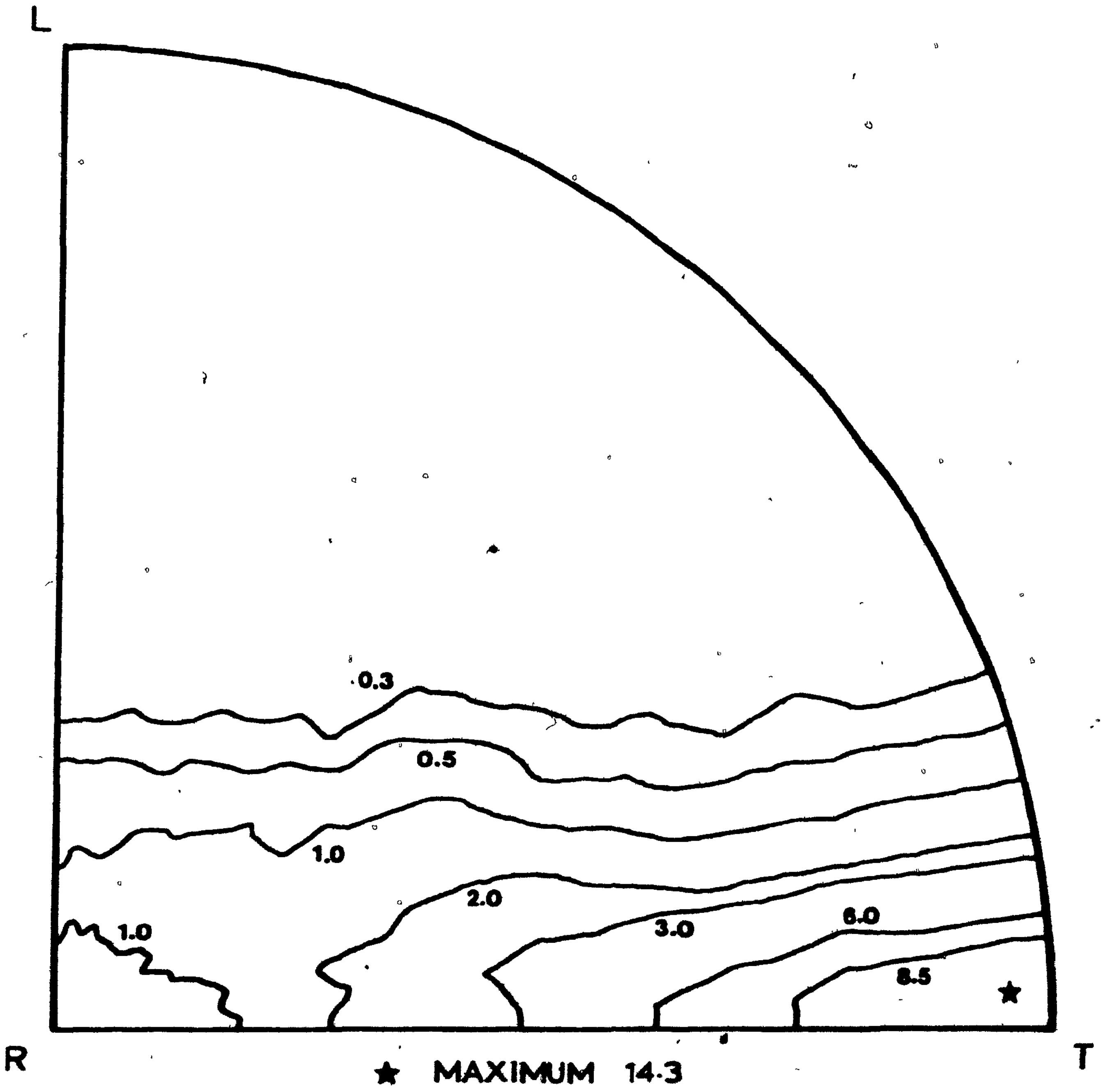

Figure 33. Average pole figure for the Excel alloy pressure tube utilized in this work (Front end of the tube).

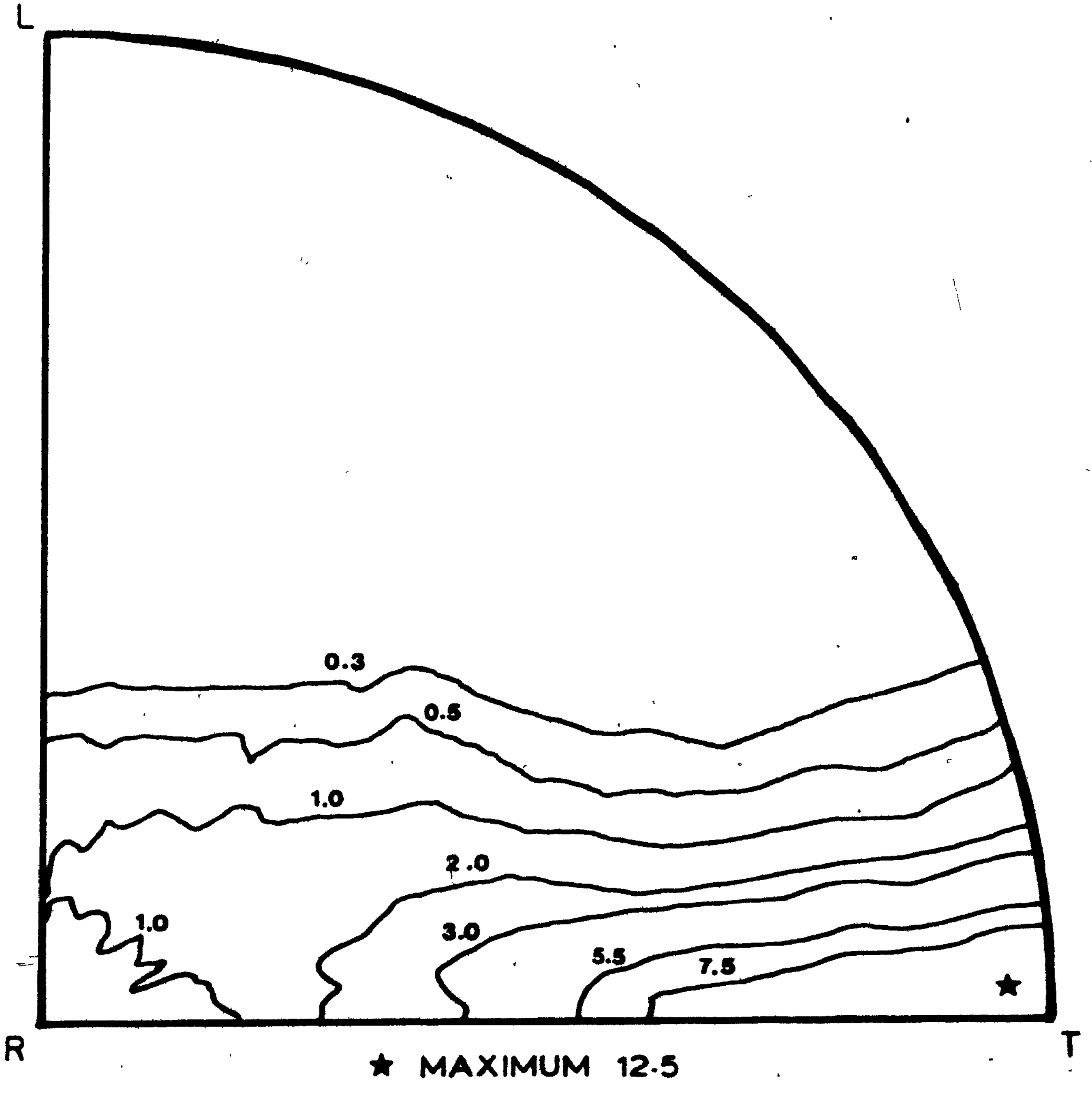

Figure 34. Average pole figure for the Excel alloy pressure tube utilized in this work (Back end of the tube).

grains in AB orientations. It is of particular interest to compare these results with those given in Table X for Zircaloy-2 and Zr-2.5 wt% Nb pressure tubes in similar metallurgical conditions. It is evident that Excel alloy pressure tubes should have a higher circumferential yield strength than the other tubes since they develop a much stronger texture with the basal plane poles more completely oriented along this direction.

Another important observation can be made by comparing the pole figures for other Excel alloy pressure tubes reported by Cheadle et al$^{(67)}$ (see Fig. 26), with the pole figure for the tube used in this work. It seems that the basal plane normals in the present tube are more evenly distributed in the radial direction of the tube. This implies a slight increase in the yield strength without affecting the ductility of the tube along the radial direction. This important difference is a direct result of the different alloy composition, as well as the fabrication route for the present tube. With regard to the latter, the effect of increasing the extrusion temperature from 1030 K to 1130 K is to sharpen the texture with more basal poles oriented parallel to the tangential direction; the effect of decreasing the extrusion ratio, by contrast, is to increase the number of basal poles close to the radial direction, leading to an almost random texture in this direction (see Figs. 33 and 34).

Thus, to summarize, it can be said that the crystallographic texture of the pressure tube studied in this work consists of basal planes parallel to the axial direction of the tube with basal poles oriented mainly in the circumferential direction and a <10$\bar{1}$0> direction parallel to the axis of the tube. From the values of the Tc's, one might expect strong anisotropy in mechanical properties, with the pressure tube being stronger in the circumferential direction and weaker along the axial direction.

In terms of this texture for the pressure tube, it is possible to describe the orientation of c poles in the three kinds of specimens used in this investigation: (i) specimens with axes parallel to the circumferential direction of the tube will have c poles oriented approximately parallel to the stress axis of the compression test; (ii) axial specimens will have their axes perpendicular to the c axis of the hexagonal cell; and finally, (iii) in the radial specimens, there is no particular concentration of basal poles along the compression direction. As a result, radial specimens, in which the hexagonal prisms are oriented so that the diametral strains are likely to be similar along the two symmetry directions perpendicular to the stress axis, are expected to exhibit little anisotropy, while circumferential and axial specimens, because of their texture, are expected to display strains in the two symmetry directions perpendicular to the stress axis of different magnitudes; thus the cross-sections of these types of specimens will become elliptical after deformation. Figure 35 shows the ideal orientation of a hexagonal unit cell in the circumferential and axial specimens together with the elements of the most common deformation systems in zirconium alloys. From this figure, it is evident that, during a compression test on specimens with a circumferential orientation, either or both $\{11\bar{2}2\}\langle 11\bar{2}3\rangle$ twinning and/or $\{10\bar{1}1\}\langle 11\bar{2}3\rangle$ pyramidal slip need to be activated in order to allow for the required reduction in height, while tensile strains perpendicular to the stress axis can be accomplished by $\{10\bar{1}0\}\langle 12\bar{1}0\rangle$ prismatic slip. In the case of the axial specimens, however, prismatic slip can account for compressive strains parallel to the stress axis, while tensile strains in directions perpendicular to the stress axis must be accommodated by either pyramidal slip or $\{10\bar{1}2\}\langle 10\bar{1}1\rangle$ tensile twinning. Thus, one might expect differences between the flow behaviour of these two kinds of specimens since the deformation mechanisms by which the strains can be accomplished during the test are different. It is noteworthy that if a tensile stress is applied to the axial specimens, then compressive strains must be accommodated in directions perpendicular to the tensile axis, which according to Fig. 35 involves $\langle \vec{c} + \vec{a}\rangle$ pyramidal slip and/or $\{11\bar{2}2\}\langle 11\bar{2}3\rangle$ compression twinning.

It should be noted that $\{0002\}\langle 11\bar{2}0\rangle$ basal slip could occur in both the circumferentially and axially oriented samples, since the basal poles can have orientations within 40 degrees of the stress axis in the case of the circumferential specimens and around an axis perpendicular to the compression axis in the case of the axially oriented specimens (see Fig. 35). However, the CRSS for basal slip is very high at low temperatures (T < 850 K, see Fig. 6) and twinning should operate under these conditions. As the temperature is increased, basal slip can play a more important role in the deformation process.

In Chapters 2 and 3, the way in which the strain rate, temperature, and chemical composition can influence the deformation mechanisms operating under a given set of conditions was discussed. From the considerations introduced, it is evident that the flow properties of specimens taken from different directions in the pressure tube can have different mechanical properties, and that these diverging behaviours are related to the differential deformation mechanisms which take place at the temperatures and strain rates involved.

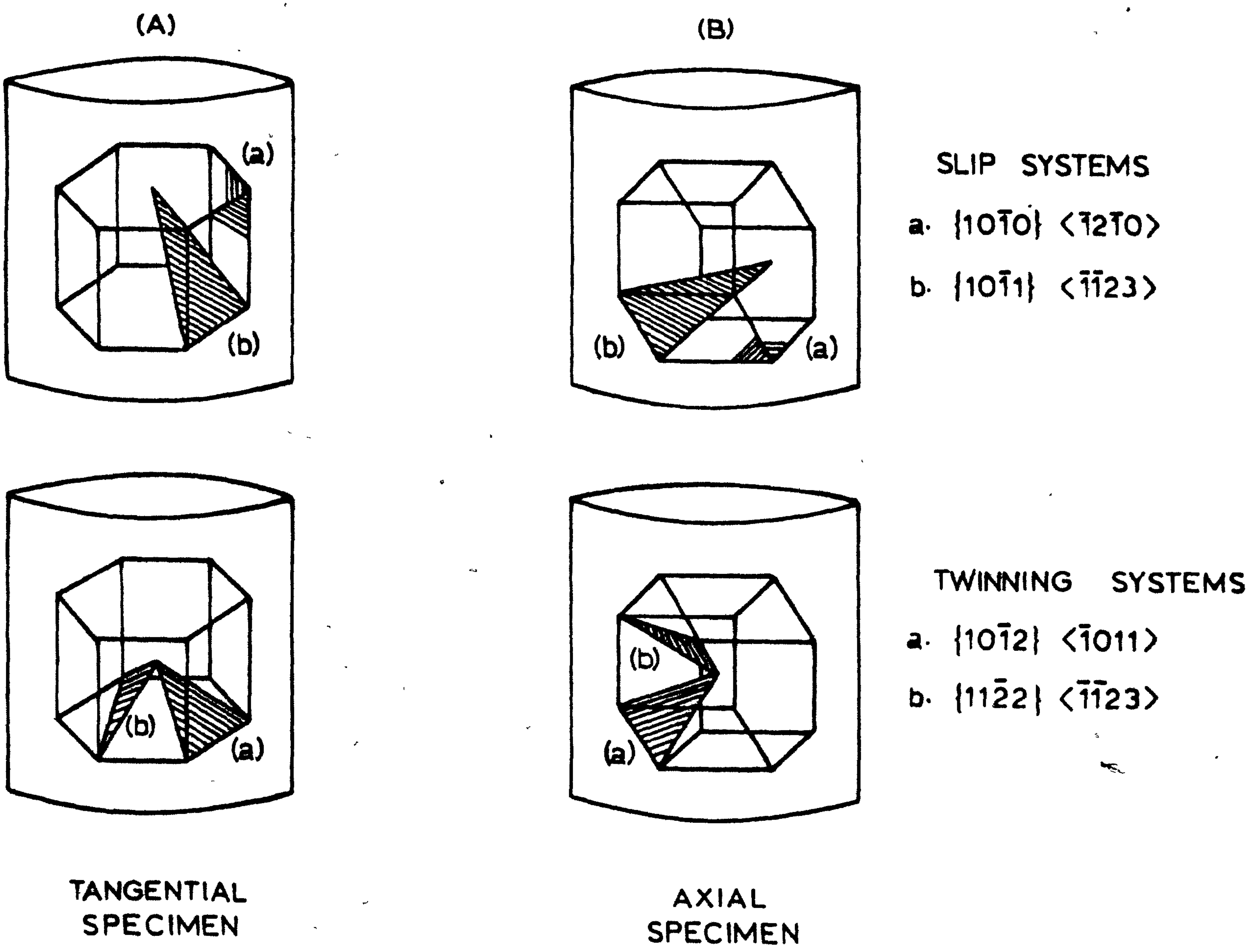

Figure 35. Spatial orientation of the HCP unit cell of alpha zirconium in the specimens utilized in this work.

5.2 Compression Tests

5.2.1 Flow curves

Figure 36 is an equilibrium phase diagram for the Zr-Sn system. It can be seen that for the Excel alloy utilized in this work (3.8 wt% Sn), testing at temperatures below 1000 K involves deforming the HCP alpha zirconium phase, while testing at temperatures in the range 1000-1300 K involves deforming a two-phase structure (α-HCP + β-BCC). Thus, it can be expected that the presence of the β-phase during testing at $T > 1000$ K changes the flow behaviour of Excel alloy, which can also be affected by the presence of precipitates and intermetallic particles (Zr_4Sn).

5.2.1.1 Circumferential direction

The flow curves for circumferentially oriented specimens tested at 10^{-4} and $10^{-1}s^{-1}$ are presented in Figs. 37 and 38 respectively. It can be seen that at or below 600 K at $10^{-4}s^{-1}$, or 900 K at $10^{-1}s^{-1}$, the flow curves show a high and decreasing strain hardening rate until fracture occurs at true strains of about 0.13. This is essentially attributable to the lack of five easily activatable deformation systems. At 800 K and $10^{-4}s^{-1}$, however, fracture of the specimen occurs at $\varepsilon = 0.25$; in contrast to the flow curves at 298 and 600 K at $10^{-4}s^{-1}$ and at or below 900 K at $10^{-1}s^{-1}$, the strain hardening rate is not very large and tends to saturation at about $\varepsilon = 0.2$, just

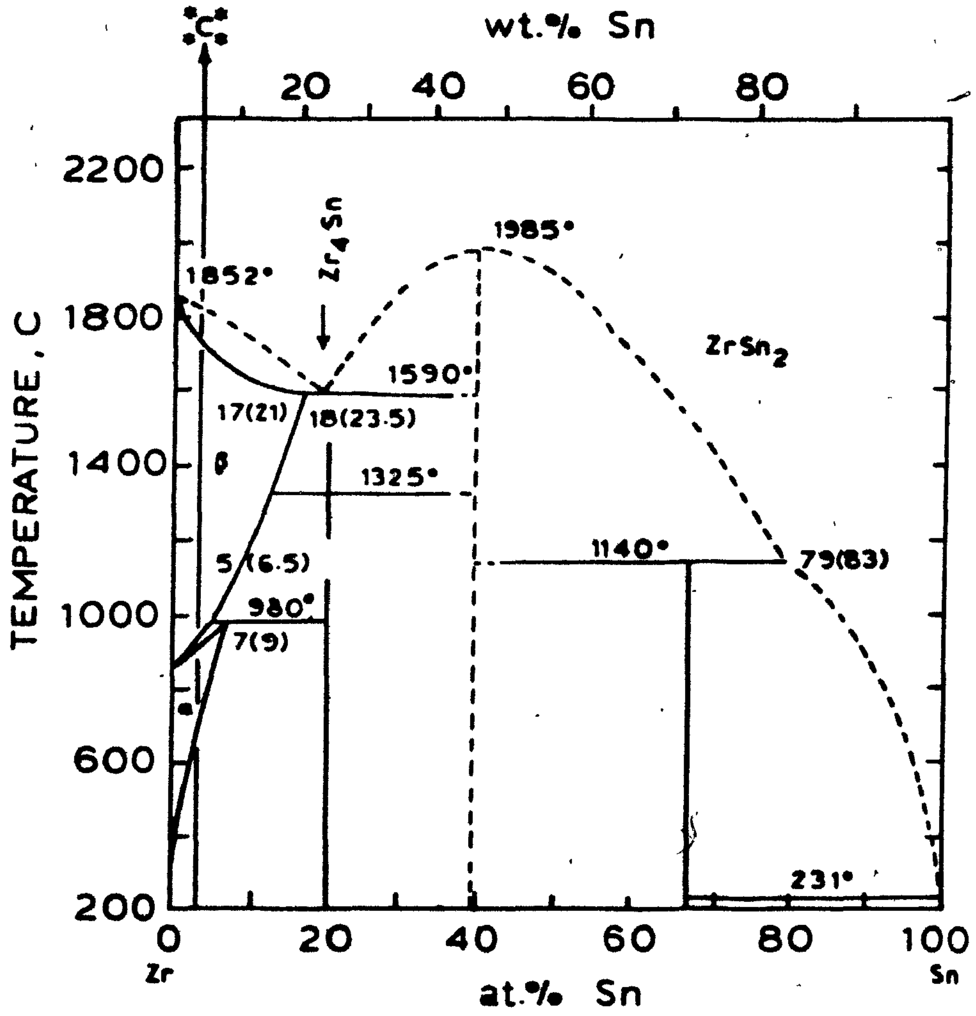

Figure 36. The Zr-Sn equilibrium phase diagram. 'c' indicates the Sn content of Excel alloy.

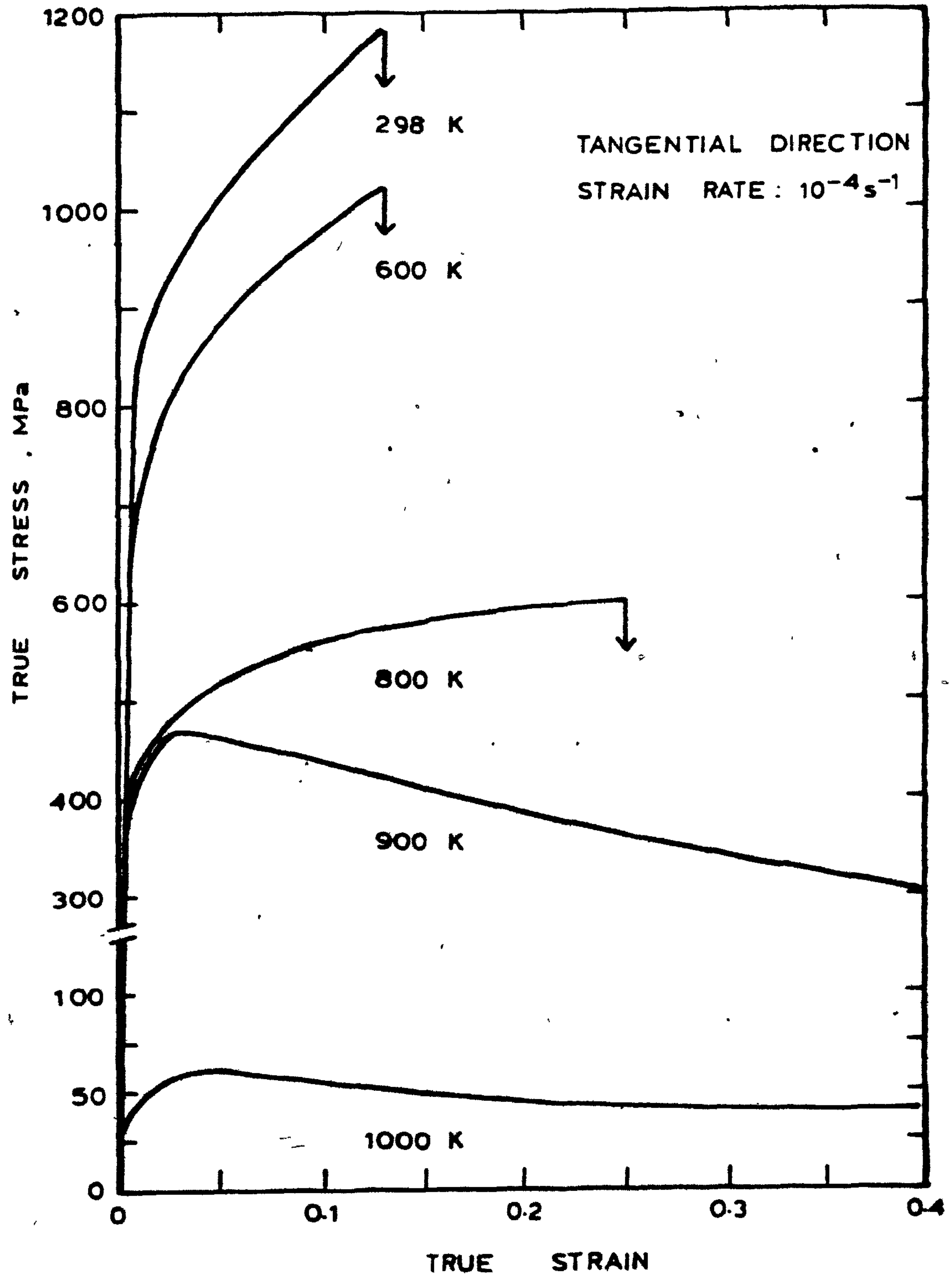

Figure 37. Flow curves for tangential specimens of Excel alloy pressure tube tested in compression.

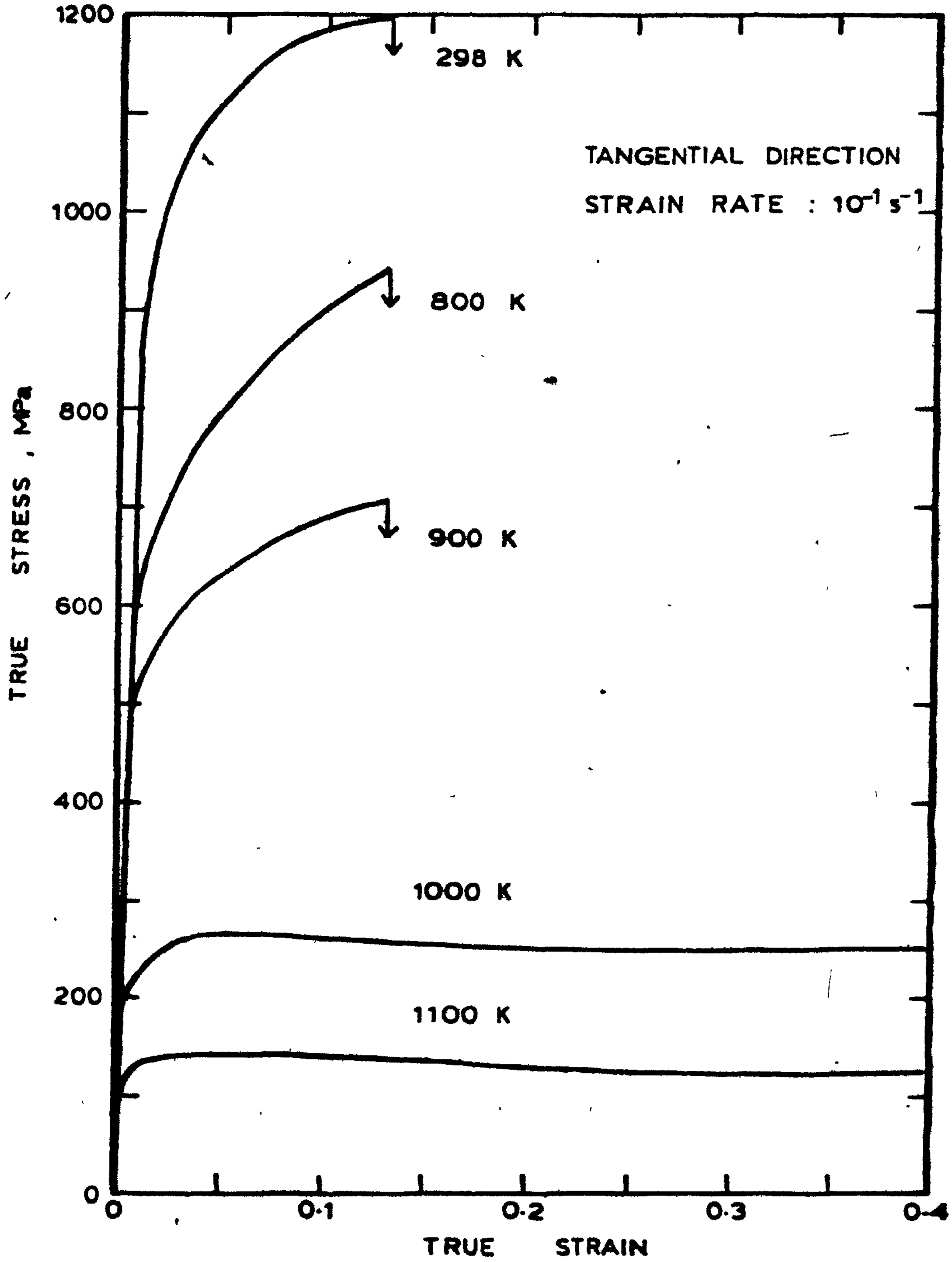

Figure 38. Flow curves for tangential specimens of Excel alloy pressure tube tested in compression.

before fracture occurs. At 900 K and $10^{-4}s^{-1}$, however, it is observed that after about 3% deformation, flow softening occurs very rapidly and it persists to true strains larger than 0.3. At 1000 K and $10^{-4}s^{-1}$, the flow curve shows some of the characteristics of dynamic recrystallization: after an initial flow regime characterized by a decreasing strain hardening rate, a "peak" stress is reached at about 4% deformation followed by flow softening and steady state flow at strains larger than 0.3. Such softening could also be due to shearing and shear localization, which was always present at lower temperatures and eventually led to fracture. The apparent decrease in softening from 900 to 1000 K may be due to the deformation being more homogeneous at the higher temperatures. Another possibility for explaining this softening could be the occurrence of texture softening. Somewhat similar behaviour is observed in the flow curves tested at $10^{-1}s^{-1}$ and 1000 and 1100 K, although the flow softening is much less pronounced and the curves resemble those characteristic of materials undergoing plastic flow controlled by dynamic recovery.

5.2.1.2 Radial direction

The flow curves for radial specimens tested at 298 and 1000 K and at strain rates of 10^{-4} and $10^{-1}s^{-1}$ are presented in Fig. 39. It can be seen that the room tempe-

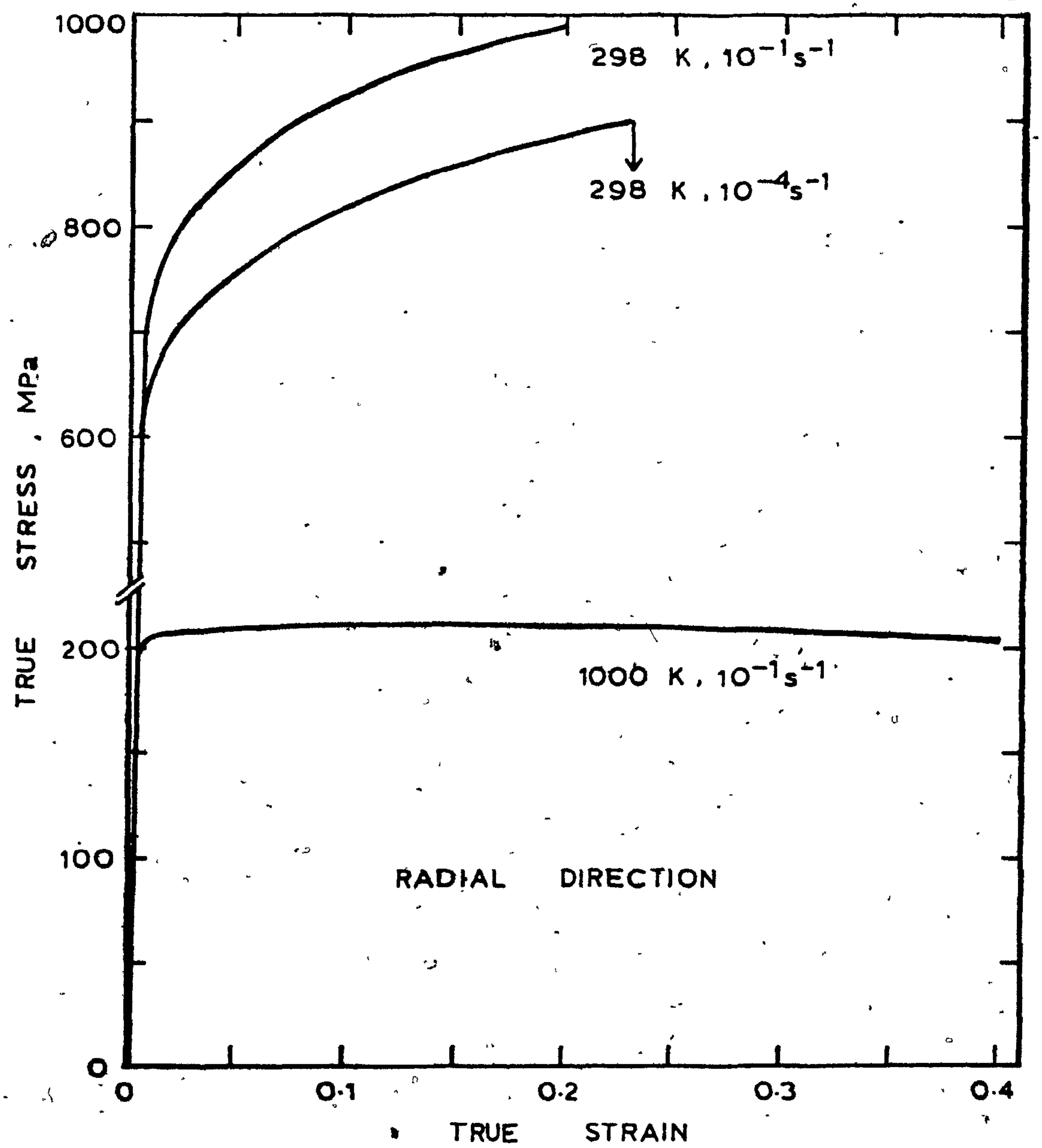

Figure 39. Flow curves for radial specimens of Excel alloy pressure tube determined in compression.

rature flow behaviour is very similar to that of the circumferential specimens, i.e. a large and decreasing strain hardening rate is observed until fracture occurs, although at a somewhat larger strain. It should be noted that with this kind of specimen, the initial height was only 4 mm, so that the scatter in the raw data was very large and sometimes pre-strains of the order of 10% were applied to the specimens at the moment of advancing the actuator to contact the surface of the specimen. Nevertheless, it can be observed from Fig. 38 that $\theta = d\sigma/de$ is smaller than in the case of the tangential specimens; this indicates that at least 5 independent deformation systems are more easily obtained and the fracture strains are consequently larger. At 1000 K and $10^{-1}s^{-1}$, a flow curve showing the characteristics of a flow regime controlled by dynamic recovery is again obtained.

5.2.1.3 Axial direction

The flow behaviour of the axial specimens turned out to be entirely different from that of the circumferential and radial ones.

The flow curves are reproduced in Figs. 40 and 41 for strain rates of 10^{-4} and $10^{-1}s^{-1}$ respectively. As can be seen, at $10^{-4}s^{-1}$, the flow curves for 600 and 298 K at first show a relatively large and decreasing rate of work hardening which seems to reach a minimum at about 4% defor-

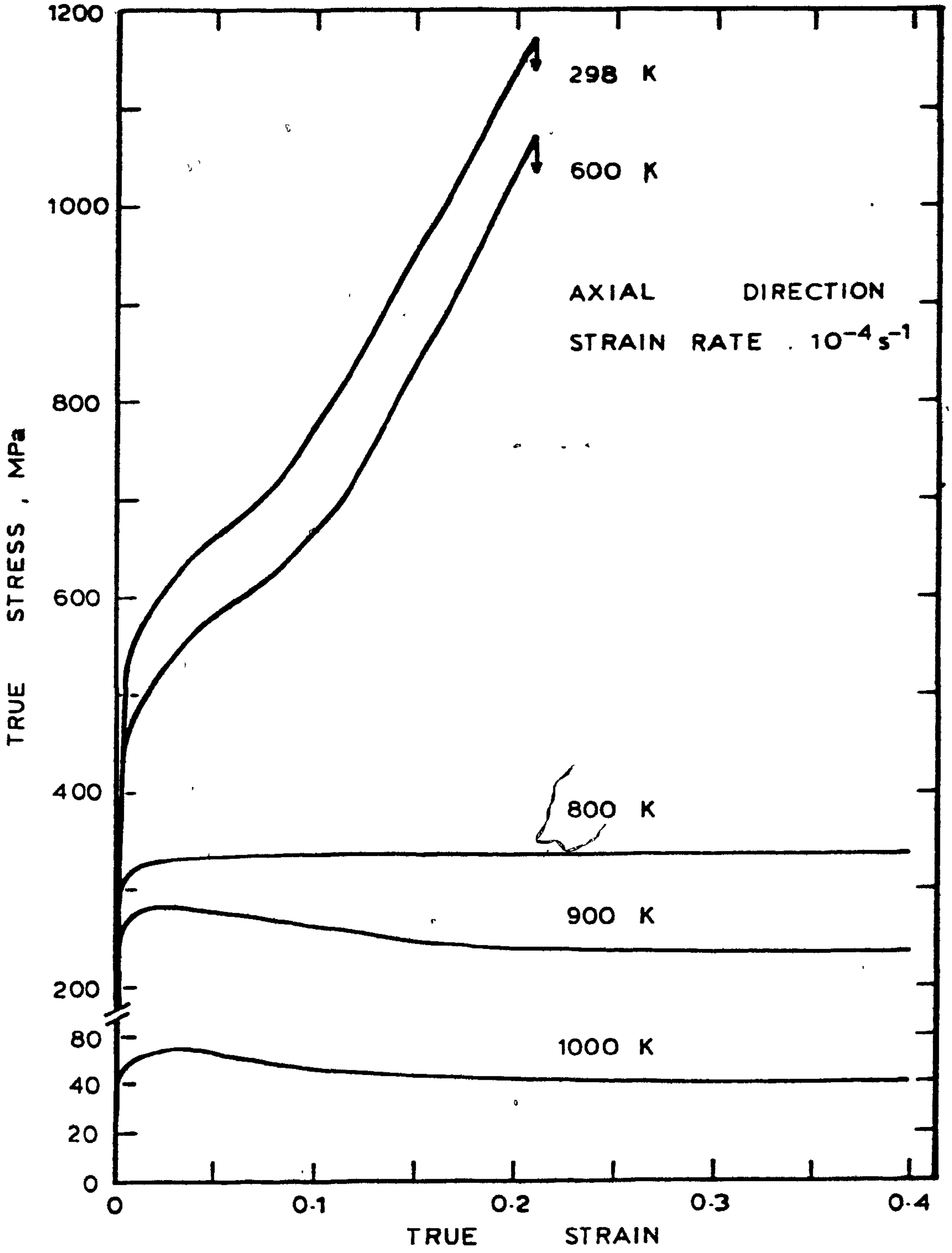

Figure 40. Flow curves for axial specimens of Excel alloy pressure tube tested in compression.

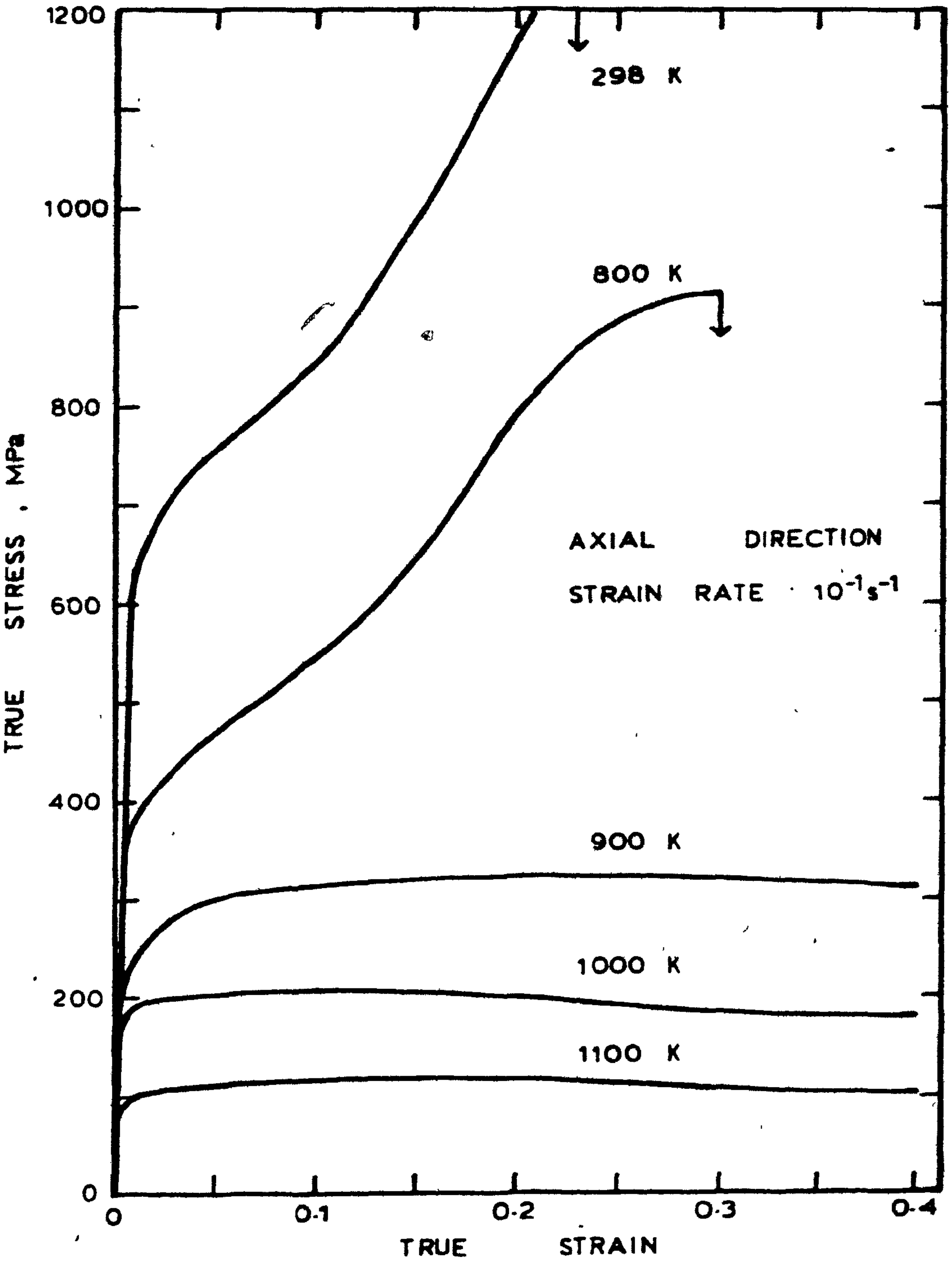

Figure 41. Flow curves for axial specimens of Excel alloy pressure tube tested in compression.

mation; after this strain, Θ increases with stress or strain until it reaches a constant value after approximately 10% deformation. This strain hardening rate remains at its steady value until fracture occurs at about 23% deformation. Similar behaviour is observed at a strain rate of $10^{-1}s^{-1}$ and up to 800 K. However, at 800 K and $10^{-1}s^{-1}$, after the regime of constant strain hardening rate, the slope of the flow curves starts to decrease again at strains larger than 0.2 and a small further strain causes the specimen to fracture in the same manner as the other specimens in which no decrease in Θ was observed.

The shape of these flow curves resembles those for zirconium single crystals obtained by Akhtar and Teghtsoonian(18) in tensile tests of crystals oriented for prismatic slip. A possible explanation for this behaviour was thought to be the activation of different deformation mechanisms in each of the stages of flow. It was therefore decided to investigate the effect of stress state on the flow characteristics of the axial specimens. This was done by carrying out a tensile test on a specimen machined from the axial direction of the pressure tube. Due to experimental limitations, this was only completed at room temperature and the test was performed by Dr. N. Christodoulou of AECL in an automated MTS-Alpha testing system. The flow curve for this test is given in Fig. 42 and it can

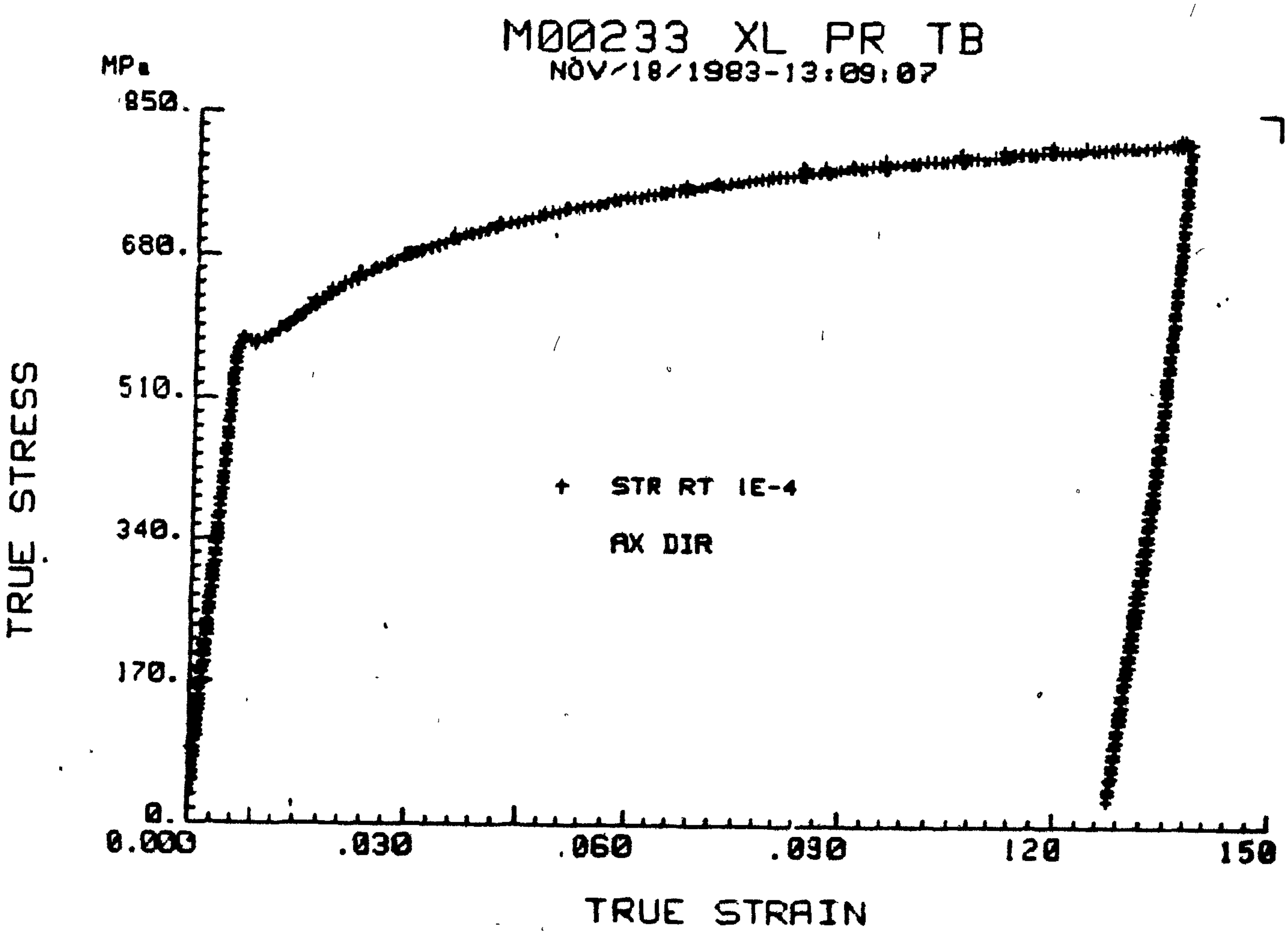

Figure 42. Tensile flow curve for an axial specimen of Excel alloy pressure tube determined at 298 K and $10^{-4}s^{-1}$. (Courtesy of Dr. N. Christodoulou, AECL, Chalk River.)

be seen that, comparing this curve with those given in Figs. 40 and 41, the state of stress, i.e. uniaxial compression vs. uniaxial tension, does indeed affect the flow behaviour of the axial specimens. Firstly, the tension testing of axial specimens causes a yield drop which is not observed during compression tests. Secondly, the yield strength in tension, as determined by the back-extrapolation method, seems to be slightly lower than the yield strength in compression, as determined by measuring the proportional limit (0.2% offset strain) after fitting a straight line to the compression data for strains up to 0.005. Thirdly, the strain hardening rate during the tension test, after the initial yield drop, <u>decreases</u> with strain and seems to saturate at strains larger than 15%. A comparison of the two flow curves shows the dramatic effects that the stress state causes in the deformation behaviour of these specimens; the two flow curves have been replotted in Fig. 43 for comparison purposes. Although the scatter in the compression data for the first 2% deformation is large, a fourth interesting point is the Strength Differential (SD) exhibited by this alloy. The flow stresses for continued deformation after about 0.11 true strain become <u>larger</u> for compression than for tension. This could be due to the reorientation of the basal plane poles caused by the formation of $\{10\bar{1}2\}$ twins during the compression tests. This twin causes a rotation

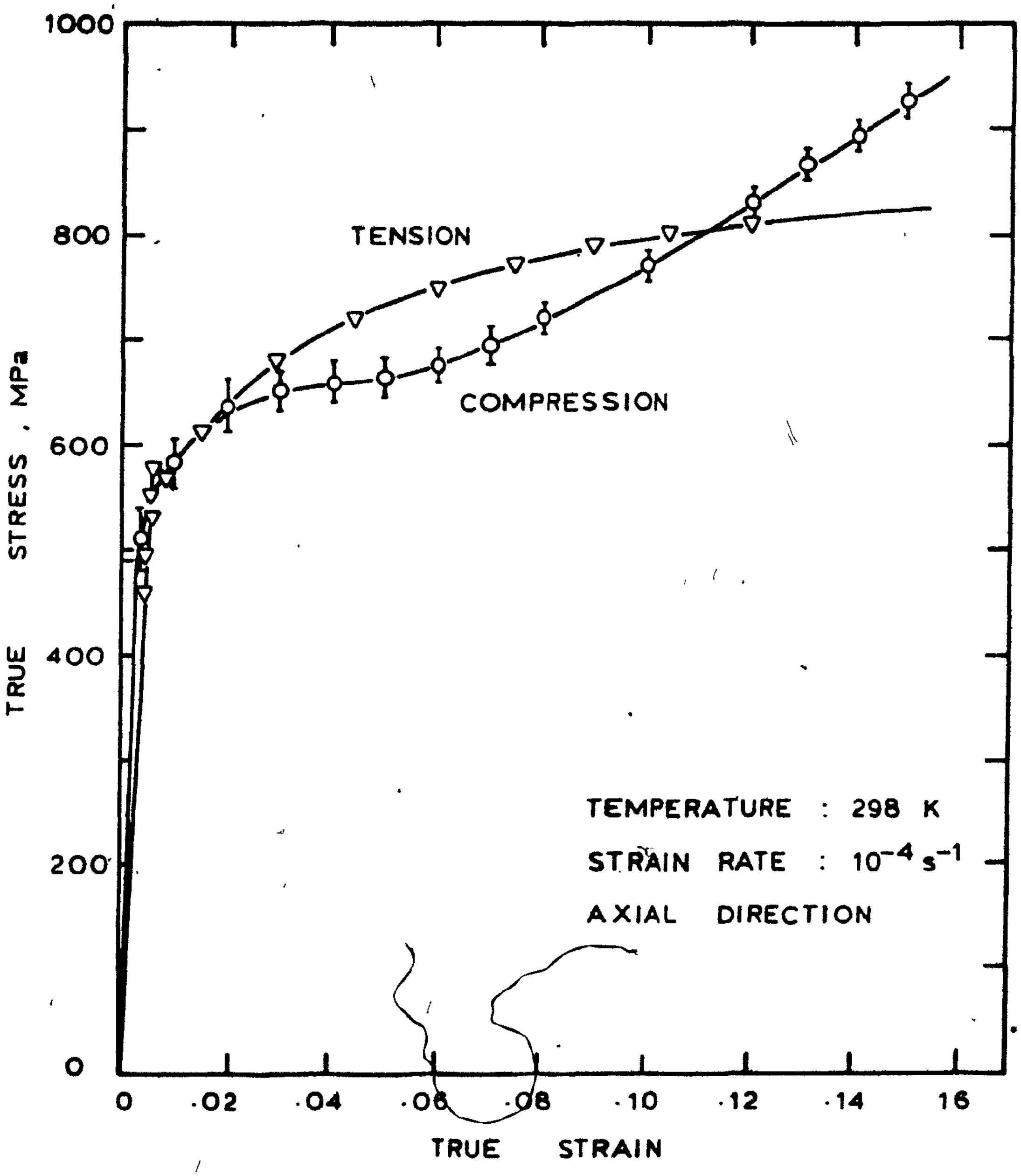

Figure 43. Effect of stress state on the flow behaviour of axial specimens of Excel alloy pressure tube.

of the texture so as to align the c poles with the stress axis; should this occur, a reduction in height along the c axis can only be achieved by either pyramidal slip with a $<\vec{c} + \vec{a}>$ Burgers vector or by $\{11\bar{2}2\}$ twinning. Either of these mechanisms has a much higher CRSS than that required for prismatic slip on $\{10\bar{1}0\}$ planes, which is the mechanism operating during the tensile test. This topic will be addressed further in the discussion chapter of this work.

At $10^{-4}s^{-1}$ and 800 K the flow behaviour seems to be controlled by dynamic recovery as the stress-strain curve shows a steady state regime of flow after the initial strain hardening regime. Similar behaviour is observed at $10^{-1}s^{-1}$ from 900 to 1100 K. On the other hand, dynamic recrystallization (or some other flow softening process such as texture softening) seems to control the flow behaviour of specimens deformed at $10^{-4}s^{-1}$ in the temperature range 900 - 1000 K. A steady state flow regime is reached at $\epsilon > 0.2$.

5.2.2 Flow behaviour within the $(\alpha+\beta)$ phase field

Figure 44 shows the flow curves for the specimens tested at 1200 K and $10^{-1}s^{-1}$. Although the scatter in these two experiments was large (±5 MPa for strains greater than 0.1), two points are noteworthy. First, the yield

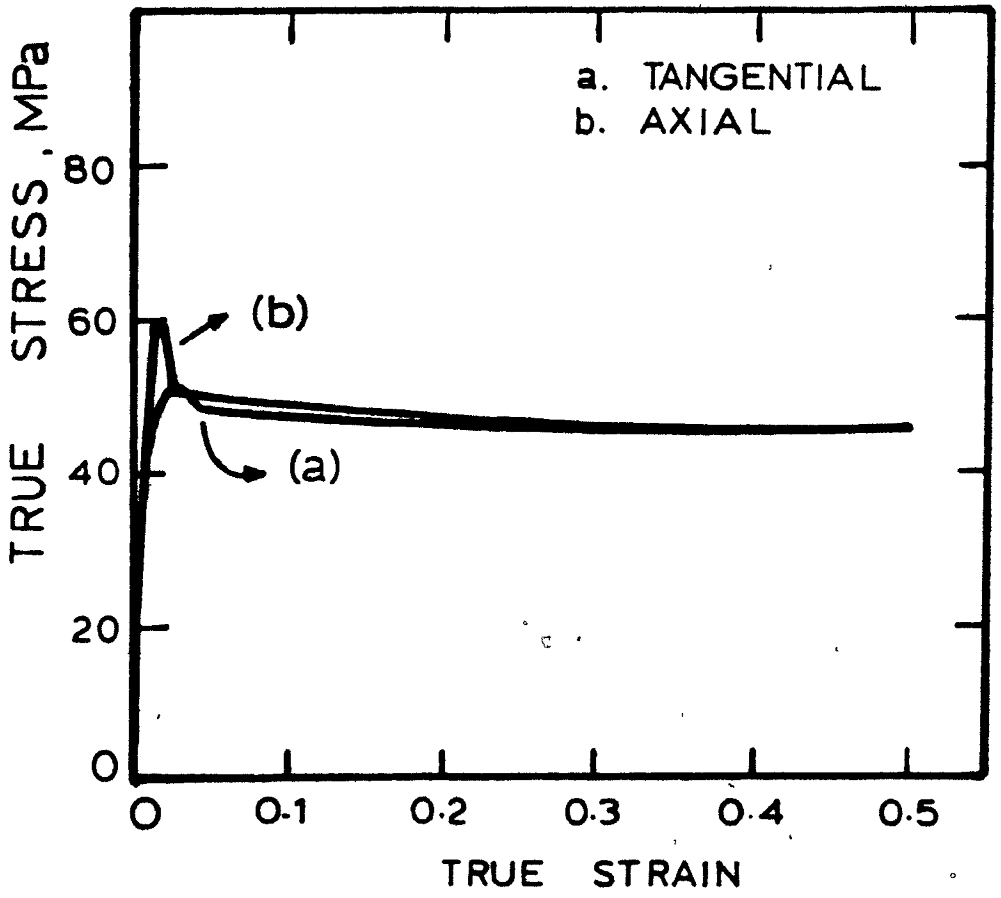

Figure 44. Yield point phenomenon in specimens of Excel alloy pressure tube tested at 1200 K and $10^{-1}s^{-1}$.

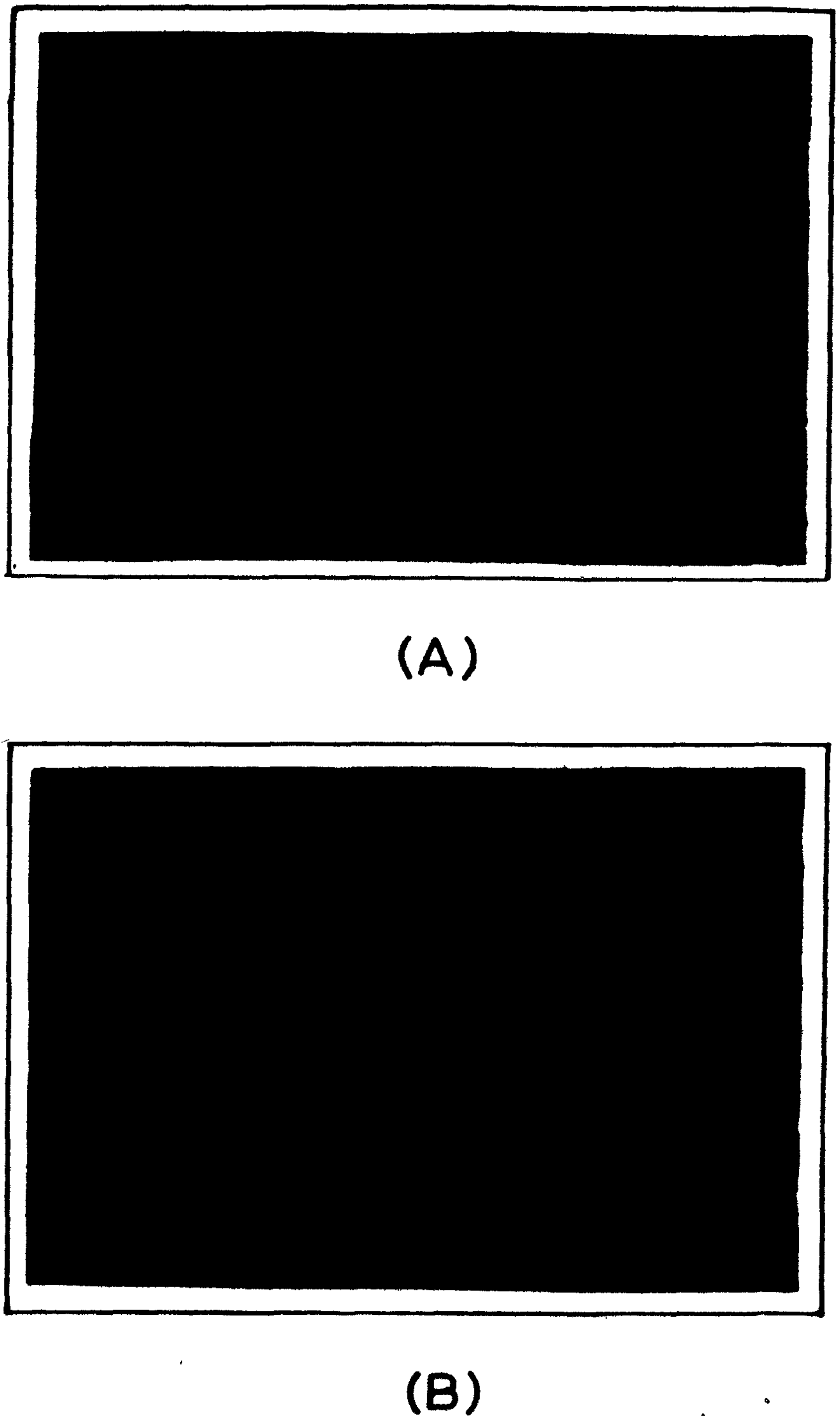

FIGURE 45 OPTICAL MICROGRAPHS OF EXCEL ALLOY DEFORMED AT 1200 K AND 10^{-1} s^{-1}. x1000 .

(A) BRIGHT FIELD

(B) POLARIZED LIGHT

(ROOM TEMPERATURE MICROSTRUCTURE).

point in the axial specimen is sharper and the yield drop is larger than in the case of the tangential specimen. The relative yield drop in the first case is 20% and in the second case it is 11%. After the initial yield, both flow curves show slight softening, and at strains larger than 30% a regime of steady state flow is established. Figure 45 is a photograph of the longitudinal section of a circumferential specimen tested at 1200 K and $10^{-1}s^{-1}$. It can be appreciated that a considerable amount of precipitation has occurred, mainly at grain boundaries. This, together with the occurrence of the sharp yield points, is evidence that aging can occur under these conditions of testing. The presence of the β-phase should be noted at the testing temperature. On slow cooling from a temperature within the (α+β) phase field, any β-phase present transforms to produce very small α grains, together with some retained β-phase, possibly α' martensite (see Fig. 45(a), within the elongated grains). It can also be seen from Fig. 45(b) that the microstructure at the temperature of testing consisted of approximately 50% α and 50% β-phase.

5.2.3 Effect of temperature and strain rate on the flow stress

The flow data determined from the experimental flow curves (Figs. 37–41) are listed in Table XXI. Here, it should be mentioned that, for a strain rate of $10^{-4}s^{-1}$ and temperatures higher than 800 K, the scatter in the flow curves is large due to the small loads required to deform the specimens, as mentioned in Chapter 4. As a consequence, the values for the 0.2% offset yield stress have an estimated error of 20%. This error decreases with decreasing temperature and increasing strain rate as the loads required to deform the specimens are higher. Figures 46 to 51 give the temperature dependence of the flow stress (0.2% and 2% offset yield stress and flow stress at $\varepsilon = 0.1$) at the two different strain rates used in this work for all the three directions tested. As can be seen, the flow stress decreases with increasing temperature and increases with strain rate irrespective of specimen orientation. The rate of decrease of flow stress is initially slow: (i) between room temperature and 600 K at $10^{-4}s^{-1}$; and (ii) between 298 and 800 K at $10^{-1}s^{-1}$. Above these temperatures, the flow stress decreases rapidly with an increase in temperature and it seems that the rate of decrease does not depend on strain rate, as can be observed from the similar slopes of the different curves.

Table XXI. Flow data for compression tests of annealed Excel alloy

Specimen	Temperature (K)	Strain Rate (s^{-1})	$\sigma_{0.2\%\ \mathrm{offset}}$ (MPa)	$\sigma_{2\%\ \mathrm{offset}}$ (MPa)	$\sigma_{\varepsilon = 0.1}$ (MPa)
T 2(1)	298	10^{-4}	690	930	1160
T 9	600	10^{-4}	600	820	1000
T A 3	800	10^{-4}	368	480	582
T 6	900	10^{-4}	271	354	430
T 1 8	1000	10^{-4}	30	42	48
A 2(2)	298	10^{-4}	515	640	768
A 8	600	10^{-4}	448	544	660
A X 2	800	10^{-4}	276	324	340
A X	900	10^{-4}	220	275	220
A 1 6	1000	10^{-4}	45	59	55
R 1(3)	298	10^{-4}	600	740	840
R 7	1000	10^{-4}	22	35	35
T A 2	298	10^{-1}	900	1110	1200
T 7	800	10^{-1}	600	750	900
T 5	900	10^{-1}	475	600	690
T 1 4	1000	10^{-1}	208	248	260
T 1 2	1100	10^{-1}	105	128	740
T 1 3	1200	10^{-1}	50*	45**	45

... cont'd

Table XXI--cont'd

Specimen	Temperature (K)	Strain Rate (s^{-1})	$\sigma_{0.2\%\ offset}$ (MPa)	$\sigma_{2\%\ offset}$ (MPa)	$\sigma_{\varepsilon = 0.1}$ (MPa)
AX3	298	10^{-1}	600	740	840
A7	800	10^{-1}	372	432	530
AX1	900	10^{-1}	220	280	320
A24	1000	10^{-1}	180	210	210
A12	1100	10^{-1}	96	108	115
A13	1200	10^{-1}	60*	50**	48
R10	298	10^{-1}	672	840	920
R5	1000	10^{-1}	190	210	210

(1) Tangential direction specimen

(2) Axial direction specimen

(3) Radial direction specimen

* Upper yield point

** Lower yield point

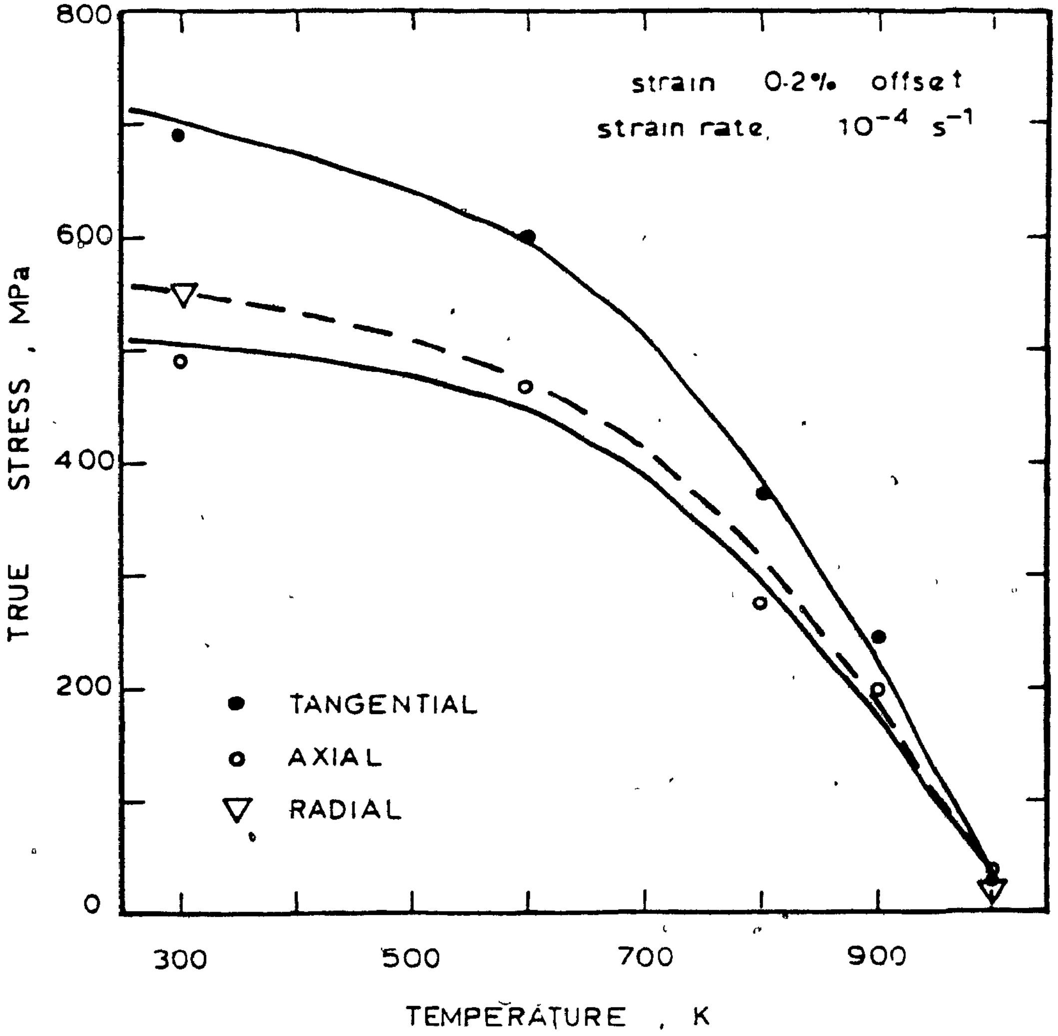

Figure 46. Effect of temperature and specimen orientation on the 0.2% yield stress of specimens machined from Excel alloy pressure tube, $10^{-4}s^{-1}$.

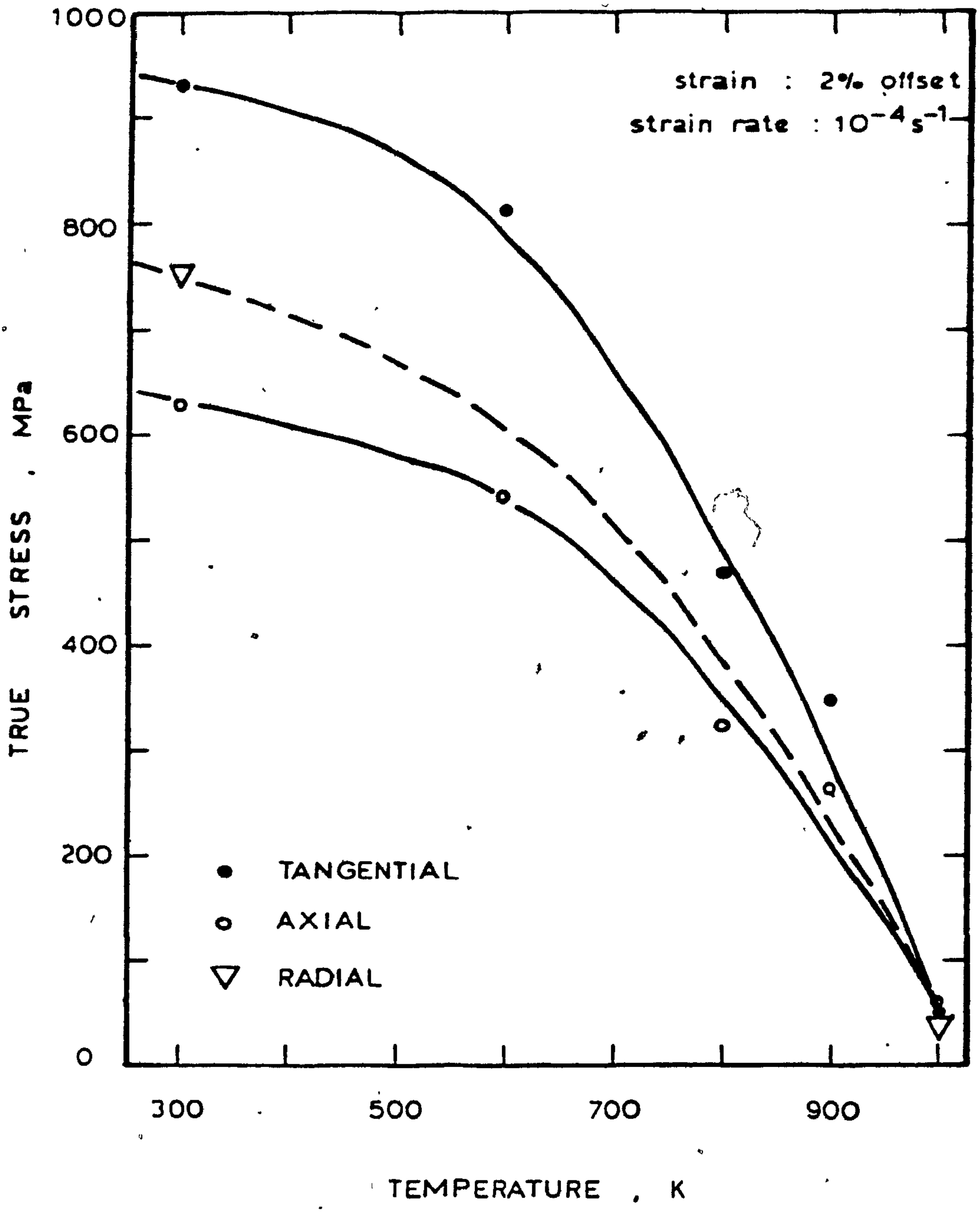

Figure 47. Effect of temperature and specimen orientation on the 2% yield stress of specimens machined from Excel alloy pressure tube, $10^{-4}s^{-1}$.

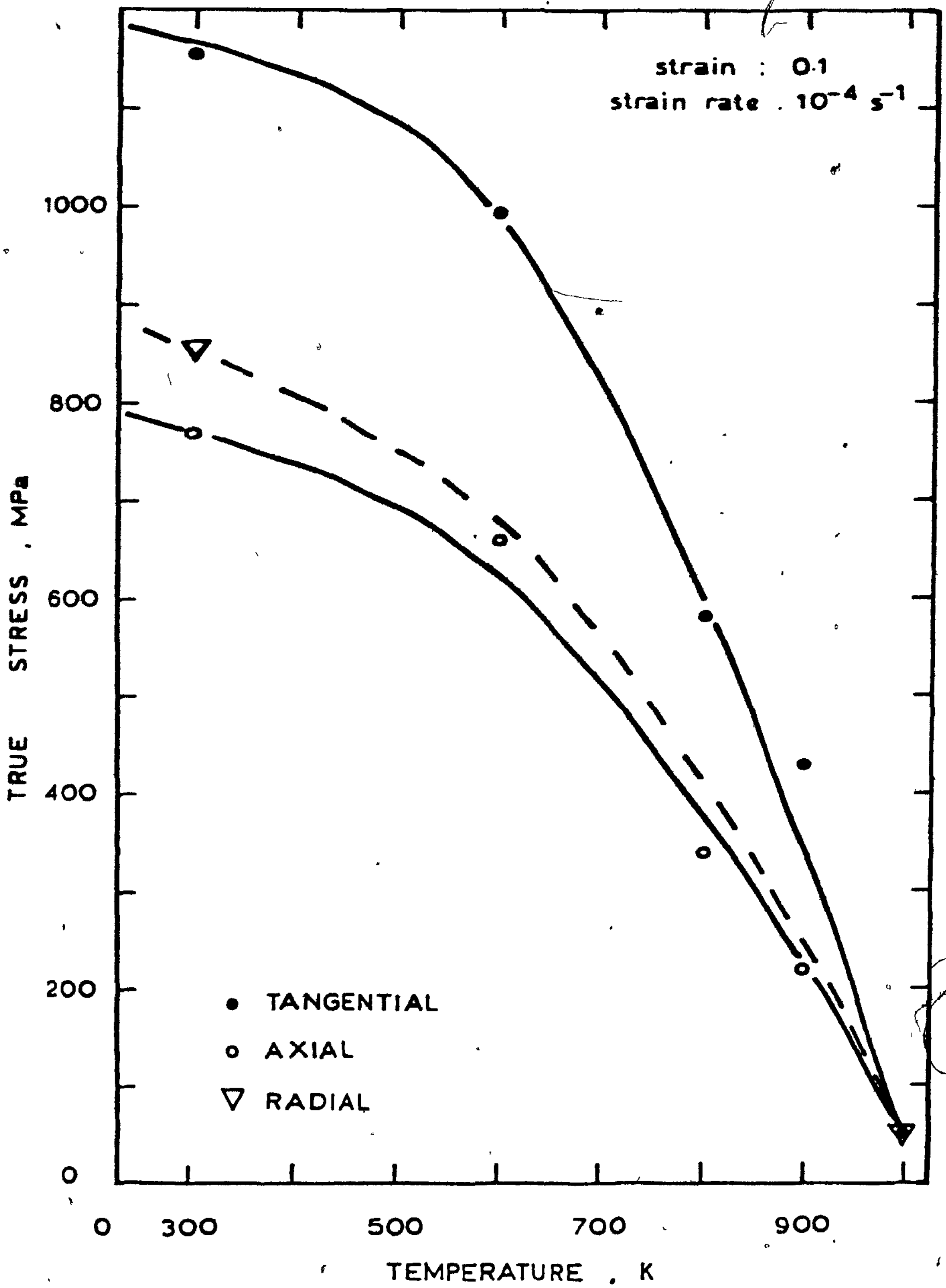

Figure 48. Effect of temperature and specimen orientation on the flow stress at $\varepsilon = 0.1$ for specimens machined from Excel alloy pressure tube, $10^{-4}s^{-1}$.

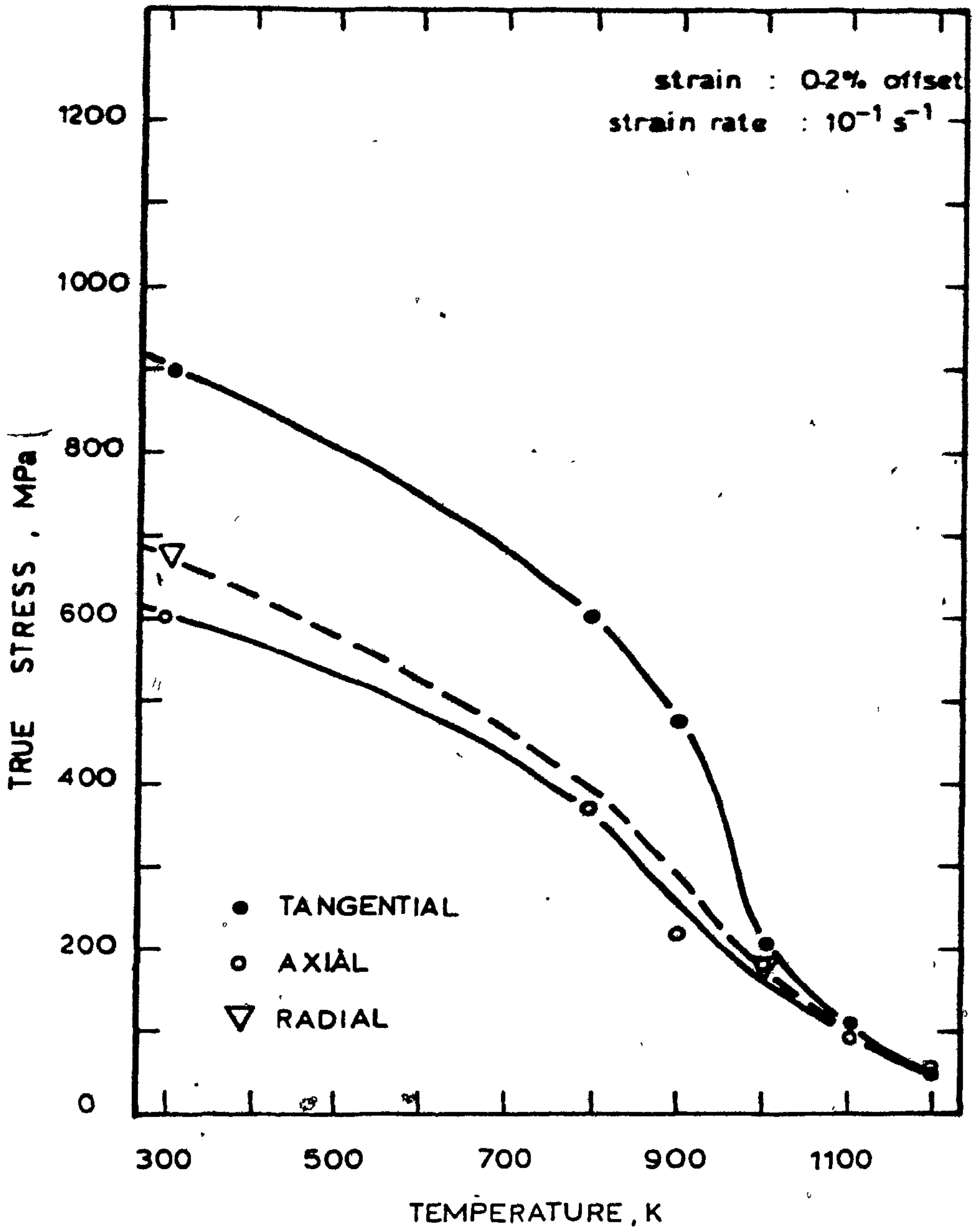

Figure 49. Effect of temperature and specimen orientation on the 0.2% yield stress of specimens machined from Excel alloy pressure tube, $10^{-1}s^{-1}$.

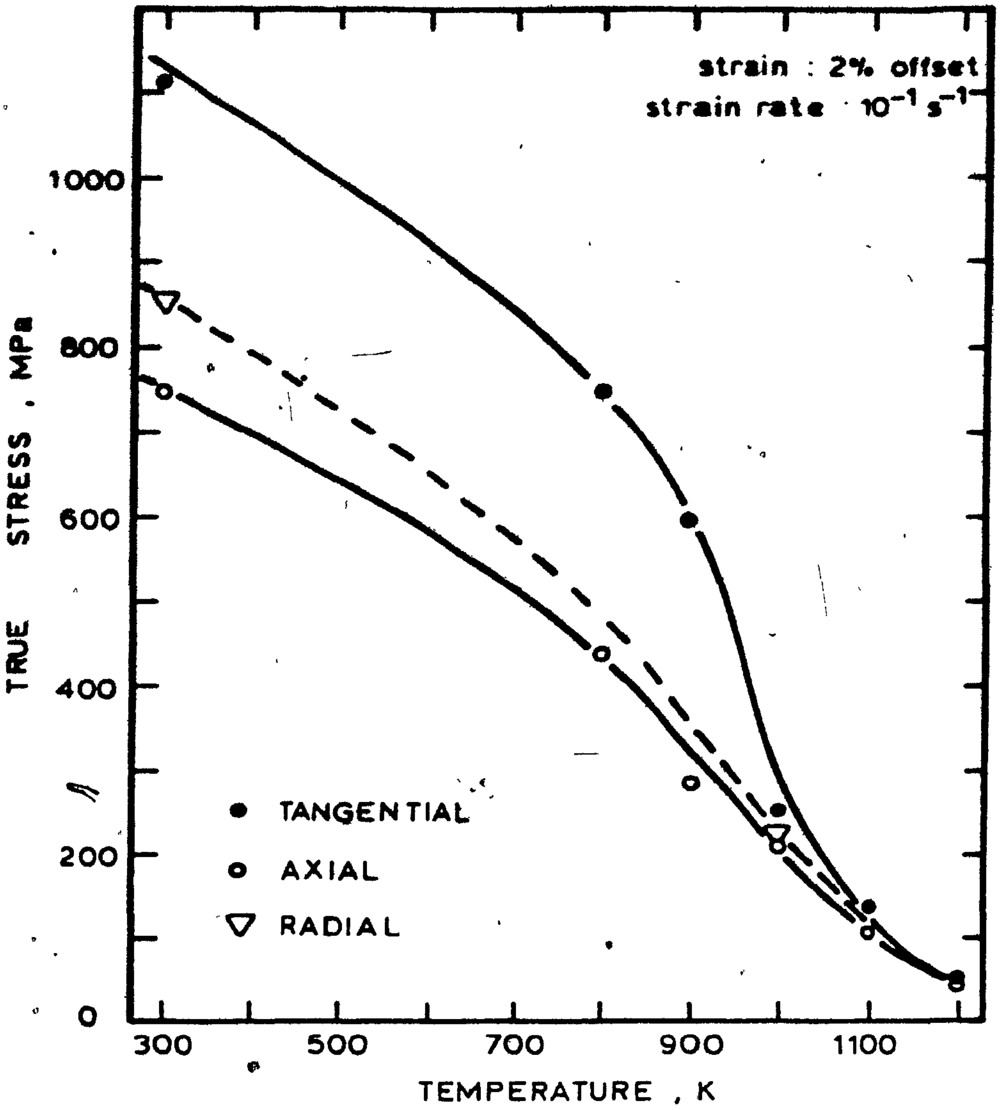

Figure 50. Effect of temperature and specimen orientation on the 2% yield stress of specimens machined from Excel alloy pressure tube, $10^{-1}s^{-1}$.

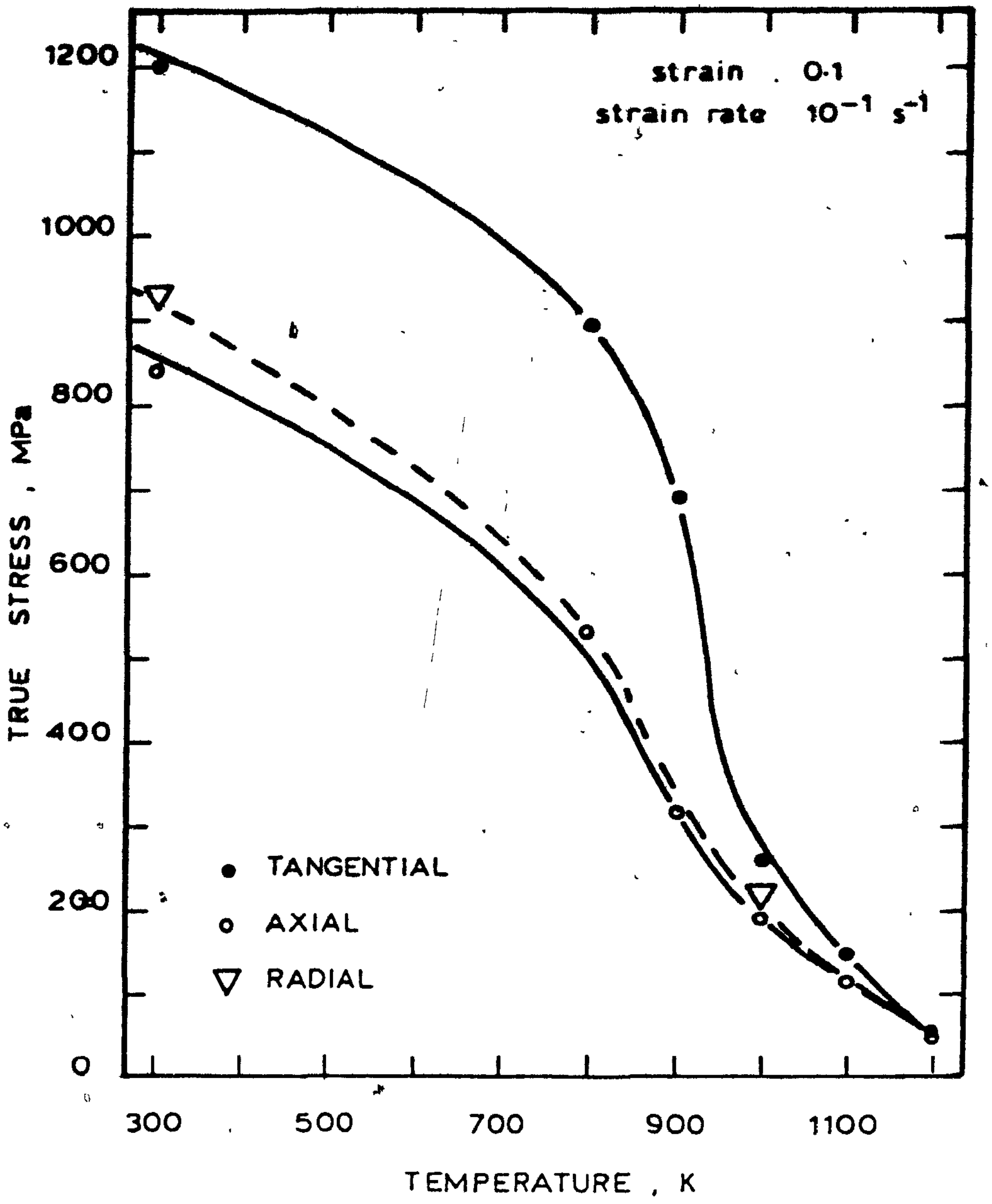

Figure 51. Effect of temperature and specimen orientation on the flow stress at $\varepsilon = 0.1$ for specimens machined from Excel alloy pressure tube, $10^{-1}s^{-1}$.

5.2.4 Effect of specimen orientation on the flow stress

The effect of specimen orientation on the flow stress can be observed from the results presented in Table XXI and Figs. 46 to 51. As can be seen, specimens with stress axes parallel to the circumferential direction of the pressure tube show the highest flow stresses at all temperatures and both strain rates. It can also be seen that specimens with this orientation remain the strongest after deformations of the order of 10% (see Figs. 46 and 51). By contrast, axial specimens showed the lowest flow stresses for a given temperature and strain rate, while radial specimens have flow stresses intermediate between those of the circumferential and axial specimens.

Flow stress ratios were calculated for the axial and radial directions, with respect to the circumferential direction, as a function of strain, strain rate and temperature; the results are given in Table XXII. It can be seen that at a strain rate of $10^{-4}s^{-1}$ and in the temperature range 298-800 K, the 0.2% yield stress in the circumferential direction is 25-30% larger than that in the axial direction, and approximately 15% larger with respect to the radial direction. After small deformations (2% offset), the axial stress ratios decrease to 0.66 at 600 and 800 K. At room temperature, however, the ratio seems to remain constant at 0.7.

Table XXII. Effect of specimen orientation and strain on the flow stress of Excel alloy pressure tube

Specimen	Temperature (K)	Strain Rate (s^{-1})	$\sigma_{.2\%}/\sigma_t$ *	$\sigma_{2\%}/\sigma_t$ *	$\sigma_{.1}/\sigma_t$ *
A 2	298	10^{-4}	0.74	0.69	0.67
A 8	600	10^{-4}	0.74	0.66	0.66
A X 2	800	10^{-4}	0.75	0.67	0.60
R 1	298	10^{-4}	0.87	0.80	0.72
A X 3	298	10^{-1}	0.66	0.66	0.70
A 7	800	10^{-1}	0.62	0.57	0.58
A X 1	900	10^{-1}	0.46	0.46	0.46
A 2 4	1000	10^{-1}	0.95	0.84	0.80
A 1 2	1100	10^{-1}	0.92	0.84	0.82
R 1 0	298	10^{-1}	0.74	0.75	0.76
R 5	1000	10^{-1}	0.91	0.84	0.80

---

*$\sigma_{0.2\%}$ = 0.2% offset yield stress

$\sigma_{2\%}$ = 2% offset yield stress

$\sigma_{0.1\%}$ = flow stress at $\varepsilon = 0.1$

σ_t = flow stress in the circumferential direction at the same level of strain.

At a strain rate of $10^{-1}s^{-1}$ and at 298-900 K, the 0.2% yield stress in the circumferential direction is about 25% larger with respect to the radial direction. However, these differences decrease considerably as the temperature is increased to 1000 and 1100 K, where the stress ratios are about 0.95. With increasing strain, the stress ratios seem to remain constant at 298 K and 800 K, although at 298 K it seems that, at strains greater than 10%, the ratio increases to about 0.70, a value near that corresponding to the radial direction. At higher temperatures ($T > 800$ K), increasing strain causes a decrease in the stress ratio. It is of interest to note that at 900 K the stress ratio at 0.2% offset deformation suddenly decreases to 0.46 and remains constant with increasing strain. This behaviour is another consequence of the anisotropic nature of the flow behaviour of this alloy. In the case of the radial direction at 1000 K, the stress ratio is similar to that of the axial direction (~0.95).

These results indicate that the anisotropic flow behaviour of the material under investigation is consistent with the experimentally determined distribution of basal poles in the pressure tube with the circumferential direction being the strongest and the axial direction the weakest. Furthermore, it seems that the strain hardening behaviour depends on the direction of testing and also depends on temperature for a given direction. Here again, the main differences are between the circumferential and axial directions since these are the ones with particularly different grain orientation distributions. In the case of circumferential specimens, the majority of the grains are oriented with their c axes near the compression axis and twinning is expected to occur at low temperatures and high strain rates. On the other hand, in the case of axial specimens, which have grains oriented with their c poles almost perpendicular to the stress axis, prismatic slip is expected to allow for the compressive strain applied to the specimens. Evidently, axial specimens are expected to be more ductile than circumferential ones since slip is generally easier to activate than twinning (see Chapter 2).

The true strain at fracture for axial and tangential specimens in the temperature range 298-900 K is given in Table XXIII and Fig. 52 for strain rates of 10^{-4} and $10^{-1}s^{-1}$. Fracture usually occurred in the compression specimens along planes at about 45 degrees to the stress axis and the fracture appearance was always of the ductile (shear) type. As can be seen from Fig. 52, the fracture strain increases rapidly in the temperature range 600-800 K at $10^{-4}s^{-1}$ for the tangential specimens. At lower temperatures, the strain to fracture remains constant and, at $10^{-1}s^{-1}$, the same behaviour is followed up to 900 K. By contrast, axial specimens tested at temperatures higher

Table XXIII. Effect of specimen orientation, temperature and strain rate on the true strain to fracture for Excel alloy

Specimen	Temperature (K)	Strain Rate (s^{-1})	True Strain to Fracture
T 2	298	10^{-4}	0.14
T 9	600	10^{-4}	0.13
T A 3	800	10^{-4}	0.25
A 2	298	10^{-4}	0.21
A 8	600	10^{-4}	0.19
T A 2	298	10^{-1}	0.13
T 7	800	10^{-1}	0.14
T 5	900	10^{-1}	0.13
A X 3	298	10^{-1}	0.23
A 7	800	10^{-1}	0.30

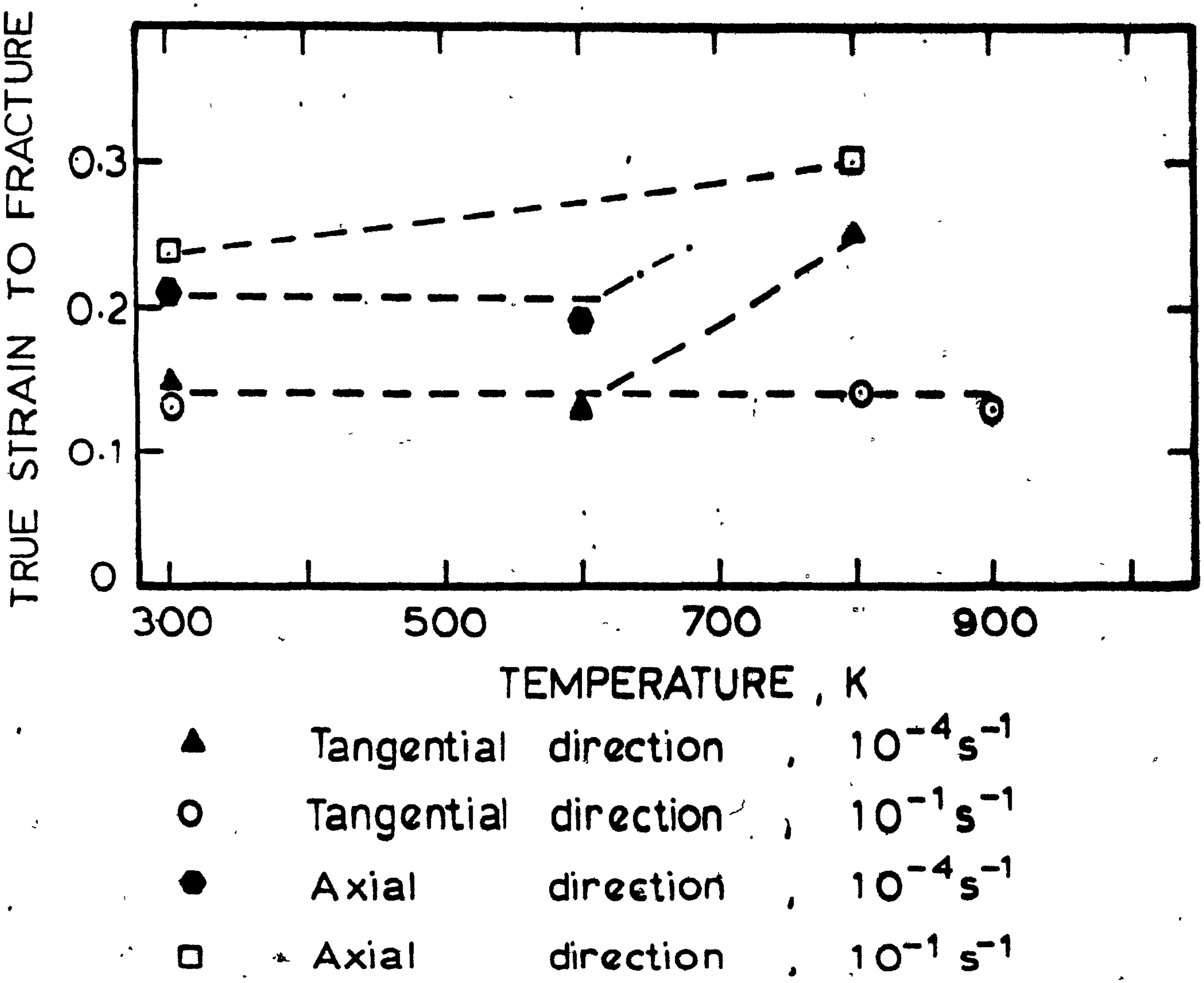

Figure 52. Effect of specimen orientation, strain rate and temperature on the true strain to fracture.

than 600 K at $10^{-4}s^{-1}$ did <u>not</u> fail and the increase in ductility follows the usual behaviour as the temperature is increased. At a strain rate of $10^{-1}s^{-1}$, the strain to fracture increases slowly in the temperature range 300-800 K; at still higher temperatures, the specimens did <u>not</u> fail.

Another important observation was that, in the specimens that fractured, the strains in directions perpendicular to the stress axis were small. However, when fracture did not occur, the cross-section of the specimens had an elliptical shape indicating that the principal strains perpendicular to the stress axis were of different magnitudes. For an isotropic material, the strain tensor in a uniaxial compression test is given by

$$\bar{\varepsilon} = \begin{bmatrix} \varepsilon_1 & o & o \\ o & \varepsilon_2 & o \\ o & o & \varepsilon_3 \end{bmatrix} \qquad (5.1)$$

where ε_1 is the compressive strain along the stress axis, and ε_2 and ε_3 are the principal tensile strains in the two other mutually perpendicular directions and are related by

$$\varepsilon_2 = \varepsilon_3 = \frac{-\varepsilon_1}{2} \qquad (5.2)$$

Thus a uniform uniaxial compressive stress causes a uniform tensile strain in directions perpendicular to the stress axis and the cross-section of the specimen after straining must be uniformly circular.

Table XXIV gives the final dimensions of two axial specimens after straining at 800 K and $10^{-4}s^{-1}$ and 900 K and $10^{-1}s^{-1}$. The presence of friction and possibly shearing effects were both evident, $(\varepsilon_1 + \varepsilon_2 + \varepsilon_3 \neq 0)$, especially in the case of the specimen tested to a strain beyond 0.5. The increase in volume observed indicates that cavitation and crack formation were occurring in these tests, and that voids were being opened up in the specimen interior. Such internal damage was not produced at the higher temperatures. It is also evident that mechanical anisotropy in these specimens results in non-uniform diametral strains and elliptical final cross-sections. It should be pointed out that radial specimens showed the most uniform diametral deformation.

The behaviour described above can be explained by considering the grain orientation distributions in the specimens. Figure 35(b) shows that the axial specimens can accommodate a tensile strain in the direction perpendicular to the plane of the paper (say the Y direction) by prismatic slip. However, in the direction which is perpendicular to the stress axis and in the plane of the paper, i.e. for a tensile strain along the c axis (say the X direction), either $\{10\bar{1}2\}$ twinning or $<\vec{c} + \vec{a}>$ slip must be activated to allow for expansion in that direction.

Table XXIV. Anisotropy of straining in axial specimens machined from Excel alloy pressure tube

Specimen	T(K)	$\dot{\varepsilon}$ (s^{-1})	h_f(mm)	D*(mm)	d**(min)	ε_1	ε_2	ε_3
A24	800	10^{-4}	3.45	6.25	4.80	-0.553	0.446	0.182
A23	900	10^{-1}	3.65	5.90	4.75	-0.497	0.389	0.172

---

*D = major diameter

**d = minor diameter

These two mechanisms have higher CRSS's than prismatic slip and consequently the strains in the X and Y directions will not be uniform; instead, elliptical cross-sections will be formed, with the Y strains greater than those in the X direction. Table XXV gives a summary of the conditions for activation of the different mechanisms of deformation in zirconium and Zircaloys. From the table it can be deduced that if $\vec{c} + \vec{a}$ slip and twinning are not operative at a given temperature and strain rate, then fracture will occur. This was confirmed for the specimens tested at the lower temperatures (T < 900).

Finally, it is worth mentioning that this behaviour persisted up to 1100 K. At 1200 K, the cross-section of the specimens showed little or no eccentricity and the strain anisotropy seemed to disappear, as well as the tendency for the specimen volume to increase with strain. The anisotropy of flow stress at this temperature also seems to disappear, but the scatter in the data at high temperatures does not make possible the accurate determination of the flow stresses.

Table XXV. Deformation systems in α-Zirconium and Zircaloys

Type	Plane	Direction	Crystallographic Description	Temperature & Stress Range
Slip	Prism	a	$\{10\bar{1}0\}\langle 1\bar{2}10\rangle$	All temperatures Lowest stress system
Slip	Basal	<a>	$\{0001\}\langle 1\bar{2}10\rangle$	High temperatures
Slip	Pyramidal	<c + a>	$\{10\bar{1}1\}\langle 11\bar{2}3\rangle$	Intermediate temperature, High stress
Slip	Pyramidal	<c + a>	$\{11\bar{2}1\}\langle 11\bar{2}3\rangle$	High temperature, High stress
Twin	Pyramidal	<c + a>	$\{10\bar{1}2\}\langle \bar{1}011\rangle$	Intermediate temperature, c-axis tension
Twin	Pyramidal	<c + a>	$\{11\bar{2}1\}\langle \bar{1}\bar{1}26\rangle$	Low temperature, c-axis tension
Twin	Pyramidal	<c + a>	$\{11\bar{2}2\}\langle \bar{1}\bar{1}23\rangle$	Low-intermediate temperature, c-axis compression
Twin	Pyramidal	<c + a>	$\{10\bar{1}1\}\langle \bar{1}012\rangle$	Intermediate-high temperature, c-axis compression

CHAPTER 6

DISCUSSION

6.1 General Observations

The anisotropic mechanical behaviour of the material under investigation was represented in Figs. 46 to 51 above in the form of $\sigma(T)$ curves; from these data it was evident that the stress is a function of specimen orientation, as well as of strain rate and true strain. Furthermore, in Table XXII, the flow stress ratios were listed for axial and radial specimens, where these were normalized with respect to the flow stress for the tangential specimen at a given temperature and strain rate. It seems clear from the results at both strain rates that the anisotropy of flow stress decreases as the temperature is increased for temperatures higher than 900 K. At lower temperatures, however, the stress ratios remain almost constant; there is little change with increasing temperature at $10^{-4}s^{-1}$ and a small decrease with increase in temperature at $10^{-1}s^{-1}$. For example, the stress ratio decreases from 0.62 at 800 K to 0.46 at 900K. Similar behaviour is observed as the strain is increased. All these observations, as mentioned in the last chapter, can be explained in terms of the initial crystallographic texture of the material (see Figs. 33 and 34) and the resulting distribution of basal plane poles in specimens of the three different orientations utilized in this work (see Fig. 35). Two extreme cases can be noted: (i) that of c poles parallel to the compression axis (tangential specimens); and (ii) that of c poles perpendicular to the compression axis (axial specimens). From these observations it seems clear that different deformation mechanisms control the plastic flow behaviour of these two kinds of specimen and differences in the strain hardening behaviour are therefore expected. This is also apparent from the differences between the flow curves for these specimens (see Figs. 37, 38, 40 and 41). Thus, it can be said that both the yield stress and the subsequent strain hardening behaviour of the present material are determined by its initial texture.

This behaviour can be complicated still further by texture changes, i.e. grain reorientations, that can occur during continued deformation.

6.2 Influence of Basal Pole Orientation on the Flow Behaviour at Low Temperatures

From the results described in Chapter 5 it is apparent that the yield strength of the material tends to increase as the proportion of basal poles oriented parallel to the stress axis increases; i.e. the yield stress for tangential specimens is greater than that for axial specimens with radial specimens having intermediate yield strengths. The deformation systems in the axial and tangential specimens were illustrated in Fig. 35 above: $\{10\bar{1}0\}\langle 12\bar{1}0\rangle$ prism slip for the axial specimens and $\{11\bar{2}2\}\langle\bar{1}011\rangle$ twinning and/or $\vec{c} + \vec{a}$ slip for the tangential specimens. Thus, it seems that compressive deformation in the two extreme cases studied in this work is controlled: (i) by prismatic slip when the basal poles are oriented perpendicular to the stress axis; and (ii) by $c + a$ pyramidal slip and $\{11\bar{2}2\}$ twinning for compression parallel to the c axis. It is therefore to be expected that the yield stress of the alloy should increase with an increase in the proportion of basal poles oriented parallel to the stress axis; furthermore, prismatic slip should control the deformation process at very low proportions and $\langle\vec{c} + \vec{a}\rangle$ slip and/or $\{11\bar{2}2\}$ twinning at large proportions. In fact, the behaviour in these two extreme cases can be modeled in terms of the behaviour of suitably oriented single crystals.(76,77)

However, the above arguments seem to contradict the observations of authors(13,18,22) who have investigated the CRSS's for the activation of the various deformation mechanisms in zirconium and zirconium alloys. Figure 53 shows the CRSS as a function of temperature for different deformation mechanisms and, as can be seen, the CRSS for prismatic slip is lower than that required to activate any other mechanism. Further, it has been found(22) that the stress levels for activation of any of the c + a mechanisms for c axis compression are at least 1.5 to 2.0 times that for prism slip.

Ballinger and Pelloux(80) have found, by studying the yield stress of Zircaloy-2 as a function of the Kearn texture number f (effective fraction of basal poles oriented in a given direction),(78) that the increase in yield stress with increasing f is not due to c + a axis deformation (either twinning or slip) becoming increasingly predominant. Instead, they suggest that the material can be treated as a composite of two components: one component that is difficult to deform and another which is easily deformed. In addition, in this model, compatibility between the two fractions must be satisfied. Their model is represented schematically in Fig. 54. The basis of the treatment is that the basal poles are not considered to be completely parallel to a given direction; instead,

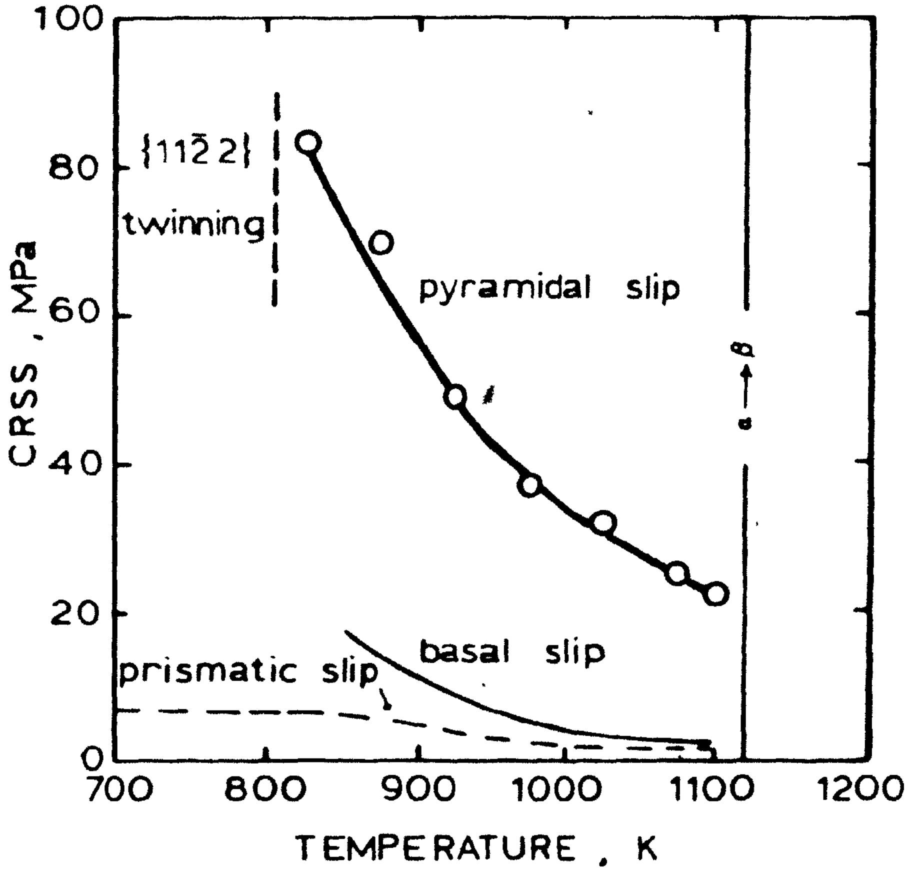

Figure 53. Temperature dependence of the Critical Resolved Shear Stress (CRSS) for prismatic, pyramidal and basal slip in Zr. (Reference 25)

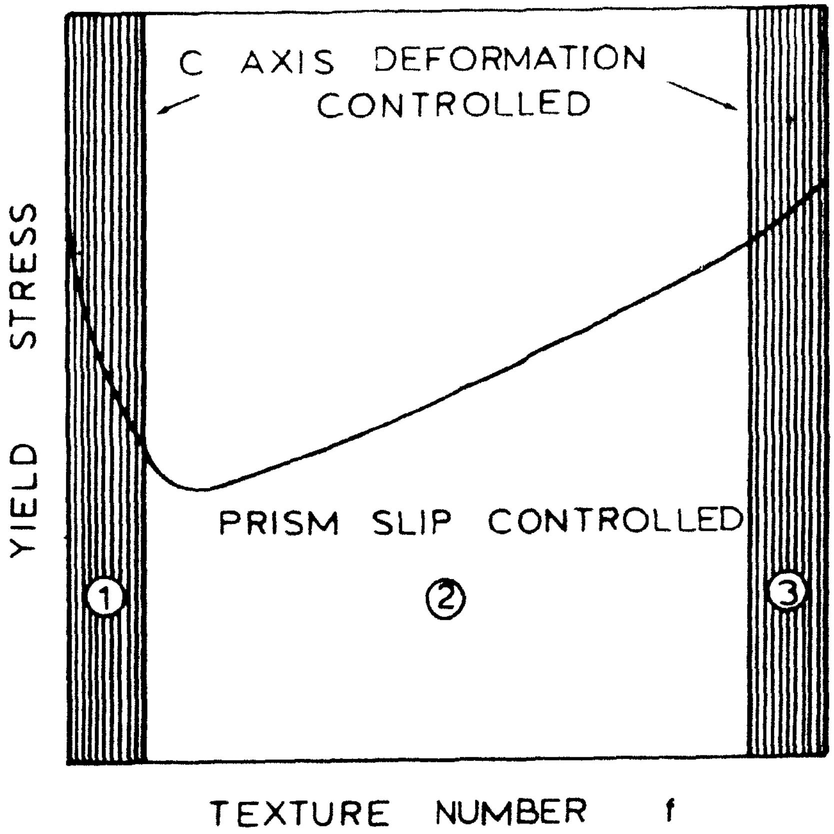

Figure 54. Qualitative behaviour of the yield stress vs. texture number, F, for a textured polycrystalline material.

the texture of the polycrystal is taken as involving a finite proportion of grains favourably oriented for prism slip. It can be seen from Fig. 54 that in region 2, i.e. for textures intermediate between those of the axial and circumferential specimens in the present work, plastic deformation of the material will be controlled by prism slip. As f increases in region 2, more grains are oriented parallel to the 'hard' direction and, as a consequence, fewer grains are available for prism slip. In addition, grains with 'hard' orientations impose constraints on the 'soft' grains and the net result is an increase in flow stress as f increases. In regions 1 and 3, i.e. for the cases of the axial and circumferential specimens in this work, the material can be expected to behave in a way similar to that of a single crystal, as mentioned before. When the c poles are oriented perpendicular to the stress axis, however, deformation will be controlled by the c axis tensile or compressive mechanism due to the Poisson effect; i.e. extension or reduction parallel to the loading axis, respectively, must be accompanied by lateral contraction or expansion. Thus, for textures approaching the ideal, the c mechanism must operate.

The argument summarized above seems reasonable for tensile loading perpendicular to the c axis since in this case compressive strains must be accommodated in directions perpendicular to the stress axis and, as indicated in Fig.

35, this can only be achieved by the operation of a ·c + a· mechanism. However, in the case of compressive deformation perpendicular to the c axis, as in the present case, tensile strains must be accommodated. Figure 35 shows that this can be achieved by the operation of the $10\bar{1}2$ $\bar{1}011$ twinning system. Several investigators have determined that the stress level for activation of this kind of twin is approximately the same as for prism slip. Recently, Tome and Kocks(79) have calculated the stress axis orientation domains in which plastic deformation in tension or compression requires the activation of a vertex of the single crystal yield surface with which at least one twinning system is associated; i.e. the $10\bar{1}2$, $\bar{1}011$ twin system. These domains are shown in Fig. 55. As can be seen, compression in directions perpendicular to the c axis requires the activation of the ·$10\bar{1}2$· twin system. The importance of the operation of this twin system in a compression test is that, when it operates, a rotation of the c axis of approximately 85 degrees occurs (see Fig. 56), which tends to align the c pole with the compression axis. This grain reorientation requires that a ·c + a· mechanism operate in order to permit further compressive deformation; in this case the material contains a double texture of basal poles, one approximately perpendicular and one parallel to the stress axis. Thus, for the case of the axial specimens in this work, it seems that the initial controlling mecha-

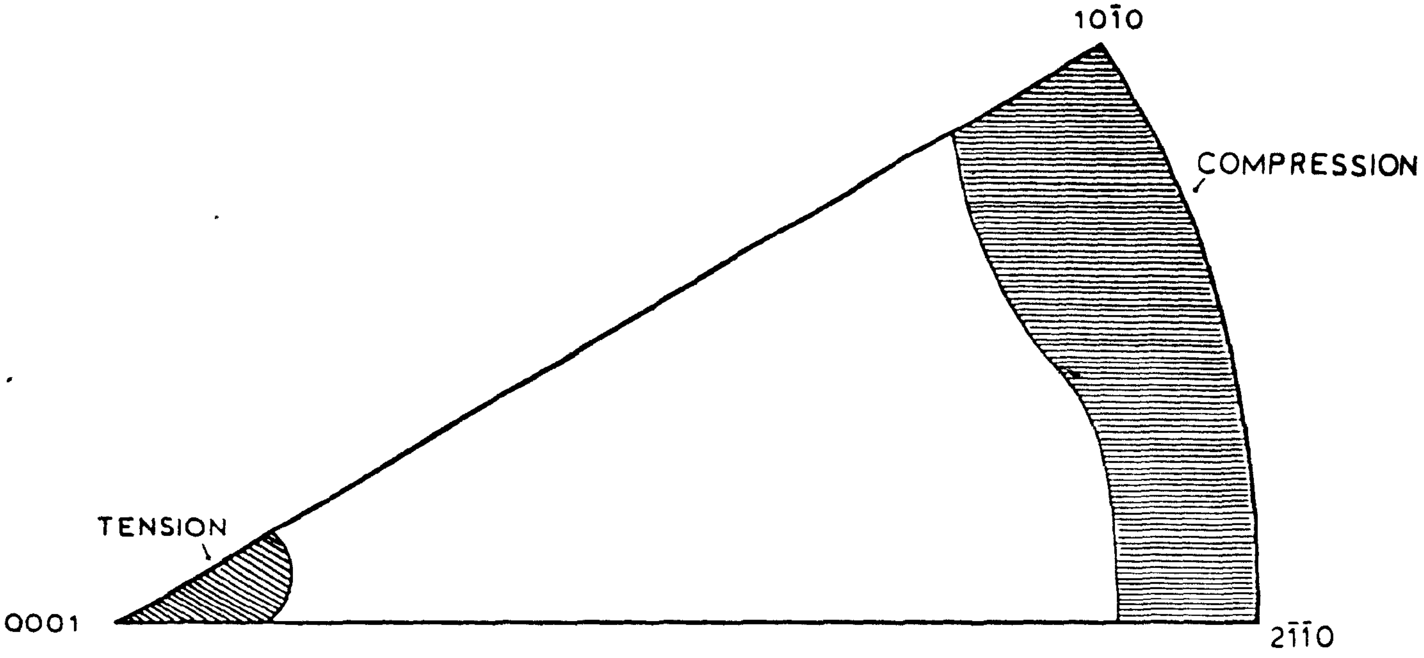

Figure 55. Orientation domains of the stress axis with respect to the crystal axes for which deformation in tension or compression requires the activation of a vertex of the yield surface with at least one associated {1012}<1011> twinning system.

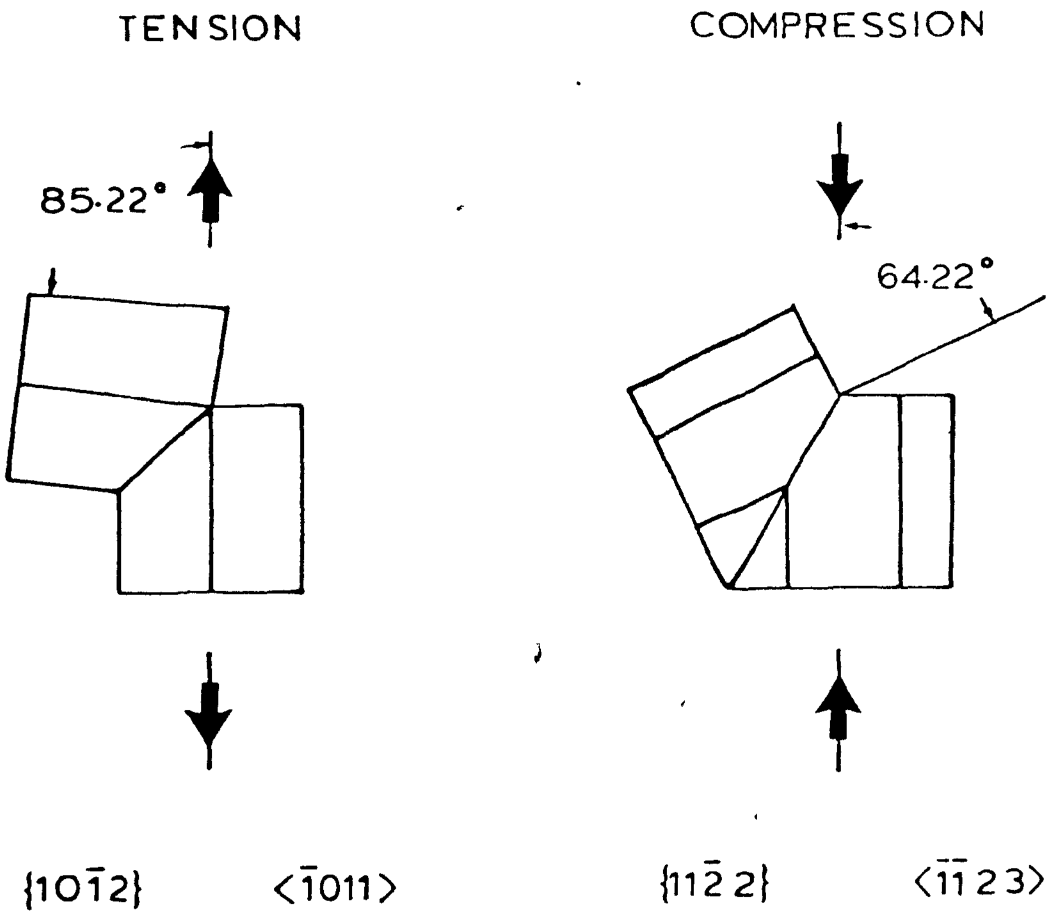

Figure 56. Texture rotations brought about by the operation of twinning deformation mechanisms in zirconium.

nism is prismatic slip for deformation parallel to the stress axis and $\{10\bar{1}2\}$ twinning for deformation perpendicular to the stress axis. This behaviour will be discussed further in the next section.

6.3 Texture Rotation and the Strength Differential Effect

The effect of the need to accommodate tensile strains in directions perpendicular to the stress axis in a compression test on axial specimens was shown in the last section to be one of c pole reorientation towards the loading direction by means of $\{10\bar{1}2\}$ twinning. The fact that different deformation mechanisms govern the overall deformation behaviour depending on the orientation of the basal plane poles can be explained in the light of the effect that tensile deformation has on the flow behaviour of axial specimens. When axial specimens are loaded in tension, axial extension is accomplished by $\{10\bar{1}2\}$ twinning, while strains perpendicular to the stress axis must be accommodated by a $<\vec{c} + \vec{a}>$ deformation mechanism. Neither of the two possible $<\vec{c} + \vec{a}>$ mechanisms produces much reorientation of the c poles, i.e. no texture rotation is produced; thus, as mentioned earlier, deformation is controlled by $<\vec{c} + \vec{a}>$ deformation via the Poisson relationship. By comparing the strain hardening rate of axial and circumferential specimens tested in compression, Figs. 37, 38, 40 and 41, it can be seen that deformation controlled by the operation of a $<\vec{c} + \vec{a}>$ mechanism produces a higher strain hardening rate. The net result is the production of a strength differential in axial specimens tested in compression and tension. This effect is clearly illustrated in Fig. 43.

The $SD[=(\sigma_C - \sigma_T)/2]$ is plotted as a function of true strain in Fig. 57. It is evident that the initial flow stress is slightly higher in compression than in tension. However, the plateau in the compressive flow curve together with the higher initial strain hardening rate during tensile deformation causes the SD to decrease up to strains of about 0.06. The fact that the SD increases with strain after this minimum and eventually becomes positive again at approximately 0.11 true strain is evidence that enough texture rotation has occurred to change the controlling deformation mechanism from that of tensile twinning in directions perpendicular to the stress axis to that of $<\vec{c} + \vec{a}>$ deformation parallel to the stress axis. As mentioned earlier, this deformation mode exhibits a higher strain hardening rate, which leads to the crossing of the two flow curves.

There still remains the question of which of the two possible $<\vec{c} + \vec{a}>$ mechanisms is actually controlling the deformation. Figure 56 shows that the texture rotation

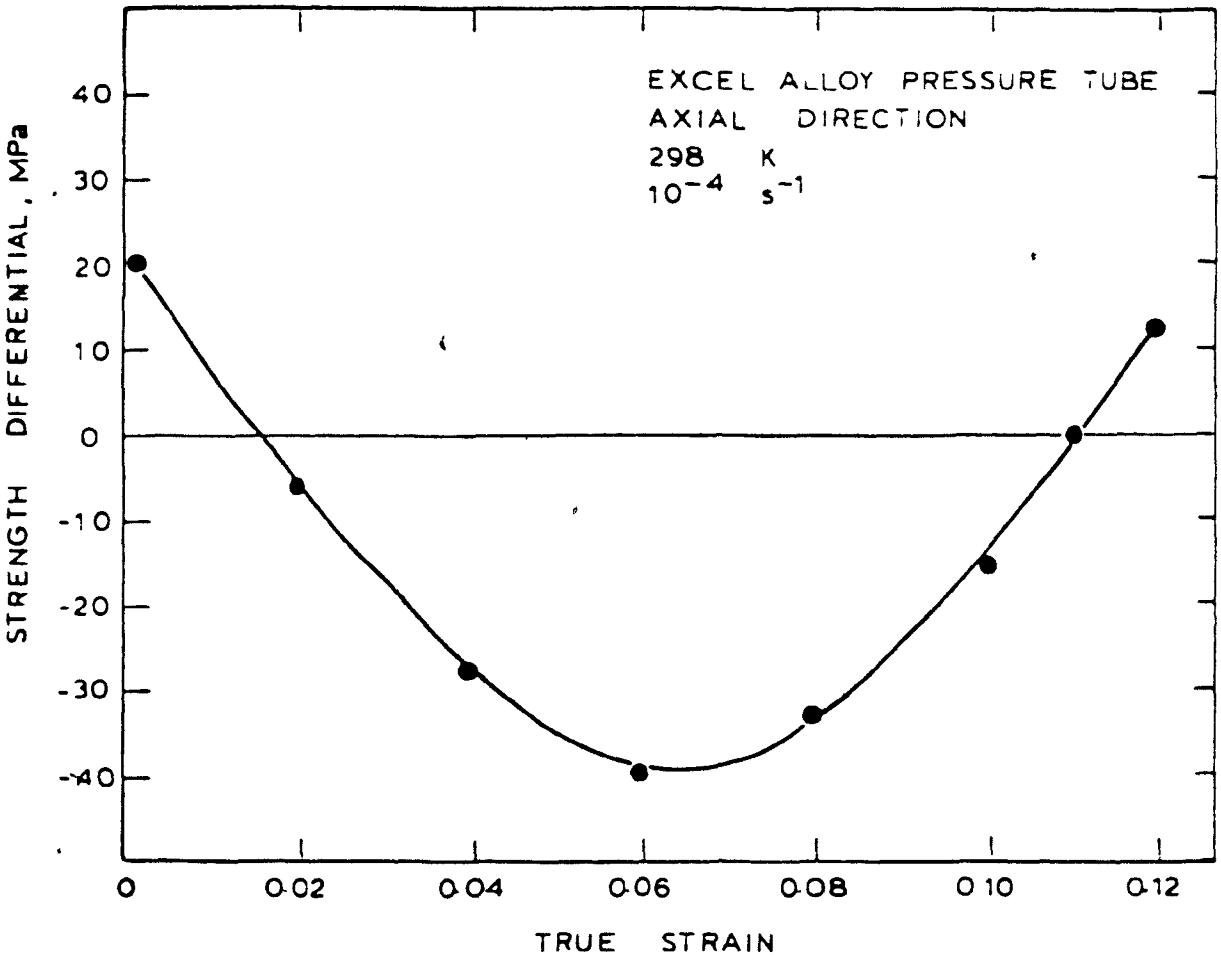

Figure 57. Strength Differential (SD = $\frac{\sigma_c - \sigma_t}{2}$) in axial specimens of Excel alloy pressure tube tested at 298 K and $10^{-4}s^{-1}$.

due to $\{11\bar{2}2\}$ twinning in pure zirconium single crystals is 64°. Such rotation is not apparent in the circumferential specimens tested in compression at temperatures up to 900 K. Thus, it seems that a $\langle \vec{c} + \vec{a} \rangle$ slip mechanism is the controlling mode of deformation for both compression along the c axis and tension perpendicular to the c pole through Poisson's ratio. This observation is in agreement with the interpretations of other investigators.(31,38,80) The effect of texture rotation on the deformation behaviour was confirmed by Ballinger and Pelloux by means of X-ray diffraction studies, transverse strain ratio measurements, and texture number measurement as a function of strain. Their results are consistent with the present data for Excel alloy.

6.4 Fracture Behaviour

As mentioned in Chapter 5, the compression specimens of Excel alloy fractured by a shear process with a fracture occurring on planes inclined at 45 degrees to the stress axis. The fracture appearance was always of the ductile type and the only difference between the axial and circumferential specimens was the magnitude of the true strain to fracture (see Fig. 52). This type of behaviour has been described previously by Blaz and Jonas(79) at 775 K.

Jensen and Backofen(33) also observed by means of electron microscopy that the fracture process in Zircaloy-4 tested in plane strain compression along the c axis involves highly localized shear along bands of $\{11\bar{2}4\}$ orientation. They found that under certain conditions continued shear within bands heavily populated with $\vec{c} + \vec{a}$ dislocations can be arrested at obstacles such as grain boundaries; nevertheless, damage due to the nucleation and growth of voids around precipitate particles could lead to fracture when enough of these weakened shear bands are linked together.

The differences in strain to fracture between axial and circumferential specimens of Excel alloy pressure tube can be explained in this way. The localization of flow due to shear band formation requires the operation of $\vec{c} + \vec{a}$ slip, which is the operative mode of deformation for reduction along the c axis (circumferential specimens). Thus, shear bands will form readily in this kind of specimen and fracture will occur early in the deformation process. By contrast, the operation of $\vec{c} + \vec{a}$ slip during the compression of axial specimens first requires that texture rotation occur due to the operation of the tensile $\{10\bar{1}2\}$ twinning mechanism to align the basal poles parallel to the stress axis; a greater amount of deformation is therefore required before flow localization can occur by the formation of shear bands.

6.5 Effect of Temperature and Strain Rate

The differences between deformation parallel and perpendicular to the basal pole mentioned in the last sections are still evident at temperatures up to 600 K at $10^{-4}s^{-1}$ and 800 K at $10^{-1}s^{-1}$. However, the behaviour is now complicated by the activation of new deformation systems which cannot operate at lower temperatures, i.e. basal slip at $T > 800$ K and $\{10\bar{1}1\}$ twinning at $T > 500$ K. Furthermore, the compressive deformation mode parallel to the basal pole, $\vec{c} + \vec{a}$ slip, is thermally activated(33) and thus exhibits a higher sensitivity to temperature.

Further increases in temperature involve the activation of other softening processes such as recovery and recrystallization. At sufficiently high temperatures, these become more important than the texture effects.

CHAPTER 7

CONCLUSIONS

1) The results of this experimental investigation show that the mechanical behaviour of cylindrical specimens taken from an Excel alloy pressure tube is a strong function of the initial crystallographic texture of the specimens, i.e. the texture of the pressure tube itself.

2) The flow stress increases with the proportion of basal plane poles oriented parallel to the stress axis for specimens loaded in compression. Tangential specimens, with most of the grains oriented with their c axes parallel to the compression axis, showed the highest flow stresses while axial specimens, which had most of the grains oriented with c axes perpendicular to the compression axis, showed the lowest flow stresses. Radial specimens, with no particular concentration of c axes parallel to the compression axis, displayed intermediate flow stresses.

3) The fact that different shapes of flow curves were obtained depending on the specimen orientation, and that different strain hardening behaviours were also displayed, suggests that different deformation mechanisms operate depending on the orientation of the basal poles with respect to the stress axis. In this respect, tangen-

tial specimens showed the highest rates of work hardening and axial specimens the lowest for the initial stages of deformation up to ~ 0.1.

4) The strong strength differential effect in axial specimens loaded in tension and compression is a result of the different deformation mechanisms required to accommodate the strains (compressive or tensile) perpendicular to the stress axis.

5) The fact that tensile strains perpendicular to the compression axis are accommodated by $\{10\bar{1}2\}$ tensile twinning causes a reorientation of the c poles parallel to the compression axis. The increase in the strain hardening rate of axial specimens after about 0.1 true strain is evidence for such texture rotation. This effect indicates that the mechanism controlling the deformation process changes from $\{10\bar{1}2\}$ twinning in directions perpendicular to the stress axis, to $\vec{c} + \vec{a}$ slip parallel to the stress axis.

6) The lack of evidence for texture rotation in tangential specimens suggest that $\{\vec{c} + \vec{a}\}$ pyramidal slip is the deformation mechanism for reduction parallel to the c axis in Excel alloy.

7) The ductility of Excel alloy is directly related to the ability of the material to accommodate reductions

parallel to the stress axis and it increases with an increase in temperature as the $\vec{c} + \vec{a}$ slip mechanism is highly sensitive to thermal activation.

8) The anisotropic mechanical behaviour of Excel alloy follows the same pattern at strain rates of 10^{-1} and $10^{-4} s^{-1}$ over the temperature range 295-900 K. A further increase in temperature causes thermally activated processes, such as dynamic recovery, to become more important than the texture effects and the anisotropy decreases considerably.

Suggestions for Future Work

Although the present analysis of the anisotropy of mechanical properties of Excel alloy has been carried out in an essentially qualitative way, it demonstrates the highly complex way in which the yield stress and the subsequent strain hardening behaviour are affected by the ability of the material to deform by twinning as well as by slip under a given set of experimental conditions. The fact that the activation of the different deformation modes depends on the initial crystallographic texture, the evolution of this texture as the material is strained, as well as on the temperature and strain rate, and that, up to now, no satisfactory model has been proposed for the prediction of such a complex behaviour justifies the need for further research in this area. From the results of the present investigation, the following topics are suggested for future work:

1) The effect of the extent to which twinning can occur during the straining of a polycrystalline aggregate should be studied in detail since this process strongly affects the development of the texture.

2) In the case of material with a texture similar to that of the axial specimens in this work, the effects of basal pole reorientation should be studied in a quanti-

tative manner, especially as regards the effects of temperature and strain rate. This work should be supported by X-ray and electron diffraction studies on specimens deformed to different strains.

3) Such studies should be carried out under stress and strain states more representative of actual fabrication and operating conditions for this alloy: e.g. plane strain compression and tension, and biaxial stressing.

4) Studies of flow localization due to shear band formation and the effects of changes in the strain path on the localization of shear could lead to a better understanding of the fracture and flow softening behaviour of the present material.

REFERENCES

1. M.H. Yoo: Metallurgical Transactions A; 12 A, 409 (1981).
2. S.F. Pugh: Philosophical Magazine; 45, 823 (1954).
3. J.R. Rice and R. Thomson: Philosophical Magazine; 29, 73 (1974).
4. R. von Mises: Z. Angew, Math. Mech.; 6, 85 (1928).
5. G.I. Taylor: Journal of the Institute of Metals; 62, 307 (1938).
6. U.F. Kocks: Acta Metallurgica; 6, 85 (1958).
7. G.W. Grooves and A. Kelly: Philosophical Magazine; 8, 877 (1963).
8. U.F. Kocks: Philosophical Magazine; 10, 187 (1964).
9. U.F. Kocks and D.G. Westlake: Transactions TMS-AIME; 239, 1107 (1967).
10. J.W. Hutchinson: Proc. R. Soc. London; A348, 101 (1976).
11. J.W. Hutchinson: Metallurgical Transactions A; 8A, 1465 (1977).
12. E.J. Rapperport: Acta Metallurgica; 3, 208 (1955).
13. E.J. Rapperport: Acta Metallurgica; 7, 254 (1959).
14. E.J. Rapperport and C.S. Hartley: Transactions AIME; 218, 869 (1960).
15. D.G. Westlake: Acta Metallurgica; 9, 327 (1961).
16. A.H. Cottrell and B.A. Bilby: Philosophical Magazine;

42, 573 (1951).

17. N. Thompson and D.J. Millard: Philosophical Magazine; 43, 422 (1952).

18. A. Akhtar and A. Teghtsoonian: Acta Metallurgica; 19, 655 (1971).

19. R.E. Reed-Hill and J.L. Martin: Transactions AIME; 230, 780 (1964).

20. D.G. Westlake: Journal of Nuclear Materials; 13, 113 (1964).

21. A. Akhtar: Acta Metallurgica; 21, 1 (1973).

22. D.O. Hobson: Transactions AIME, 242, 1105 (1968).

23. M.L. Picklesimer: Electrochemical Technology; 4, 289 (1966).

24. E. Tenckhoff: Z. Metallkunde; 63, 192 (1972).

25. A. Akhtar: Journal of Nuclear Materials; 47, 79 (1973).

26. S.R. MacEwen, J. Faber and A.P.L. Turner: Acta Metallurgica; 31, 657 (1983).

27. R.G. Ballinger: "The Anisotropic Behaviour of Zircaloy-2." Garland Publishing Inc., New York & London, 1979.

28. R.E. Reed-Hill: TMS-AIME Conference V.25 "Deformation Twinning," 1964.

29. R.E. Reed-Hill: "An evaluation of the role of deformation twinning in the plastic deformation of zirconium." 2nd Quart. Prog. Report, Jan. 1962; 3rd Quart. Prog. Report, April 1962; 4th Quart. Prog. Report,

July 1962; Contract AT(38-1)-252, Metallurgical Research Lab., University of Florida.

30. M.L. Picklesimer· GEAP-4989 (II) Paper No. 13 (1962).

31. J.A. Jensen and W.A. Backofen: Canadian Metallurgical Quarterly; 11, 39 (1972).

32. G.E. Lucas and A.L. Bement: Journal of Nuclear Materials; 55, 246 (1975).

33. S.R. MacEwen, C.E. Ells and O.T. Woo: Journal of Nuclear Materials; 101, 336 (1981).

34. B.A. Cheadle, C.E. Coleman and H. Licht: Nuclear Technology; 57, 413 (1982).

35. A.J. Blank: Proc. AIME Conf. Reactor Metals, Buffalo, N.Y. 575 (1958).

36. W. Evans, J.E. Le Surf and W.R. Thomas: AECL-2890 (1967) Atomic Energy of Canada, Ltd.

37. C.D. Williams and R.W. Gilbert: Journal of Nuclear Materials; 18, 161 (1966).

38. J. Winton and R.A. Murgatroyd: Electrochemical Technology, 4, 358 (1966).

39. R.F. Hehemann: Canadian Metallurgical Quarterly; 11, 201 (1972).

40. B.A. Cheadle and S.A. Aldridge: Journal of Nuclear Materials; 47, 255 (1973).

41. D. Weinstein: Electrochemical Technology; 4, 307 (1966).

42. C.E. Ells and B.A. Cheadle: Journal of Nuclear Materials; 23, 257 (1967).

43. S.A. Aldridge and B.A. Cheadle: Journal of Nuclear Materials; 42, 32 (1972).

44. W.R. Thomas, et al: Proc. 3rd Int. Conf. Peaceful Uses Atomic Energy; 9, 80 (1964).

45. B.A. Cheadle and W. Evans: AECL-2652 (1966) Atomic Energy of Canada Ltd.

46. R. Bullough and M.H. Wood: Journal of Nuclear Materials; 90, 1 (1980).

47. P.A. Ross-Ross, C.E.L. Hunt: Journal of Nuclear Materials; 26, 2 (1968).

48. P.A. Ross-Ross: ASM Publication No. P9-101.

49. F.A. Nichols: Materials Science and Eng.; 6, 167 (1970).

50. E.F. Ibrahim: AECL-2528 (1965) Atomic Energy of Canada, Ltd.

51. W.J. Langford: AECL-3516 (1970) Atomic Energy of Canada, Ltd.

52. E.F. Ibrahim: Proc. ASTM Symp. on Applications-Related Phenomena in Zirconium and its Alloys; STP-458.

53. J. Schroeder and J.J. Holicky: Journal of Nuclear Materials; 33, 52 (1969).

54. V. Fidleris: Journal of Nuclear Materials; 26, 51 (1968).

55. C.E. Ells and V. Fidleris: Electrochemical Technology; 4, 268 (1966).

56. R.K. McGeary and B. Lustman: Transactions AIME; 191, 944 (1951).

57. B.A. Cheadle and C.E. Ells: Electrochemical Technology; 4, 329 (1966).

58. B.A. Cheadle, C.E. Ells and W. Evans: Journal of Nuclear Materials; 23, 199 (1967).

59. B.A. Cheadle and C.E. Ells: Transactions AIME; 233, 1044 (1965).

60. M.L. Picklesimer: Proc. USAEC, Symp. on Zr-Alloy Development GEAP-4089, II, 13-0 (1962).

61. B.A. Wilcox: "Basic strengthening mechanisms in refractory metals," in Refractory Metal Alloys, p. 1, Plenum Press, Inc., NY, 1968.

62. D.L. Douglass: Atomic Energy Review; 1 (4), 71 (1963).

63. MTS Product Specification: 433 Processor Interface units, MTS Systems Corp., 1981.

64. C.D. Williams: Reactor Technology; 13, 147 (1970).

65. C.D. Williams, C.E. Ells and P.R. Dixon: Canadian Metallurgical Quarterly; 11, 257 (1972).

66. E.F. Ibrahim, E. Price and A. Wysiekiersky: Canadian Metallurgical Quarterly; 11, 273 (1972).

67. B.A. Cheadle, R.A. Holt, V. Fidleris, A.R. Causey and V.F. Urbanic: ASTM-STP 754, 193 (1982).

68. D.J. Abson and J.J. Jonas: Journal of Nuclear Materials; 42, 73 (1972).

69. R.A. Holt: Journal of Nuclear Materials, 8, 419 (1979).

70. E.F. Ibrahim and B.A. Cheadle: Unpublished work.

71. E.F. Ibrahim: AECL-5805 (1977) Atomic Energy of Canada, Ltd.

72. E.F. Ibrahim: Personal communication.

73. L.G. Schultz: J. App. Phys.; 20, 1030 (1949).

74. J.E. Winegar: AECL-5626 (1977) Atomic Energy of Canada, Ltd.

75. R. Hill: Proc. of the Royal Society of London; A193, 281 (1948).

76. G.P. Kiely: CRNL-2523 Atomic Energy of Canada, Ltd., 1983.

77. C. Tomé and U.F. Kocks: To be published.

78. J.J. Kearns: WAPD-TM-472 (1965).

79. C. Tomé and U.F. Kocks: Unpublished work.

80. R.G. Ballinger and R.M. Pelloux: Journal of Nuclear Materials, 97, 231 (1981).

```
10 REM ------------------------------------------------------------
20 REM
30 REM                 A  P  P  E  N  D  I  X     I
40 REM
100 REM -----------------------------------------------------------
200 REM
300 REM          CONSTANT TRUE STRAIN RATE COMPRESSION TEST
400 REM
500 REM            PROGRAMMED BY ARMANDO SALINAS RODRIGUEZ
600 REM
700 REM       REVISED WITH THE ASSISTANCE OF RICHARD BERGLY OF MTS
800 REM
900 REM -----------------------------------------------------------
1000 DIM P(220),S(220),X(405),S3(220),E2(220),P3(220)
1100 QUIT
1200 FG1(0)
1300 MSW1(2)
1400 CNTR(3)
1500 PRINT "WOULD YOU LIKE TO RECALL DATA FOR PLOTTING ? (Y OR 'CR')",
1600 INPUT I1$
1700 REM ----------------------------------------------------------
1800 REM                     EXPERIMENTAL CONDITIONS
1900 REM ----------------------------------------------------------
2000 PRINT "TEST I D ",\INPUT N$
2100 PRINT "MATERIAL ",\INPUT M$
2200 PRINT "HEAT TREATMENT ",\INPUT H$
2300 PRINT "TEST TEMPERATURE ",\INPUT T$
2400 PRINT "TOTAL STRAIN ",\INPUT E
2500 PRINT "TRUE STRAIN RATE (1/SEC) ",\INPUT E1
2600 PRINT "STROKE RANGE (MM)",\INPUT R1
2700 PRINT "LOAD RANGE (LBS) ",\INPUT R2
2800 PRINT "SPECIMEN HEIGHT (MM)",\INPUT L0
2900 PRINT "SPECIMEN DIAMETER (MM)",\INPUT D0
3000 A0=PI*D0^2/4
```

```
3100 T=E/E1\K=2047/R1\K1=2047/R2
3200 IF I1$<"Y" THEN 3800
3300 GOSUB 19900
3400 GO TO 11300
3500 REM -----------------------------------------------------------------
3600 REM          CALCULATE FUNCTION GENERATOR PARAMETERS
3700 REM -----------------------------------------------------------------
3800 IF T>200 THEN 4600
3900 N=200
4000 IF T>=100 THEN 4700
4100 IF T>=50 THEN 4800
4200 IF T>=10 THEN 4900
4300 IF T>=5 THEN 4500
4400 R=100\A4=0\N=100\GO TO 5000
4500 R=50\A4=1\GO TO 5000
4600 N=400\R=1\A4=7\GO TO 5000
4700 R=5\A4=5\GO TO 5000
4800 R=10\A4=4\GO TO 5000
4900 R=20\A4=2
5000 X(1)=4095*N/T/R/2
5100 U=T
5200 Y=10
5300 Y2=INT(9*Y+.5)
5400 REM ----------------------------------------------------------------
5500 REM                  SET UP THE SYSTEM
5600 REM ----------------------------------------------------------------
5700 CNTR(3)\MSW1(2)\FG1(0)
5800 PRINT "CHECK THE FOLLOWING:"\PRINT
5900 PRINT "DC ERROR IS 0"
6000 PRINT "REMOTE/LOCAL SWITCH TO REMOTE"
6100 PRINT "SPAN 1 IS AT ZERO"
6200 PRINT "STROKE CONTROL"\PRINT
6300 PRINT "PRESS RETURN TO CONTINUE";\INPUT F$\PRINT
6400 PRINT "TURN ON THE HYDRAULICS"\PRINT
6500 PRINT "SET 'SPAN 1' TO 10"
```

```
6600 PRINT \PRINT "PRESS RETURN TO CONTINUE", INPUT F$\PRINT
6700 REM--------------------------------------------------------------
6800 REM                   DUMP CHECK
6900 REM--------------------------------------------------------------
7000 EDMP
7100 SDMP(1,A)\IF A=0 THEN 7800
7200 PRINT "DUMP CARD PROBLEM. UNABLE TO FINISH TEST "
7300 PRINT \PRINT "TURN OFF THE HYDRAULICS "
7400 STOP
7500 REM ------------------------------------------------------------
7600 REM               EXPERIMENT STARTS
7700 REM ------------------------------------------------------------
7800 PRINT "IS THE PISTON IN THE RIGHT POSITION ?";\INPUT A2$
7900 IF A2$<"Y" THEN 7800
8000 DACQ(0,S1,2,0)
8100 FOR I=2 TO N+2
8200 X(I)=K*L0*(EXP(-E*(I-2)/N)-1)+S1+.5\NEXT I
8300 X=N+2
8400 TIME(Y,E9)\DACQ(3,P,0,U)\DACQ(6,S,2,2)
8500 FG1(X,1,7,A4)\STAR
8600 IF P<=100 THEN 8600
8700 QUIT(1)\P=101\S=P
8800 TIME(Y2,E8)\STAR
8900 BUF1(Z)\IF Z>-1 THEN 8900
9000 QUIT
9100 REM --------------  EXPERIMENT IS FINISHED  ----------------------
9200 DACQ(0,S4,2,0)
9300 REM ------------ RETURN PISTON TO INITIAL POSITION --------------
9400 FOR I=S4 TO 0
9500 FG1(I)
9600 NEXT I
9700 PRINT "YOU CAN TURN OFF THE HYDRAULICS NOW"
9800 PRINT "HIT A 'CR' WHEN READY",\INPUT C$
9900 PRINT "WOULD YOU LIKE TO STORE THE DATA ?",\INPUT C$
10000 IF C$<"Y" THEN  GO TO 11300
```

```
10100 REM ---------------------------------------------------------------
10200 REM                    STORING EXPERIMENTAL DATA ON A FLOPPY DISK
10300 REM ---------------------------------------------------------------
10400 FOR I=P+2 TO 3 STEP -1\P(I)=P(I-2)\NEXT I
10500 P(1)=P\P(2)=S1\P=P+2
10600 OPEN "DX1:"&N$ FOR OUTPUT AS FILE #1
10700 AOUT(P,1,0,E4)
10800 AOUT(S,1,1,E5)
10900 CLOSE #1
11000 REM ---------------------------------------------------------------
11100 REM                    CALCULATE TRUE STRESS & TRUE STRAIN
11200 REM ---------------------------------------------------------------
11300 U=0
11400 FOR I=1 TO P
11500 L=ABS(P(I))*9.81/K1/1000/2.2046
11600 L1=6.58960E-05*L^2-.0164243*L
11700 L2=(S(I)-S1)/K
11750 L3=L0+L2-L1
11800 E2(I)=-LOG(L3/L0)
11810 S3(I)=1000*L*L3/A0/L0
11820 PRINT S3(I),E2(I),L,L2,L1
11840 IF U<S3(I) THEN U=S3(I)
11860 NEXT I
11900 PRINT "MAX. STRESS : "U
12000 PRINT "ENTER MAX. STRESS LEVEL FOR SCAL";\INPUT U
12100 REM ---------------------------------------------------------------
12200 REM               PLOT TRUE STRESS VS. TRUE STRAIN
12300 REM ---------------------------------------------------------------
12400 CNTR(3)\CNTR(0)\PHYL(100,900,80,700)
12500 SCAL(0,0,E,0,U)\CNTR(2)\PLOT(0,0)
12600 LABL("TRUE STRAIN","TRUE STRESS MN/M^2",.1,50,1)
12700 LABL(" "," ",.05,10,3)\CNTR(0)\PLOT(0,0)
12800 PLOT(E,0)\PLOT(E,U)\PLOT(0,U)\PLOT(0,0)\CNTR(1)
12900 COMM("SAMPLE #",.5*E,.96*U)\PRINT N$
13000 COMM(M$,.5*E,.93*U)\COMM(H$, 5*E,.9*U)
```

```
13100 COMM(T$,.5*E,.87*U)\COMM("STRAIN RATE",.5*E,.83*U)
13200 PRINT E1\COMM(" /SEC",.9*E,.83*U)\CNTR(2)
13300 PLOT(0,0)\CNTR(0)
13400 FOR I=1 TO P\MAPK("+",E2(I),S3(I))\NEXT I
13500 CNTR(2)\INPUT F$\CNTR(3)
13600 PRINT "WAS THE STRESS LEVEL OK  ? ",\INPUT J$
13700 IF J$<>"Y" THEN 12000
13800 CNTR(3)
13900 REM ---------------------------------------------------------------
14000 REM           PLOT INITIAL YIELD PEGION
14100 REM ---------------------------------------------------------------
14200 PRINT "TO PLOT THE INITIAL YIELD REGION HIT A 'CR'",\INPUT C$
14300 PRINT "ENTER MAX  STRESS LEVEL FOR SCAL",\INPUT U
14400 PPINT "ENTER MAX  STRAIN FOR SCAL",\INPUT E5
14500 CNTR(3)
14500 CNTR(0)\PHYL(100,900,80,700)
14700 SCAL(0,0,E5,0,U)\CNTR(2)\PLOT(0,0)
14800 LABL("TRUE STRAIN","TRUE STPESS MN/M^2",E5/5,U/10,1)
14900 LABL(" "," ",E5/10,U/50,3)\CNTR(0)\PLOT(0,0)\PLOT(0,U)
15000 PLOT(E,U)\PLOT(E,0)\PLOT(0,0)\CNTR(1)
15100 COMM("INITIAL YIELD PEGION",E5/2,.96*U)
15200 COMM("SAMPLE #",E5/2,.92*U)\PPINT N$\CNTR(2)
15300 PLOT(0,0)\CNTR(0)
15400 FOR I=1 TO P\MARK("+",E2(I),S3(I))\NEXT I
15500 CNTR(2)\INPUT F$\CNTR(3)\CNTR(1)
15600 PRINT "WAS THE PLOT OK  ?",\INPUT H$
15700 IF H$<>"Y" THEN 14300
15800 REM ---------------------------------------------------------------
15900 REM                PLOT TRUE STRAIN VS  TIME
16000 REM ---------------------------------------------------------------
16100 V=T
16200 CNTR(3)\CNTR(0)\PHYL(100,900,80,700)
16300 SCAL(0,0,T,0,E)\CNTR(2)\PLOT(0,0)
16400 LABL("TIME","TRUE STRAIN",T/10,.1,1)
16500 CNTR(0)\PLOT(0,0)\PLOT(T,0)\PLOT(T,E)\PLOT(0,E)
```

```
16600 PLOT(0,0)\CNTR(0)\A8=0
16700 FOR I=1 TO 100
16800 A8=A8+V/1000\MARK(".",A8,E2(I))\NEXT I
16900 FOR I=101 TO P\A8=A8+9*V/1000
17000 MARK(".",A8,E2(I))\NEXT I
17100 CNTR(1)\COMMK("STRAIN-TIME", .6*T, .96*E)
17200 COMMK("SAMPLE # ", .6*T, .92*E)\PRINT N$
17300 REM ---------------------------------------------------------------------
17400 REM                 PLOT LOAD VS. TIME
17500 REM ---------------------------------------------------------------------
17600 CNTR(2)\INPUT F$\CNTR(3)\CNTR(1)
17700 PRINT "ENTER ESTIMATED LOAD LEVEL IN LB FOR SCAL";\INPUT F
17800 CNTR(3)\CNTR(0)\PHYL(100,900,80,700)
17900 SCAL(0,0,T,0,F)\CNTR(2)\PLOT(0,0)
18000 LABL("TIME","LOAD",T/10,F/20,1)
18100 CNTR(0)\PLOT(0,0)\PLOT(T,0)\PLOT(0,0)
18200 PLOT(0,F)\PLOT(0,0)
18300 CNTR(0)\A8=0
18400 FOR I=1 TO 100
18500 A8=A8+V/1000\P3(I)=ABS(P(I))/K1
18600 MARK(".",A8,P3(I))\NEXT I
18700 FOR I=101 TO P\A8=A8+9*V/1000
18800 P3(I)=ABS(P(I))/K1\MARK(".",A8,P3(I))\NEXT I
18900 CNTR(1)\COMMK("LOAD-TIME", .7*T, .96*F)
19000 COMMK("SAMPLE # ", .7*T, .92*F)\PRINT N$
19100 CNTR(2)\INPUT F$\CNTR(3)\CNTR(1)
19200 PRINT "WAS THE LOAD LEVEL RIGHT ?";\INPUT W$
19300 IF W$<"Y" THEN  GO TO 17700
19400 CNTR(3)
19500 STOP
19600 REM ---------------------------------------------------------------------
19700 REM            RECALL PREVIOUS TEST DATA FOR PLOTTING
19800 REM ---------------------------------------------------------------------
19900 OPEN "DX1:TEST"&N$ FOR INPUT AS FILE #1
20000 AINP(P,1,0,E6)
```

```
20100 P=P(1)\S1=P(2)\P=P-2
20200 FOR I=1 TO P\P(I)=P(I+2)\NEXT I
20300 AINP(S,1,1,E7)
20400 CLOSE #1
20500 RETURN
20600 REM ---------------------------------------------------------------

READY
```

APPENDIX II

Effect of Machine Curves on Experimentally Determined Flow Curves

When a specimen is loaded in a testing machine, the load is transmitted to the entire system as well as to the specimen. While the specimen deforms first elastically and then plastically, the testing system is designed so that it only deforms elastically. Table A-1 gives the Young's modulus of Excel alloy as a function of orientation within the tube. As can be seen, Young's modulus is high enough that the elastic deformation of test specimens during a compression test will be small, of the order of 10^{-3}, and the initial slope of the flow curves should be very high, in terms of *plastic* strain. Because of the anisotropy of Young's modulus, the slope of the loading curve varies with specimen orientation. Figure A-1 shows the flow curve for an axial specimen tested at room temperature and a strain rate of $10^{-1}s^{-1}$ as obtained after the experiment; it can be seen that the initial slope is not very high. It was therefore decided that a correction should be made for the effect of machine compliance; this term refers to the elastic deformation undergone by the testing system as a result of its reaction to the force applied to the specimen. Any element in the system, such as the loading frame,

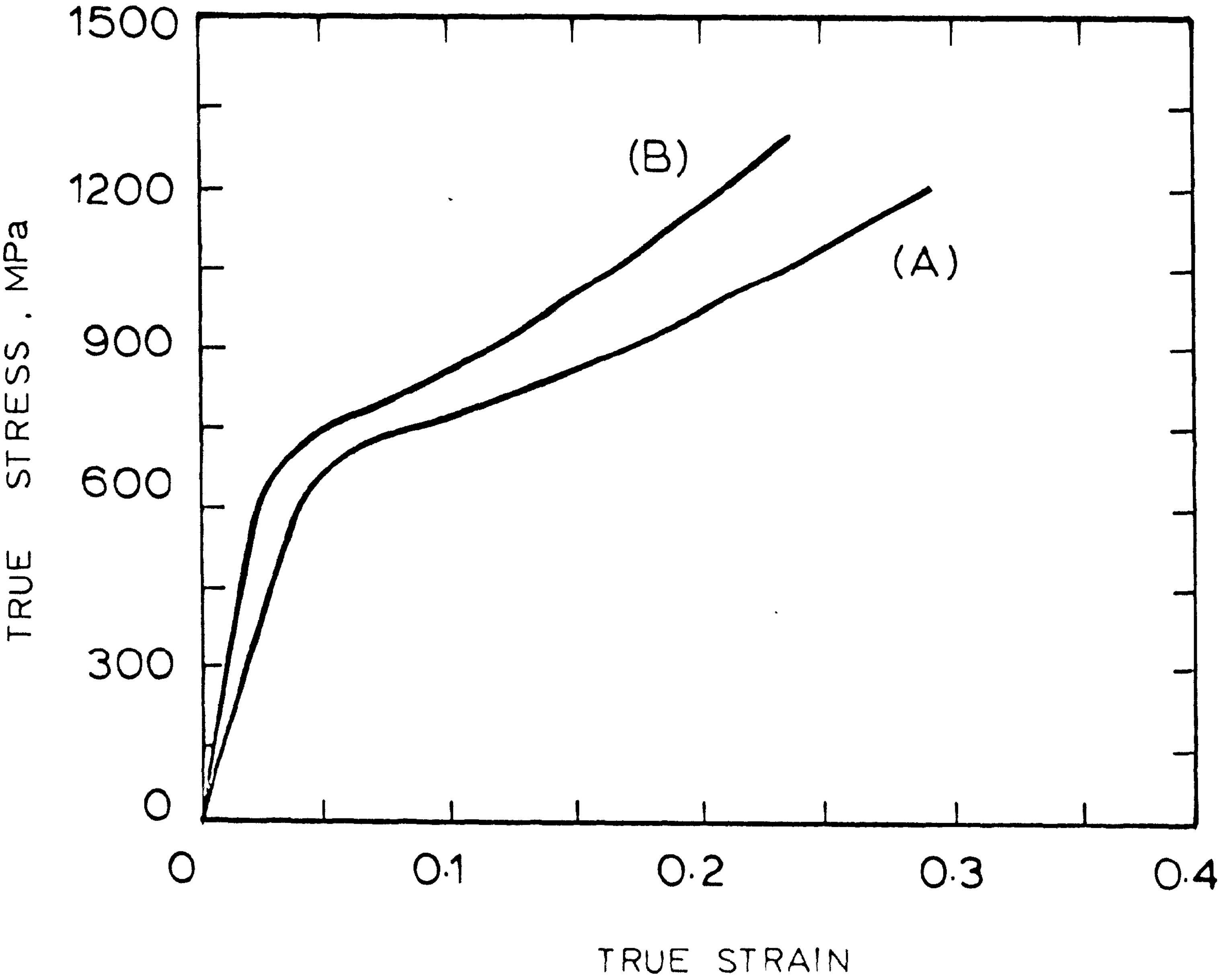

Figure A-1. Effect of the machine compliance on the experimentally determined flow curve of an axial specimen tested at 298K and 10^{-1} s^{-1}. (A) Experimental, (B) Corrected for machine compliance.

the tungsten compression tooling, the stainless steel extension rods, load cell, actuator, etc., contributes to the compliance of the load train.

As mentioned in Chapter 4, the crosshead or actuator velocity in the system utilized to carry out this work is decreased exponentially to allow for the decrease in height of the specimen. However, the actuator velocity is kept constant within each segment created by the Hardware Segment Generator (which is part of the processor interface). Thus, at any given instant within a segment, the testing machine applies a constant <u>total</u> displacement rate; that is, the sum of the elastic displacement of the specimen, the plastic displacement of the specimen, and the displacement (opposite in sign) resulting from the elasticity of the testing machine is held constant. Thus, if the actuator velocity is v, then after a time interval Δt the total displacement of the actuator is $v\Delta t$ and this must be equal to the sum of the elastic displacements of the specimen and machine and the plastic displacement of the specimen during the same interval,

$$v\Delta t = \frac{\Delta F}{K} + \frac{\Delta\sigma \cdot L}{E} + \Delta\varepsilon_p \cdot L \qquad \text{(A1)}$$

where ΔF = increase in applied force during Δt

K = elastic compliance of the testing system

$\Delta\sigma$ = increase in stress on the specimen during Δt

E = Young's modulus of the specimen

$\Delta\varepsilon_p$ = increase in true plastic strain during Δt

L = 'instantaneous'height of the specimen.

Thus, solving for $\Delta\varepsilon_p$:

$$\Delta\varepsilon_p = \frac{v\Delta t}{L} - \frac{\Delta\sigma}{E} - \frac{\Delta F}{K} \qquad \text{(A2)}$$

It is therefore evident that the plastic strain increment is affected by both the elastic strain increment in the specimen as well as the incremental elastic compliance of the test system.

Figure A-2 shows a schematic diagram of the effect of machine compliance on the determination of the current height of the specimen. As can be seen, the position of the specimen/compression rod interface, which is a measure of the specimen height, is determined at the uppermost end of the loading train by the LVDT connected to the actuator. Thus, if S1 is the initial position of the actuator in machine units (2047 m.u. = 10 mm) and its position after the interval Δt is S(i), also in machine units, then the ram displacement (in mm) is given by

$$dr = \frac{S(i) - S1}{K} \qquad \text{(A3)}$$

where K (=2047/10) is a calibration factor for the LVDT that depends on the range in which the associated transducer conditioner is operated (range 4 in the present case).

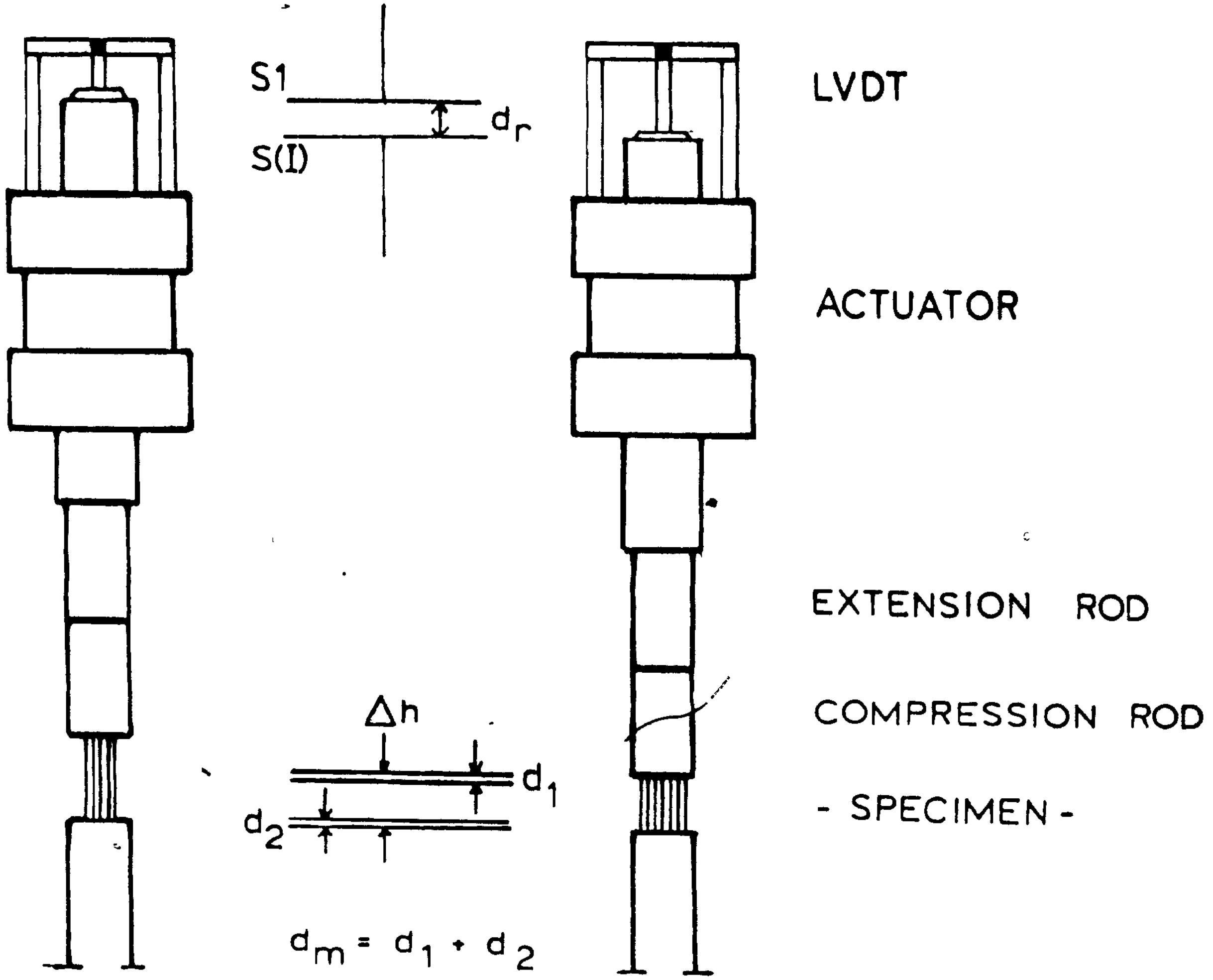

Figure A-2. Effect of machine compliance on the determination of the actual height of a specimen.

Note that dr is a negative quantity as $|S(i)| > |S1|$ and both are always negative during a compression test. This ram displacement is equal to the instantaneous change in height of the specimen Δh, plus the small elastic displacement due to the compliance of the system dm represented in Fig. A-2 as the single contributions of the upper and lower anvils:

$$dr = \Delta h + dm \tag{A4}$$

$$h = ho + dr - dm \tag{A5}$$

where dm depends on the load applied to the system. The functional relationship between dm and the load was determined experimentally for the testing system. This was carried out by loading the system in the absence of a specimen and selecting the load cell output signal as the controlled variable. With the aid of the computer and using the FG1(ARG 1) routine, increasing loads were applied to the system and the displacement was read out with the aid of a multimeter. The following relationships were used to obtain the values of load and displacement from the multimeter readings:

$$\begin{aligned} 2047 \text{ machine units} &= -10 \text{ V} = -10 \text{ mm} \\ 2047 \text{ machine units} &= -10 \text{ V} = -100 \text{ KN} \end{aligned} \tag{A6}$$

Table A-2 and Fig. A-3 give the results and the calibration curve obtained; it can be seen that the calibration curve is relatively linear, as may be expected for elastic behaviour. Nevertheless, a second degree polynomial was fitted to the experimental data and very good correlation was obtained. The functional relationship between load and displacement characterizing the elastic compliance of the testing system is given by

$$dm = 6.058962 \times 10^{-5} F^2 - 0.0164243 F \qquad (A7)$$

As mentioned earlier, Eq.(A7) confirms that the elastic compliance of the testing system increases as the load is increased. Equation (A5) indicates that the instantaneous height of the specimen is larger than the value obtained directly from the LVDT readings, i.e. h - ho + dr, so that the current area of cross-section is smaller than the value obtained when the compliance is neglected. Thus the corrected flow curve shown in Fig. A-1 is displaced to the left and the stress for a given strain is higher than in the uncorrected curve. This is a direct result of the underestimation of the cross-section of the sample mentioned above.

Table A-1. Young's Modulus for Excel alloy

Direction	Youngs' Modulus (GPa)
Axial	94.8
Radial	94.6
Circumferential	103.0

Table A-2. Effect of load on the elastic compliance of the testing system

Load (KN)	Displacement (mm)
2.33	.047
4.33	.086
6.89	.117
9.19	.152
11.5	.186
13.82	.219
16.02	.247
18.33	.278
20.67	.307
22.98	.337
27.54	.396
32.15	.454
36.71	.51
41.36	.568
45.93	.623

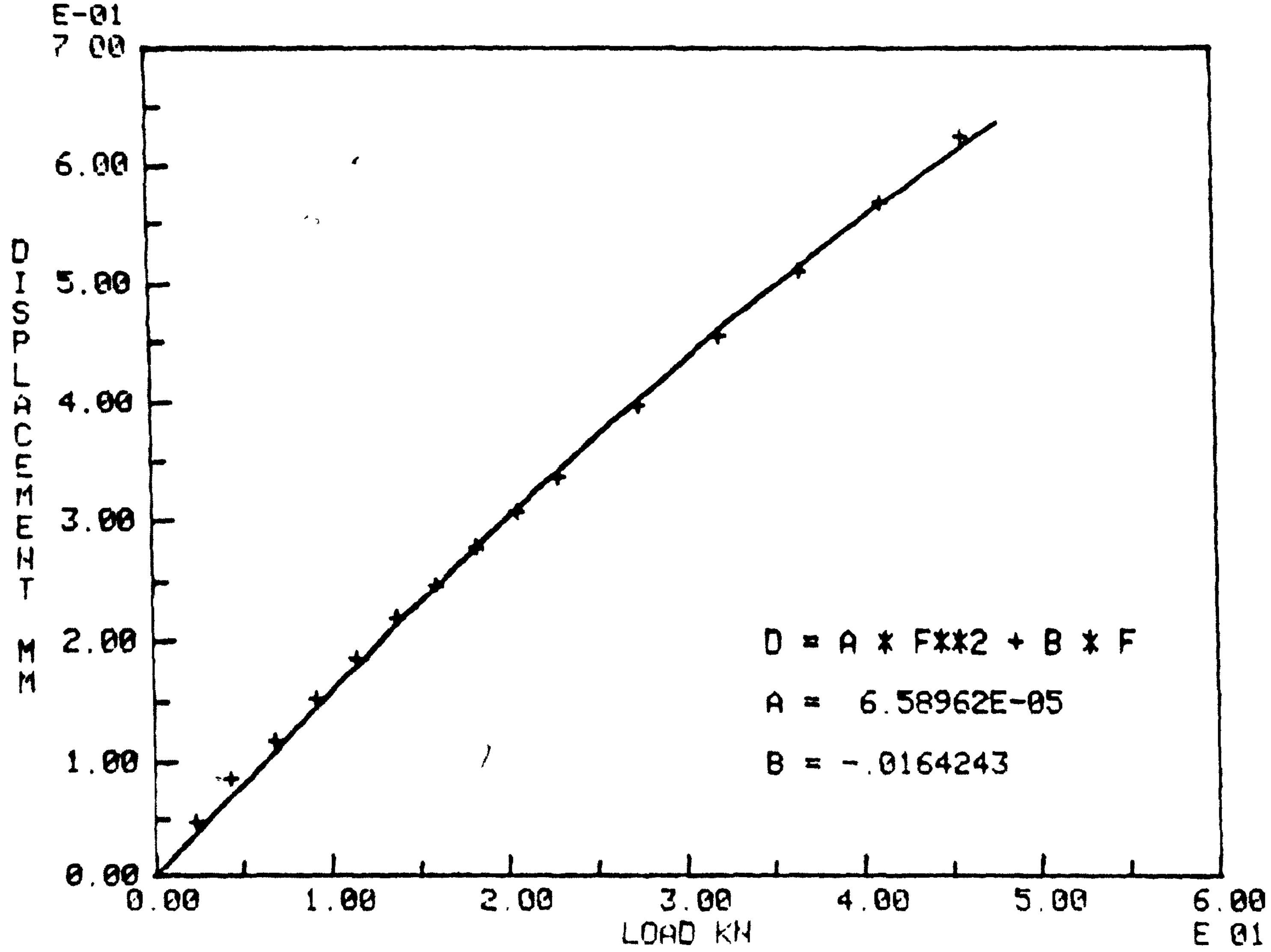

Figure A-3. Elastic compliance of the testing system.